# Breakup of a surface-mounted droplet by an impinging jet flow

by

Kenechukwu Okoye

A thesis
presented to the University of Waterloo
in fulfillment of the
thesis requirement for the degree of
Master of Applied Science
in
Mechanical and Mechatronics Engineering

Waterloo, Ontario, Canada, 2023

## Author's Declaration

I hereby declare that I am the sole author of this thesis. This is a true copy of the thesis, including any required final revisions, as accepted by my examiners.

I understand that this document may be made electronically available to the public.

# Abstract

Droplet removal under wind-forcing arises in many engineering applications, such as surface cleaning. In these applications, the efficiency of the system can be affected by droplet breakup, since smaller droplets are harder to remove. This thesis focused primarily on the breakup process of isolated surface-mounted droplets exposed to an accelerating impinging jet flow. The investigation focused on: (i) the critical flow velocities in the breakup process, and (ii) characterizing the geometry of both the originating droplet prior to breakup and the resulting child droplet.

Impinging jet flows were generated using a custom jet facility in the Fluid Mechanics Research Laboratory at the University of Waterloo. The jet centerline velocity was programmed to ramp up to a target velocity, $U_j = 20$ m/s at four flow accelerations, $\frac{dU_j}{dt} = 1.2$, 2.2, 3.2, and 4.4 m/s$^2$. Hot-wire anemometry was used to characterize the background flow field at the jet exit, and various wall-normal distances at the initial stream-wise location of the droplets.

Distilled water droplets of 50, 100, 200, 300, 400, 500, and 600 µl were tested on an anodized aluminium substrate in the impinging jet facility at the aforementioned flow conditions. Droplets were characterized based on side-view and top-view images which were captured simultaneously during the impinging jet ramp-up. The breakup process of surface mounted droplets in an accelerating impinging jet flow comprises three distinctive consecutive stages: depinning, necking, and breakup. The critical Weber number ($\overline{\mathrm{We}}_{h,\mathrm{crit}}$), based on droplet height at depinning, at which droplets in the considered volume range depin is within the range of $3 \lesssim \overline{\mathrm{We}}_{h,\mathrm{crit}} \lesssim 4$ when exposed to impinging jet flow. Shortly after depinning, necking begins as a precursor to the droplet breakup. The Weber number for the onset of necking ($\overline{\mathrm{We}}_{h,\mathrm{neck}}$) is within the range $4 \lesssim \overline{\mathrm{We}}_{h,\mathrm{neck}} \lesssim 6$. Finally, the necking process culminates in the droplet breaking up into two, or more, smaller child droplets. The Weber number at which breakup occurs ($\mathrm{We}_{h,\mathrm{br}}$) follows a power-law relationship with the Ohnesorge number (Oh). For the Ohnesorge range ($8.8 \times 10^{-4} \leq \mathrm{Oh} \leq 1.4 \times 10^{-3}$) investigated in the present study, $\mathrm{We}_{h,\mathrm{br}}$ fell in the range $6 \lesssim \mathrm{We}_{h,\mathrm{br}} \lesssim 7.5$ and showed little variation with the tested parameters.

The volume of the largest child droplet resulting from breakup was estimated using a 3D reconstruction of the droplet. Larger originating droplets shed larger percentages of their volumes during the breakup process. This is also the case for droplets exposed to higher flow accelerations. A linear correlation was also found between the lengths of the child droplet and that of the original droplet immediately prior to breakup. Based on this correlation, it was concluded that smaller sessile droplets and droplets exposed to lower flow accelerations likely break up into smaller volume fractions due to the lower elongation they experience. The results of this thesis provide useful guidelines for the optimization of impinging jet configurations in non-touch drying systems.

## Dedication

I would like to dedicate this thesis to Pratistha Gupta. Your encouragement and support throughout my masters studies means a lot to me.

# Contents

# List of Figures

# List of Tables

# List of Abbreviations

$A$ frontal area

$F_D$ drag force

$F_{\mathbf{adh}}$ adhesion force

$F_\mu$ viscous force

$U_{\mathbf{br}}$ flow velocity at which breakup occurs

$U_{\mathbf{crit}}$ critical depinning velocity

$U_{\mathbf{neck}}$ flow velocity at the onset of necking

$U_{h,\mathbf{crit}}$ critical depinning velocity measured at the droplet's height

$U_{j,\mathbf{crit}}$ critical depinning velocity measured at the jet exit

$U_\infty$ freestream velocity

$V$ droplet volume

$C_D$ drag coefficient

$\rho_\infty$ density of driving fluid

$\theta_d$ downstream contact angle

$\theta_j$ impinging angle

$\theta_s$ sessile contact angle

$\theta_u$ upstream contact angle

$\theta_{\mathbf{max}}$ maximum upstream contact angle

$\theta_{\mathbf{min}}$ minimum downstream contact angle

$h$ droplet height

$l$ droplet length

$l_0$ sessile length

$w$ droplet width

$w_{\min}$ minimum width

**CAH** contact angle hysteresis

**Oh** Ohnesoge number

**Re** Reynolds number

**We** Weber number

$\mathbf{We}_{h,\mathbf{crit}}$ critical depinning Weber number based on droplet height

$\mathbf{We}_{h,\mathbf{neck}}$ Weber number for the onset of necking

# Chapter 1

# Introduction

*This thesis considers the breakup of a single liquid droplet resting on a solid surface by an impinging jet flow. The following sections in this chapter provide a technical overview of the problem under investigation. Section 1.1 introduces the conceptual background of the problem and its relevance to engineering applications. Section 1.2 highlights the gaps in existing literature. Section 1.3 outlines the objectives of this study. Section 1.4 details the outline of the remaining chapters in this thesis.*

## 1.1    Conceptual and engineering background

Many practical applications, such as aircraft deicing [17], proton exchange membrane (PEM) fuel cell water management [14], and surface cleaning [70], encounter interactions of surface-mounted liquid droplets with shear flows. Surface-mounted liquid droplets exposed to shear flow experience an aerodynamic drag force directed downstream, which is counteracted by adhesion forces prior to droplet depinning. As the flow speed increases, the droplet deviates from its initial symmetrical sessile shape and ultimately sheds along the surface at higher flow speeds. Larger droplets generally depin at lower flow speeds [35].

For example, aircraft icing is a problem in aeronautics [8] that results from the freezing of super-cooled droplets on the aircraft's surface. This negatively affects the aerodynamics, and consequently the safety of aircraft. Ice accretion can cause increased drag, decreased lift, and a greater risk of stall [9]. An induced rolling moment may also result from asymmetric icing of an aircraft. This could cause rolling and overturn. Consequently, much effort has been put into understanding and addressing this issue. A common approach is the use of ice-phobic coatings which have a lower ice adhesion and consequently reduce the aerodynamic forces required to remove the super-cooled droplets from the structure [2].

As another example, PEM fuel cells generate electrical energy from electrochemical reactions that take place within the fuel cell membrane. At the cathode, hydrogen ions react with oxygen by catalytic reaction and form water and heat as byproducts. Excessive water accumulation degrades the fuel cell performance [61]. This is because the cathode's performance depends on the rate of oxygen transport to active sites. The presence of liquid droplets reduces the surface area for oxygen transport to active sites. As such, the management and detachment of water droplets from the cathode is a vital consideration for the performance of PEM cells. This is typically accomplished using water-exhaust systems that generate air flows over the membrane.

Surface cleaning of liquid droplets, such as oil and water, using air jets is a common practice in many industrial settings. Specifically, it is commonly employed when mechanical cleaning methods are not suitable because of constraints such as avoiding the risk of contamination or damage to the surface [30]. As such, studying optimal jet parameters for removal of liquid droplets is essential to optimizing the removal process.

In these applications, the flow speed required to remove the droplets might cause them to break up into multiple smaller droplets [4], which require even higher flow speeds to depin. Consequently, droplet breakup is a potentially undesired outcome since it leads to a cascade of smaller, harder to remove, droplets.

## 1.2    Research gaps

The droplet breakup process involves the splitting of a single droplet into multiple smaller child droplets [1] by a driving force, such as aerodynamic drag. This occurs when the drag force overcomes the restorative force due to the droplet's surface tension [46]. Most prior studies have focused on the breakup of free-falling droplets [46][29][67][24][23]. This scenario is widely encountered in atomization processes, such as gas combustion chambers, cosmetic sprays, and the chemical and drying industries [59][25][51].

The breakup process of free-falling droplets has been studied both numerically [58][47] and experimentally [32] [57]. Prior studies also considered exposing a free-falling liquid droplet to shear flows [46][64]. In this configuration, droplets have been seen to breakup in five different modes, depending on the droplet's Weber numbers, which characterizes a ratio of aerodynamic drag and cohesive force due to surface tension [64]. In comparison, the breakup of surface-mounted droplets has received significantly less attention in research literature. While freely falling droplet breakup dynamics is governed by a balance of drag force and resisting surface tension and viscous forces, surface-mounted droplets are also subjected to an adhesion force, which is expected to influence the dynamics.

Several studies have been conducted on single [52][70][35][63][4] and multiple [48][49][26][39] surface-mounted liquid droplets exposed to shear flow. However, most of these studies have focused on the flow velocity required to dislodge, or depin, the droplet for the first time. This flow velocity is referred to as the critical depinning velocity, and has been shown to be affected by various parameters, such as the initial droplet volume and the hydrophobicity of the substrate [35]. The critical depinning velocity is an important design consideration

in droplet removal applications but ultimately does not guarantee that the droplet will be removed from the surface when dislodged. For instance, the droplet might be re-adhered or breakup into smaller droplets which require a higher flow velocity to be removed [35]. This is especially a possibility for larger droplet volumes in which the role of surface tension is less significant [49]. Droplet depinning has also been seen to occur at relatively low Weber numbers. However, most papers studying the breakup process of free-falling have not considered such low Weber numbers [46].

Furthermore, droplet removal by impinging jet flows has not received much attention despite its relevance in drying and cleaning applications. Most studies have focused on the removal of surface-mounted droplets in a flat plate boundary layer. To the author's knowledge, only two studies reported jet exit velocity required for surface droplet removal [70][31]. Zhang [70] provided a comprehensive study on the optimal jet configurations for the depinning of an isolated surface-mounted droplet by an impinging jet flow. However, this study did not consider droplet breakup in the removal process.

## 1.3   Research objectives

Considering the state of the current knowledge, this thesis studies the post-depinning dynamics of surface-mounted droplets, focusing primarily on the breakup of these droplets. The specific research goals of this study are as follows.

1. Characterize the breakup of a single surface-mounted droplet exposed to impinging jet flow and quantify the underlying incoming flow conditions and droplet dynamics.

2. Characterize the geometry of the child droplet resulting from the breakup of the original surface-mounted droplet.

## 1.4   Thesis outline

The remaining chapters of this thesis are organized as follows. Chapter 2 presents a review of literature relevant to the current study. It begins by summarizing literature pertaining to impinging jet flows, which is the flow to which surface-mounted droplets are exposed to in this study. Afterwards, the aerodynamics of three-dimensional surface-mounted hemispheres are discussed in order to provide insight into the interactions of the wall-bounded background flow fields and objects of similar geometry to a droplet. Then, the interfacial phenomena pertaining to a sessile droplet, as well as the factors affecting its geometry, are discussed. Afterwards, the state-of-the art of fluid dynamics on the depinning of isolated droplets, as well as droplet arrays, is discussed. Finally, literature pertaining to the breakup of free-falling droplets, and surface-mounted droplets, in shear flow is briefly summarised.

Chapter 3 details the experiment methods used to fulfill the research objectives outlined in Section 1.3. It provides information on the impinging jet facility used to generate the

background flow. It also outlines the employed test matrix and setup used in acquiring droplet images for observing both the depinning and post-depinning behaviour of the droplets. Finally, it explains the post-processing methods used in extracting information from the acquired droplet images.

Chapter 4 presents the results. It focuses on both the depinning and subsequent breakup of droplets exposed to an accelerating impinging jet flow. First, the critical depinning velocity of the droplets being considered is evaluated. Then, the breakup process of these droplets is explored under various accelerations. Finally, the geometry of the child droplets resulting from breakup is characterized.

Chapter 5 summarises the findings of the thesis and presents conclusions pertaining to the breakup of surface-mounted droplets exposed to impinging jet flow. It also provides suggestions on potential directions for future studies on the topic.

# Chapter 2

# Research Background

*This chapter reviews the literature relevant to the present study. Section 2.1 discusses the fluid dynamics of an impinging jet flow. Section 2.2 discusses the flow development over three-dimensional hemispheres. Finally, Section 2.3 expands on the interfacial physics of a sessile droplet resting on a substrate (Section 2.3.1), then reviews the studies on depinning of an isolated droplet (Section 2.3.2) and depinning of droplet arrays (Section 2.3.3). Finally, Section 2.3.4 reviews the studies on droplet breakup.*

## 2.1  Impinging jets

An impinging jet flow is created when expelled fluid from a nozzle is directed onto a surface as seen in Figure 2.1. As the jet flow approaches the surface, there is a decrease in flow velocity accompanied by an increase in static pressure, which forms a stagnation zone. The flow then reorients to become aligned with the surface, after which a wall jet develops. Static pressure decreases along the surface and the favorable pressure gradient accelerates the reoriented flow. There are three characteristic regions that are commonly observed in impinging jet flows: a free jet region, impingement region, and a wall jet region [44].

The free jet region begins at the nozzle exit and is composed of two characteristic regions: a shrinking potential core and a widening mixing layer. Conventionally, for impinging jets, the potential core length is defined as the distance from the jet exit to the location where dynamic pressure is 95% of the initial average dynamic pressure [44]. When the nozzle-to-plate spacing is too small, the free jet region might not be present [56].

The impingement region is a region of fluid near the surface with near zero velocity magnitude and fluctuations. It contains the stagnation point located near the intersection between the jet centreline and the impingement surface. The wall jet region forms once the
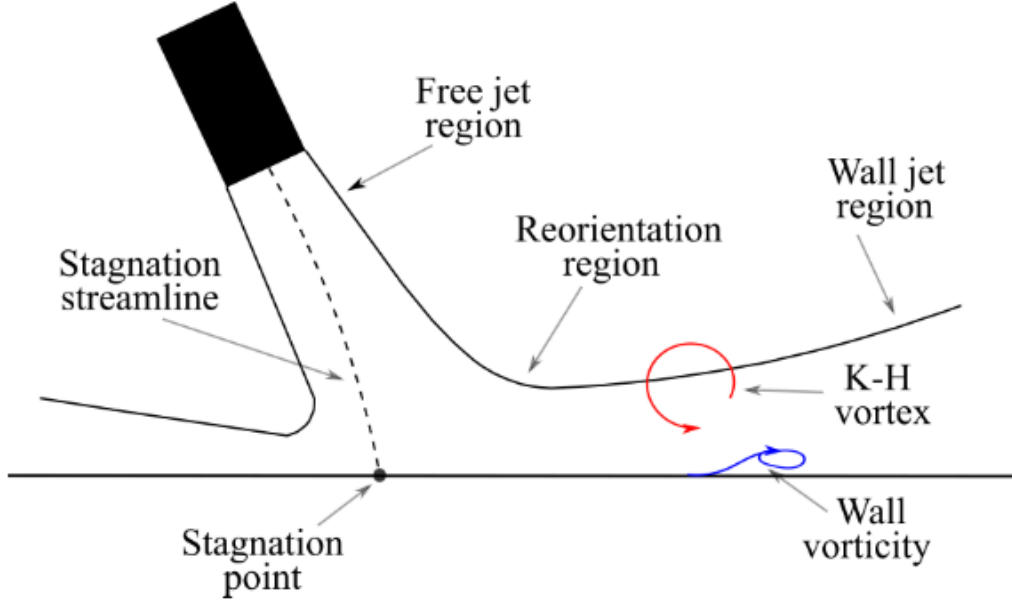
**Figure 2.1:** Characteristic regions of an impinging jet. Figure adapted from Zhang [70].

flow reorients along the impingement surface. It is typically characterized by two lengths (see Figure 2.2): $y_m$, the local wall normal distance to the maximum average stream-wise velocity, $U_m$, and the wall-jet half-width, $y_{\frac{1}{2}}$, which is the wall normal distance where the local average stream-wise velocity is $0.5U_m$ [44]. The wall jet is often subdivided into inner and outer layers, separated by $y_m$, where the flow development is similar to boundary layer flows and free shear layers, respectively [45].

There are many factors that affect the flow development of an impinging jet flow, such as jet Reynolds number, nozzle geometry, and nozzle-to-plate spacing [20]. The nozzle-to-plate spacing determines the type of impingement. Placing the surface beyond the potential core length creates transitional impingement, where an additional region of velocity decay is observed beyond the potential core length. Alternatively, placing the surface within the potential core length creates potential core impingement in which the decay region is suppressed. Impinging jet flow can also be categorized into different types based on the angle of the jet flow relative to the surface. A normal impinging jet is created if the surface is perpendicular to the jet flow. A jet oriented parallel and sufficiently close to the surface will create wall jet flow [44]. Orienting the surface at any other angle will result in an oblique impinging jet [44].

6
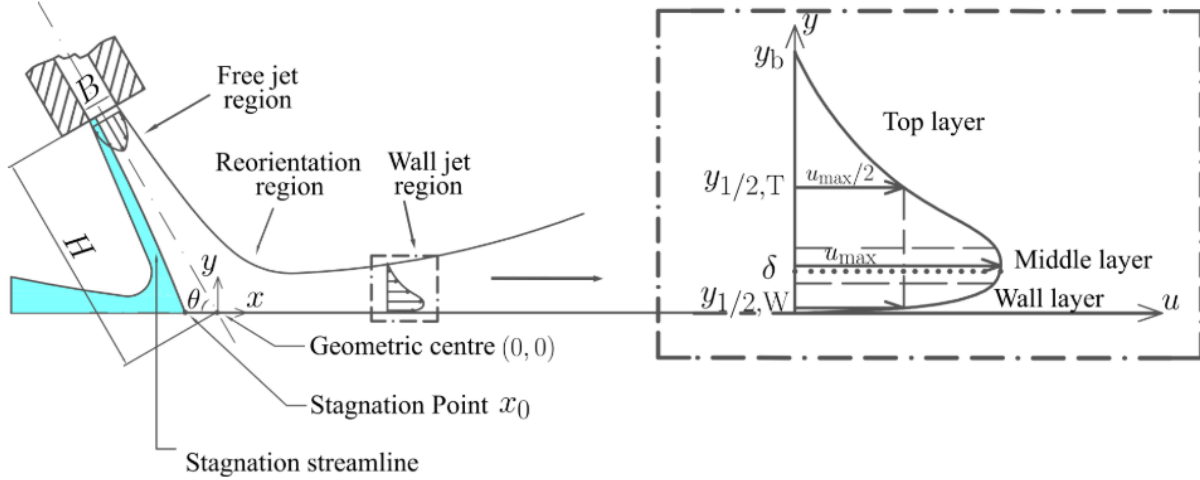
**Figure 2.2:** Schematic of an oblique impinging jet flow. The green-shaded region masks the region that is not of interest. Figure adapted from Zhang [70].

## 2.2 Flow over a three-dimensional hemisphere

Studies have shown that the flow development over a surface-mounted hemisphere is a reasonable approximation for the flow over a surface-mounted droplet [71]. Due to boundary layer growth along the wall and the lack of up-down symmetry, the flow around a surface-mounted sphere is more complex that around a freely floating sphere [10]. Figure 2.3 illustrates the flow development around a surface-mounted hemisphere. The flow forms a stagnation region on the upstream surface as it approaches the body [53]. Upstream of the body, the boundary layer will also separate due to the adverse pressure gradient induced by the body. The separated flow rolls up downstream and surrounds the bluff body, to form a system of horse-shoe vortices [66]. The horseshoe vortex system wraps around the hemisphere and orients predominantly downstream. These vortex lines curve in towards the centreline as the separated flow reattaches to the substrate, resulting in the characteristic 'necklacing' vortex topology in the wake [53]. The formation and necklacing of the horseshoe vortex system has been observed for both laminar and turbulent incoming boundary layers, and for different smooth obstacle geometries [70] [66].

There are three Reynolds number ($Re_h$) regimes associated with characteristic trends observed in the drag coefficient ($C_D$) of a surface-mounted hemisphere [10]. Initially, the drag coefficient decreases with increasing Reynolds number [10]. At a higher Reynolds number ($Re_{h,\text{crit}}$), the hemispheres experience a phenomenon known as a drag crisis. The drag crisis is characterized by a rapid drop in the drag coefficient of the body. This $Re_{h,\text{crit}}$ has been shown to correlate with the aspect ratio of the obstacle, with $Re_h \propto (\frac{h}{c})^{\frac{2}{5}}$. For an obstacle with $\frac{h}{c} \approx 1$, this critical value lies between $600 < Re_h < 900$ [70]. Cao et al. [10]
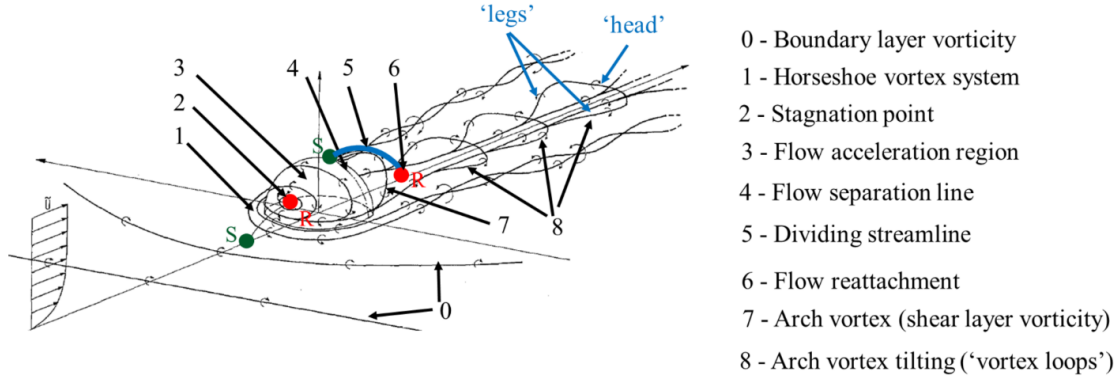
**Figure 2.3:** Flow development over a surface-mounted hemisphere. Figure adapted from Savory and Toy [53].

reported a lift crisis that occurred in the same regime as the drag crisis. At the critical Reynolds number, the lift force of the hemisphere doubled due to the lift crisis, while the drag force halved due to the drag crisis. Finally, for $Re_h > Re_{h,\text{crit}}$, $C_D$ increases initially with increasing Reynolds number but ultimately becomes Reynolds number independent [10][60][33]. In order of increasing $Re_h$, these regimes are referred to as subcritical, critical, and supercritical [10].

## 2.3 Droplet research

### 2.3.1 Droplet physics at sessile state

The surface energy/tension ($\gamma_A$) associated with a specific homogeneous phase (A) can be described as the change in free energy when the surface area is increased by a unit area [11]. By extension, when an interface is formed between two phases A and B, there also exists an interfacial energy/tension ($\gamma_{AB}$). This interfacial tension is the change in free energy when the interfacial area is changed by a unit area [28].

When a liquid droplet (L) is placed on a solid surface (S), three interfaces exist, as seen in Figure 2.4. These are the solid-gas, solid-liquid, and liquid-gas interfaces. Each of these interfaces have an interfacial tension associated with them: $\gamma_{SG}$, $\gamma_{SL}$, and $\gamma_{LG}$, respectively. The point where all three phases intersect forms the contact line. The angle between the solid surface and the tangent of the liquid-gas interface at the contact line is the sessile contact angle ($\theta_s$) [70]. The sessile contact angle can be estimated for an ideal smooth surface using Young's Equation (Equation 2.1) [28] where $\gamma$ is the interfacial tension between the liquid and gas phases referred to as the surface tension of the liquid.

$$\gamma \cos\theta_s = \gamma_{SG} - \gamma_{SL} \qquad (2.1)$$

8
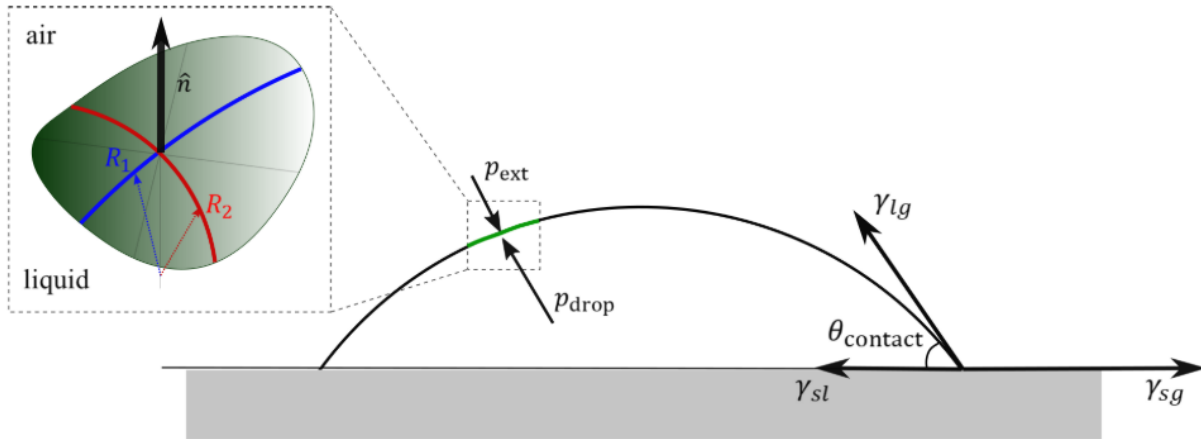
**Figure 2.4:** Interfacial tensions of a sessile droplet. Figure adapted from Zhang [70].

However, there are limitations to Young's equation. For example, it assumes that the solid surface is perfectly smooth, but this is unlikely in reality. The roughness of the solid surface increases the effective interfacial area and affects $\theta_s$. The Wenzel model (Equation 2.2) attempts to account for this by using a scaling factor ($r$) to account for the actual wetting relative to the apparent wetting of the solid surface[28].

$$\gamma \cos\theta_s = r(\gamma_{SG} - \gamma_{SL}) \tag{2.2}$$

Another limitation of Young's equation is that, in reality, most solid surfaces are chemically heterogeneous, contrary to the surface homogeneity assumed in Young's equation. The Cassie-Baxter model (Equation 2.3) attempts to account for this by dividing the solid surface into chemically homogeneous fractions (e.g. $f_1$ and $f_2$) where $f_1 + f_2 = 1$ [28]. However, this model only holds for a smooth surface.

$$\gamma \cos\theta_s = f_1(\gamma_{SG1} - \gamma_{SL1}) + f_2(\gamma_{SG2} - \gamma_{SL2}) \tag{2.3}$$

Another useful parameter in droplet-solid interactions is the spreading coefficient ($S$) (Equation 2.4) [43]. Spreading occurs when $S > 0$ and the larger the value of the spreading coefficient, the more rapidly the wetting occurs. Equation 2.4 also shows that, for good wetting, the surface tension of the solid must be greater than the surface tension of the liquid. In other words, greater wetting occurs for solids with high surface energy and/or liquids with low surface tension.

$$S = \gamma_{SG} - (\gamma_{LG} + \gamma_{SL}) \tag{2.4}$$

The contact angle a liquid droplet makes on a solid surface can characterize the wettability and surface energy of the solid surface since lower contact angles result from

higher wettability of the solid [43]. A hydrophobic surface tends to not be wetted by water, whereas a hydrophilic surface is wetted by water. Practically, hydrophobicity and hydrophilicity are relative terms commonly characterized by the contact angle of water droplets when placed on the solid. For contact angles of water less than 90°, the surface is designated as hydrophilic. If water spreads over the surface, and the contact angle at the spreading front edge is less than 10°, the surface is often designated as super-hydrophilic provided that the surface is not absorbing the water, dissolving in the water, or reacting with the water. Alternatively, more hydrophobic solid surfaces result in droplets with higher contact angles. Surfaces with contact angles greater than 90° are designated as hydrophobic. Theoretically, the maximum contact angle for water on a smooth surface is 120°. However, micro-textured or micro-patterned surfaces with hydrophobic asperities can exhibit apparent contact angles exceeding 150° and are designated as super-hydrophobic [3].

Another important factor to consider in liquid droplets is their volume; the shape of a droplet has been shown to be affected by the size of the droplet [15][6]. For a sufficiently small droplet, its shape is governed by capillary forces which dominate gravity and the droplet retains a nearly spherical shape. For sessile volumes larger than a certain threshold, gravitational effects become more significant and distort the droplet shape. In this case, the droplet shape becomes similar to a spherical cap. For even larger volumes, gravity dominates and the droplet is flattened by gravity. The threshold volumes for the three aforementioned regimes vary for different liquids but have been shown to be related to the capillary length. For most liquid droplets on a substrate, the droplet baseline length and height increase along with the volume until the gravity flattened regime where the droplet height plateaus to a constant value and the droplet length increases less gradually [15][6][63]. The sessile contact angle of the droplet, however, has been shown to be independent of the droplet volume in all three regimes for a variety of droplet-substrate configurations [6].

### 2.3.2 Depinning of an isolated droplet

When a sessile droplet is exposed to incoming flow, there are three forces experienced by the droplet: the driving force of aerodynamic drag and two resisting forces (adhesion force ($F_{\text{adh}}$) and viscous force ($F_\mu$)). This force balance is illustrated in Figure 2.5.

When exposed to shear flow, the flow around a droplet behaves similarly to the flow around a hemisphere [71]. Specifically, a low pressure region forms behind the droplet, resulting in a downstream drag force ($F_D$). As the freestream velocity ($U_\infty$) increases, the drag force ($F_D$) increases. The drag force can be estimated from Equation 2.5 [62][34], where $A$ is the frontal area, $\rho_\infty$ is the density of driving fluid, and $C_D$ is the drag coefficient dependent on the droplet shape. As the drag force is applied to the droplet, it causes a change in the droplet geometry, whereby, the upstream contact angle ($\theta_u$) decreases while the downstream contact angle ($\theta_d$) increases. Ultimately, as the flow velocity is increased, $\theta_u$ and $\theta_d$ will exceed their limits ($\theta_{\min}$ and $\theta_{\max}$ respectively), and the droplet will "depin" from the substrate in the downstream direction.
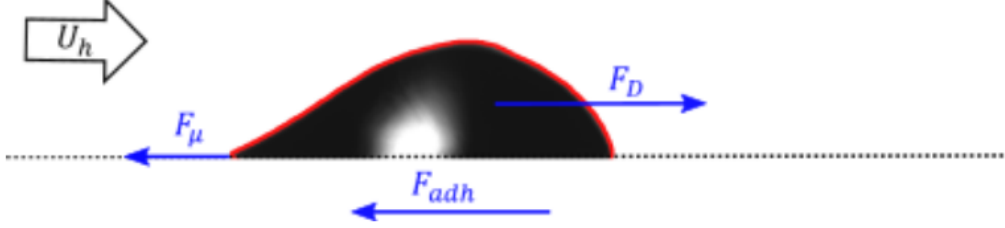
**Figure 2.5:** Force diagram of a droplet prior to depinning. Figure adopted from Zhang [70].

$$F_D = \frac{\rho_\infty U_\infty^2 A C_D}{2} \tag{2.5}$$

The adhesion force of the droplet is a function of the geometry and surface tension of the droplet (Equation 2.7). It can be calculated based on the contact angle distribution $(\theta(l_{\mathrm{cl}}))$ along the contact line $(l_{\mathrm{cl}})$ and the contact line shape $(\psi(l_{\mathrm{cl}}))$. The contact line shape is the angle between the wall-normal vector of the local contact line and the applied force. However, $\psi(l_{\mathrm{cl}})$ and $\theta(l_{\mathrm{cl}})$ are difficult to estimate. Therefore, a simplified expression (Equation 2.7) for adhesive force is commonly used [62][34][70]. The lateral adhesion is expressed as a function of the contact angle hysteresis (CAH = $\cos(\theta_u)$ - $\cos(\theta_d)$) [70], and droplet length $(l)$, while $k$ is a factor that accounts for $\psi(l_{\mathrm{cl}})$ and $\theta(l_{\mathrm{cl}})$. The contact angle hysteresis reflects the energy required to change the droplet from one metastable state to another. There is a consensus that the adhesion force is proportional to CAH, with some discrepancies in the reported values of $k$ [18].

$$F_{adh} = -\gamma \int_0^l \cos(\theta(l_{\mathrm{cl}}))\cos(\psi(l_{\mathrm{cl}}))dl \tag{2.6}$$

$$F_{adh} = k\gamma l(\cos(\theta_u) - \cos(\theta_d)) \tag{2.7}$$

Finally, the viscous force is the force that results from the fluid resistance to shear stress. When a droplet is exposed to incoming flow, the resulting shear stress causes the droplet to exert a viscous force on the driving fluid to resist deformation. However, the viscous force has been shown to be significantly smaller in magnitude compared to the drag force and adhesion force, so it can be neglected when studying droplet depinning [70][62]. This is especially true when the droplet has not started moving because the effect of droplet viscosity will be limited to controlling the rate of deformation of the droplet surface in response to the shear flow [16].

In summary, the depinning dynamics of a surface-mounted droplet exposed to shear flow is primarily determined by the downstream directed drag force and the upstream directed adhesion of the droplet. As the freestream velocity increases, the drag force increases. The lateral adhesion increases in response to the drag force in order to resist motion, which causes the droplet to deform [4]. Eventually, the drag force exceeds the adhesion

force and the droplet "depins". Berejnov and Thorne [5] found that both contact points do not depin simultaneously. The upstream contact point remains stationary while the downstream contact point moves downstream, causing the droplet to elongate. At higher flow velocities, the upstream contact point also depins, and both contact points continue to move downstream. The flow velocity at the moment when the upstream contact point depins is referred to as the critical depinning velocity ($U_{\text{crit}}$) [70]. This has been a subject of interest in many studies because of its relevance in some engineering applications [35][4][52].

The critical depinning velocity of a droplet is influenced by changes in one or more of the forces in Figure 2.5. For example, larger droplets have larger frontal areas, as a result, they experience a higher drag force than smaller droplets at the same freestream velocity. On the other hand, a larger volume droplet also experiences a higher lateral adhesion. Several studies have shown that the increase in drag is greater than the increased adhesion, and consequently larger droplets have lower critical depinning velocity [62][70][16][4]. This trend is more noticeable in smaller droplet volumes, but plateaus as the droplet volume increases to the gravity flattened regime [54][35].

For more hydrophobic substrates, the sessile contact angle of the droplet is higher, and the droplet takes a more rounded shape. This translates into a larger frontal area and $C_D$ resulting in a higher experienced drag for the same freestream velocity. Higher hydrophobicity is also accompanied by a decrease in lateral adhesion. Milne et al. [35] studied water droplets on PMMA, Teflon, and SHS, and hexadecane droplets on Teflon. They tested a wide range of droplet volumes and found that the maximum adhesion force consistently decreased with increasing hydrophobicity for all volumes tested. As a result, the critical depinning velocity decreases as the hydrophobicity of the substrate increases. These findings agree with Baware et al. [4] who found that $U_{\text{crit}}$ strongly depends on CAH.

Fan et al. [16] tested water-glycerine mixtures with glycerine concentrations of 0, 50, and 100% on three surfaces. They found that the droplet-surface combinations with higher contact angles had lower critical depinning velocity. They also investigated Newtonian oils of viscosity 5, 10, and 20 mPa on a controlled Certonal FC732 surface. They found that droplets with higher viscosity had a higher critical depinning velocity. However, the effect was minor compared to other factors like size and shape, consistent with [70][4].

Fu et al. [18] tested a glycerol droplet on PMMA, glass, and polished stainless steel. They found that there is a critical friction velocity ($u_f$) (Equation 2.8) at which the droplet depins. Their results show a linear relationship between the initial droplet diameter and the critical length of the droplet. Also, the critical friction velocity has an exponential relationship ($u_{f,\text{crit}} \approx C_0 d_{\text{drop}}^{-k_0}$) with the diameter of the droplet ($d_{\text{drop}}$) where $k_0$ was close to 0.5 in all cases. This is consistent with findings by Wang et al. [62] showed that $U_{\text{crit}} \propto \sqrt{\frac{1}{R}}$, where $R$ is the radius of the wetted area of the droplet.

$$u_f = \sqrt{-\frac{h}{2\rho}\frac{dp}{dx}} \tag{2.8}$$

Mandal et al. [34] investigated droplet depinning on PMMA, Teflon, and SHS at temperatures ranging from subfreezing to room temperature and for different droplet

volumes. In their results, the critical depinning velocity did not change appreciably on Teflon. However, in all other cases, the critical depinning velocity increases under icing conditions. They concluded droplets may flatten at subfreezing temperatures, particularly larger droplets. However, droplets on Teflon did not flatten significantly. This flattening, as well as an increased CAH, translate to an increase in adhesion at subfreezing temperatures. Combined with a decreasing drag coefficient, this brings about an increase in critical depinning velocity. These findings agree with those from a similar study by Roisman et al. [52].

Zhang [70] conducted an impinging jet study with individual water droplets on an anodized aluminium substrate. The results show that as the impinging angle ($\theta_j$) increases, the elongation and CAH of the droplet decrease at depinning. These effects translate to a decrease in adhesion force causing the critical depinning velocity to decrease as $\theta_j$ is increased. It is also reported that, as the turbulence intensity of the free-stream flow increase, the critical depinning velocity decreases. In addition, the results show that the critical depinning velocity decreases slightly with increasing initial free-stream acceleration. Droplets in a flat plate boundary layer have been found to have a constant depinning threshold of $\mathrm{We}_{h,\mathrm{crit}} = 7.5 \pm 0.5$. Droplets in impinging jets have lower thresholds within the range of $2 \leq \mathrm{We}_{h,\mathrm{crit}} \leq 4$.

### 2.3.3 Droplet arrays under wind forcing

As discussed in Section 2.3.2, a number of studies considered depinning of a single isolated droplet. However, in many practical scenarios, multiple droplets are exposed to shear flow. In such cases, the drag force experienced by each droplet is affected by wake interactions, consequently affecting their critical depinning velocity [49].

Razzaghi et al.[48] studied a pair of equally sized droplets in a wind tunnel. For several droplet spacings, they studied the droplets in both a tandem and side-by-side configuration on two different substrates (PMMA and Teflon coated aluminium). When the droplets were placed in tandem, the downstream droplet was shielded from the flow by the upstream droplet, whilst the upstream droplet's wake was being stabilized by the downstream droplet. These effects caused both droplets to experience a lower drag force compared to an isolated droplet in the same flow. It was concluded that this was primarily a result of the drag coefficient of both droplets being reduced by the presence of the other droplet. Ultimately, this translated to both droplets having a higher critical depinning velocity. In this arrangement, it was found that the upstream droplet depinned first, then collided with the downstream droplet before moving together as a larger droplet resulting from their coalescence. As the spacing between the droplets increased, the critical depinning velocity of the upstream droplet was seen to reduce until it approached the critical depinning velocity of a single isolated droplet at large spacings. At these large spacings, the droplets were also seen to depin independently. They also found that the critical depinning velocity of the upstream droplet was higher for droplets with larger volumes, especially at smaller spacings. This differs from what has been seen with single droplets [62][70][16][4]. They attributed this to the fact that larger droplets have larger $F_{\mathrm{adh}}$, as seen in the work of Milne

et al. [35]. Therefore, this coupled with the decrease in drag coefficient experienced by droplets in groups requires a larger flow velocity to generate a drag force high enough to depin the droplets.

In a side-by-side configuration, the droplets were seen to co-shed and move identically. For small spacings, the droplet were seen to have $U_{\text{crit}}$ similar to a single droplet but the critical depinning velocity increased with increasing spacing until a critical spacing where it relaxed to the critical depinning velocity of a single droplet once more upon further increase in spacing. The maximum spacing in which the downstream droplet influenced the upstream droplet was seen to reduce with increasing hydrophobicity. In another publication by the same group [49], some other configurations were also considered: triangle, reversed triangle, diamond and square configurations on the same substrates at only two spacings. It was shown that most of the previously reported trends applied to these configurations as well. The upstream droplet(s) slid first and collided with downstream droplets that were in tandem. It was also seen that most of the droplets had a critical depinning velocity that was higher than that of an isolated droplet.

### 2.3.4 Droplet breakup in shear flow

As discussed in Section 2.3.2 and Section 2.3.3, a lot of prior research has focused on droplet depinning. Although the critical depinning velocity is an important parameter, for practical applications such as drying, the post-depinning dynamics of droplets is also of interest. One such behaviour is the breakup of droplets since it can leave behind small droplets on the surface that have a relatively high critical depinning velocity.

In order to study the aerodynamic forces that result in droplet breakup, it is common to begin by analyzing the deformation and consequent breakup of a single droplet. Most experiments on the subject involve exposing a free-falling droplet to breakup inducing loading, including shock waves [40][50][22][21], and continuous air jets [64][65]. There have also been numerical studies on the breakup of droplets [59][41][47]. The first, and most popular, complete analytical model for modelling a deforming droplet undergoing breakup in a uniform air jet is called the Taylor Analogy Breakup (TAB) model. It models the droplet using a mass-spring-damper where the droplet liquid viscosity is a damping force while the restorative surface tension acts as the spring force. This model did not compare well with experimental results, but has served as a foundation for many subsequent models [69].

Many variables have been used in literature when correlating droplet breakup properties e.g. Weber number, Bond number, Reynolds number, freestream velocity[57], and Capillary number [59]. However, when studying the breakup of individual droplets in air flow, the Weber number and the Ohnesoge number (Oh) are the two most influential parameters [27]. The Weber number (We $= \frac{\rho U^2 D}{\gamma}$, where $\rho$ is the density of the driving fluid, $U$ is the flow velocity, $D$ is a characteristic length of the droplet, and $\gamma$ is the surface tension of the droplet) represents the ratio of the disrupting aerodynamic force to the restorative surface tension force [57]. The Ohnesoge number (Oh $= \frac{\mu_{drop}}{\sqrt{\rho_{drop}\gamma D}}$, where $\mu_{drop}$ is the dynamic

viscosity of the droplet, $\rho_{drop}$ is the density of the droplet) represents the relative importance of the viscous force to the inertial and surface tension forces [68].

A liquid droplet exposed to shear flow will breakup if the Weber number is higher than a critical value [29]. Experiments on the breakup of free-falling liquid droplets in a shear flow have revealed that there are different modes of breakup that may occur depending on various droplet properties and the surrounding flow characteristics (see Figure 2.6) [64]. Each breakup mode has been seen to occur within a characteristic range of Weber number. Five different modes of breakup are commonly observed. In order of increasing Weber number, they are vibrational breakup, bag breakup, multimode breakup, sheet-thinning breakup, and catastrophic breakup [69]. The transition Weber number between different modes has been shown to increase with increasing Ohnesoge number. This is because the viscous forces inside the droplet hinder its deformation [68]. The critical Weber number, which is the threshold Weber number for bag breakup, has been found to be approximately 12 for Oh < 0.1 [46].

Most studies have focused on high Weber number breakup modes and have consequently exempted the vibrational breakup. The vibrational breakup may occur when the Weber number is relatively small and oscillations develop at the natural frequency of the droplet [46]. Under certain conditions, interactions with the flow field may cause the droplet's oscillation amplitude to increase and ultimately cause the droplet to break into a few large fragments [64]. When it occurs, it only produces a few large fragments, and the overall breakup time is relatively long compared to those seen for the other regimes [46]. As a result, the vibrational breakup is not usually considered when droplet breakup is studied [46]. Although the definition of the initiation of the breakup process varies according to the breakup mechanism, the time required to initiate breakup has been seen to decrease continuously with increasing Weber number [46].

Droplet breakup has also been observed in experiments where a droplet suspended on a substrate was exposed to a shear flow. Fu et al. [18] investigated glycerol droplets on stainless steel, PMMA, and glass in a wind tunnel. They found that droplets broke up while depinning on the stainless steel substrate unlike the tests done on PMMA and glass. After depinning, the droplet continued to elongate and ultimately splits into several portions. The larger portion continued to move in the stream-wise direction while the other portion remained stationary. However, under similar conditions on an inclined plane, this breakup was not seen. Fu et al. [18] attributed the breakup to a complex instability phenomenon. A similar trend was seen in a study by Barwari et al. [4] in which droplets of various water-glycerol fractions and various water-ethanol fractions were tested in a wind tunnel on PMMA and CSW substrates. It was observed that some droplets broke up on PMMA but never on CSW. It was proposed that this might have been because CSW substrate was smoother than PMMA. It was further proposed that this phenomenon might be linked to the surface energy of the substrate, since PMMA is more hydrophilic. This breakup was seen for higher viscosity droplets which elongated to form a tail at their upstream point while in motion. This tail was seen to elongate as the droplet travelled downstream. The tail formation was also seen to be linked to the breakup of the droplet and the threshold viscosity for the onset of tail formation was seen to be lower on PMMA than CSW.
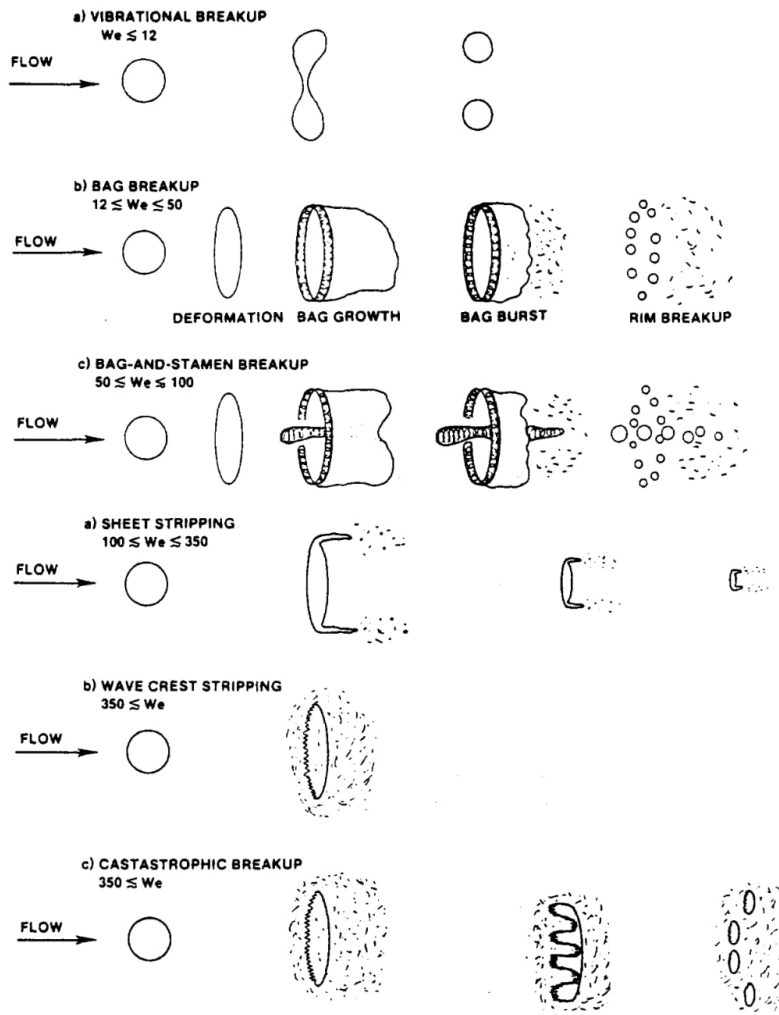
**Figure 2.6:** Breakup modes of liquid droplet in gas flow. Figure adopted from Pilch [46].

Leung et al. [31] exposed randomly distributed glycerol-water droplets on PMMA to an impinging jet flow. When exposed to the flow, the millimeter-sized droplets deformed and split into smaller droplets with diameters on the order of hundreds of micrometers. The droplets slid away from their original positions and ultimately became re-adhered at a downstream distance proportional to their size. They became re-adhered because the aerodynamic force weakened farther away from the impinging point. At the location of their re-adherence, the weakened aerodynamic force could no longer overcome the droplets' adhesion force [31].

Although the experiments focusing on free-falling droplets provide useful insights into droplet breakup, they have mostly focused on higher Weber number and leave questions unanswered about how breakup translates to a suspended droplet in which the lateral adhesion would play a significant role. The experiments on substrates have also not focused on the specific breakup dynamics and have consequently not provided in-depth insight into the breakup of surface-mounted droplets.

# Chapter 3

# Experimental Setup and Procedures

*This chapter presents the experiment methodologies employed to achieve the research objectives outlined in Section 1.3 and is divided into three sections. Section 3.1 introduces the jet facility used in the present work and expands on the method by which the flow was characterized. Section 3.2 identifies the key experimental parameters and test matrix for investigating the droplet depinning and breakup in shear flows. The experimental setup for controlling the identified parameters is also described. Finally, Section 3.3 introduces the post-processing procedures used to extract quantitative geometric properties from the acquired droplet images.*

## 3.1   Impinging jet facility

An impinging jet flow was generated using a custom jet facility in the Fluid Mechanics Research Laboratory at the University of Waterloo [70]. The experimental setup is illustrated in Figure 3.1. Airflow from a blower was first conditioned by passing it through a honeycomb structure and four mesh screens. The conditioned flow was then accelerated through a 9:1 two-dimensional contraction. The velocity profile exiting the nozzle was uniform, with a maximum deviation of less than 1% across 95% of the span. An anodized aluminium plate with dimensions $60B \times 80B$ in the streamwise ($X$) and spanwise ($Z$) directions, respectively, served as the impingement target. For all experiments conducted, the nozzle-to-plate spacing (defined as the distance from the nozzle exit to the plate along the free stream direction) and impinging angle were kept constant at $H/B = 4$ and $\theta_j = 30°$, respectively.

   In the experiments pertaining to droplet breakup (Section 3.2), the jet exit velocity was increased from 0 to 20 m/s with varying flow acceleration (1.2, 2.2, 3.2, and 4.2 m/s$^2$). The ramp-up velocity profile of the jet facility was characterized using hot-wire measurements. A
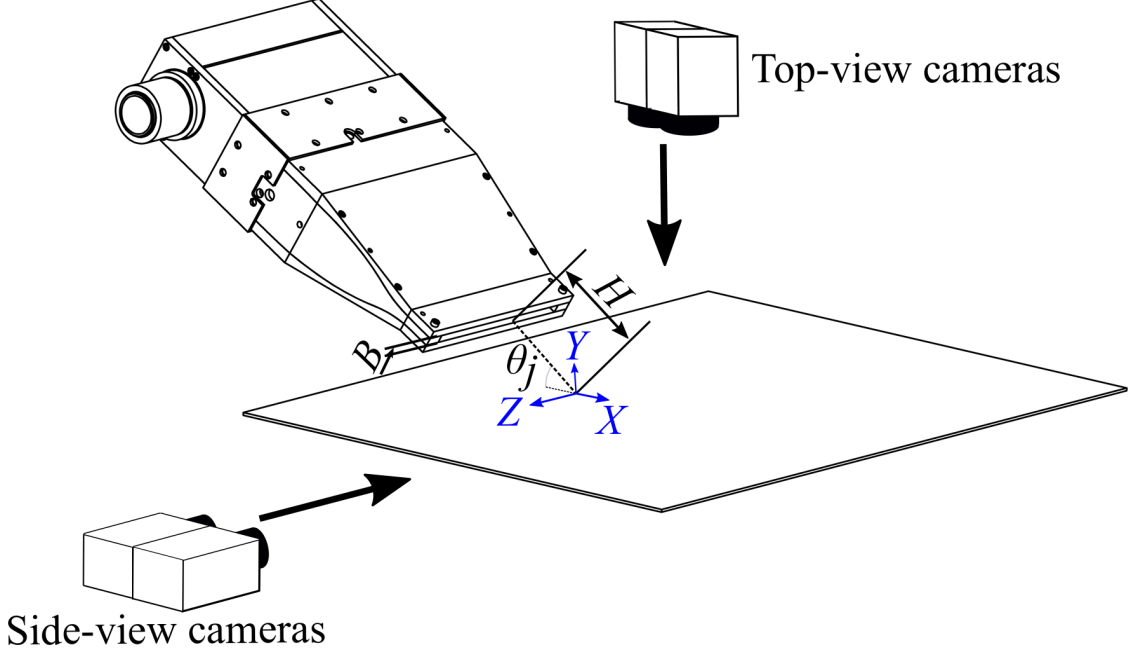
**Figure 3.1:** Schematic of the impinging facility, instrumentation, and variable definitions.

Dantec Streamline Pro constant-temperature anemometer was used to measure jet velocity, at the jet exit, with an uncertainty estimated, based on calibration and methodological variations, to be below 2.3%. The overheat ratio and acquisition rate were set to 0.5 and 10 kHz, respectively. The instantaneous velocities were measured at the jet exit, and each test was repeated five times for each acceleration investigated. A consistent velocity ramp up was produced at the jet exit slot for all runs and accelerations. A single run for each configuration is shown in Figure 3.2 as an example. The ramp-up profile is seen to be quasi-linear between $3 \lesssim U_j \lesssim 20$ m/s. As such, for each configuration, a linear fit (illustrated by the red dashed line) was applied to the ensemble of five runs. For the experiments on surface-mounted droplets, instantaneous flow velocity at the jet exit was estimated based on these fits as follows. Trigger signals for all cameras used in experiments were synchronized with the trigger signal for initiating the jet ramp up. The jet exit flow velocity corresponding to each image was estimated by applying the corresponding linear fit using the image's acquisition timestamp relative to the beginning of the jet ramp up. The uncertainty of this approach, due to probe calibration, methodological variations, and the fit error, is estimated to be less than 2.6% (see Appendix B). The primary benefit of this approach is the prevention of optical obstruction and light scattering caused by the presence of the hot-wire probe during droplet imaging.

In the present study, the initial location of the droplets in all experiments, detailed later
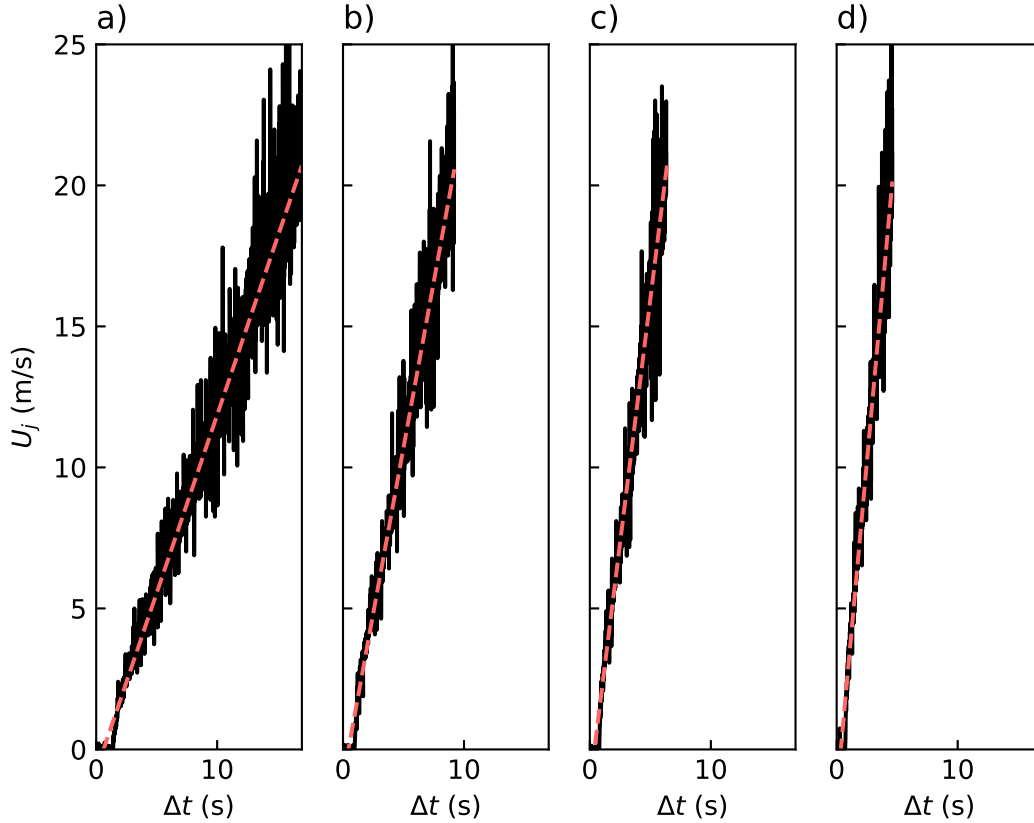
**Figure 3.2:** Flow velocity sampled at the jet exit for various flow accelerations, a) 1.2, b) 2.2, c) 3.2, and d) 4.4 m/s². The red dashed lines represent linear fits applied to the ensemble averages of the corresponding five runs.

in Section 3.2, was $X^* = 3.5B$ from the stagnation point. Using a similar approach to that used for characterising the ramp-up velocity profile at the jet exit, the ramp-up profiles at this location were also characterized. Using the same acquisition parameters and target velocity, hot-wire measurements were taken at wall-normal distances $Y = 1$ mm and 2 mm at a flow acceleration of 4.4 m/s² as well as $Y = 3$ mm at flow accelerations of 1.2, 2.2, 3.2, and 4.4 m/s². These wall normal locations correspond to the heights of the droplets that were considered. The hot-wire position was measured using calibrated side-view camera images. Velocity measurements were repeated five times for each configuration. A sample result for each configuration is shown in Figure 3.3 and the ramp-up profile is also seen to be quasi-linear between $3 \lesssim U_j \lesssim 20$ m/s. As such, the red dashed lines once again represent the linear fit applied to the ensemble of the five runs in the corresponding configuration.
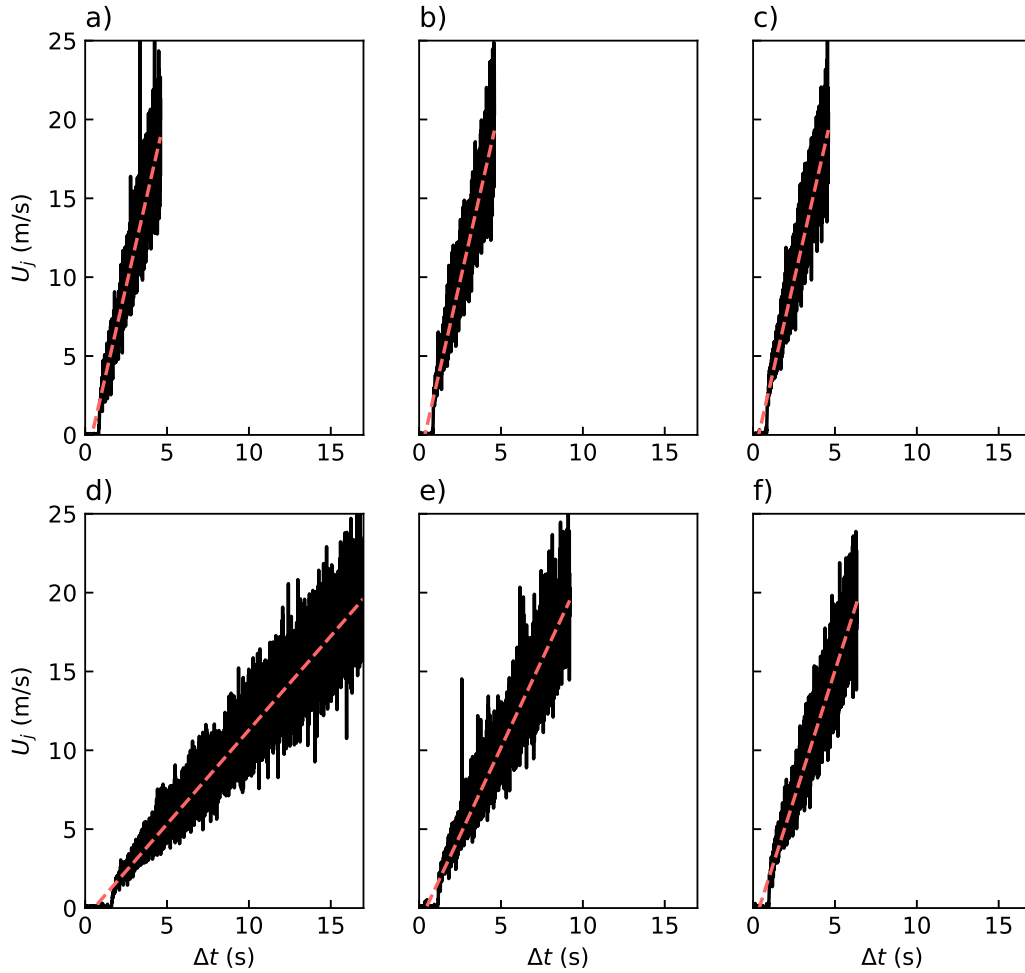
**Figure 3.3:** Flow velocity sampled at $X^* = 3.5B$ at various wall-normal ($Y$) locations and flow accelerations. $Y =$ a) 1, b) 2, and c) 3 mm with $\frac{dU_j}{dt} = 4.4$ m/s$^2$ as well as $Y = 3$ mm with $\frac{dU_j}{dt} =$ d) 1.2, e) 2.2 and f) 3.2 m/s$^2$. The red dashed lines represent linear fits applied to the ensemble averages of the corresponding five runs.

## 3.2 Droplet tests under shear flow

In the present study, two sets of experiments were performed to characterize the depinning and breakup of surface-mounted droplets. All experiments were conducted in the experimental facility illustrated in Figure 3.1. Droplets of distilled water were deposited on the anodized aluminium substrate. The substrate was polished to 1000-grit and black-anodized. In all experiments, single droplets were placed on the plate surface at a stream-wise distance $X^* = 3.5B$ from the stagnation point using a micropipette. The flow speed was then

ramped to 20 m/s at given flow accelerations while the side-view and top-view images of the droplets were captured simultaneously. To improve the contrast of the side-view image, a cold diffused light from an LED light array was used as a back light. A fluorescent light tube was also used to provide additional illumination from above. Based on image calibration, an uncertainty of less than 7 μm was expected.

The droplet depinning tests were performed in order to determine the critical depinning velocity of the droplets being considered. Droplet volumes of 10, 50, 100, 200, 300, 400, 500 and 600 μl were studied using the method detailed above. Based on calibration, of the micropipette, the uncertainty in the droplet volume was estimated to be within 3.3% of the smallest droplet volume investigated (see Appendix B). The flow speed was ramped at a flow acceleration of 4.4 m/s$^2$. These tests were repeated fourteen times for each droplet volume. Two 2560 x 2160 pixel LaVision imager sCMOS cameras were used to capture the side-view and top-view profiles of the droplets simultaneously. Both cameras were synchronized and operating at an image acquisition rate of 100 Hz. The side-view camera was equipped with a 200 mm Nikon lens and had a spatial resolution of 69.8 px/mm. The top-view camera was equipped with a 50 mm Nikon lens with a resulting resolution of 12 px/mm. Corresponding imaging parameters are summarised in Table 3.1, and the respective fields of view are illustrated in Figure 3.4.

**Table 3.1:** Imaging parameters for $U_{\text{crit}}$ experiments.

| Parameter | Side-view | Top-view |
|---|---|---|
| FOV (mm$^2$) | 30.6 x 9.6 | 29.2 x 23.3 |
| Focal length (mm) | 200 | 50 |
| Resolution (px/mm) | 62.8 | 12.0 |
| Acquisition rate (Hz) | 100 | 100 |

The method employed to capture the droplet breakup behaviour was similar to that employed to quantify the critical depinning velocity of the droplets. The droplet volumes and flow accelerations considered in these experiments are detailed in Table 3.2. In these experiments, a micropipette with a larger volume output range was used. The uncertainty in droplet volume, based on calibration of the micropipette, was estimated to be within 2.1% of the smallest droplet volume investigated (see Appendix B). For each configuration, the tests were repeated 30 times. Top and side views of the droplet were captured simultaneously using four 2560 x 2160 pixel LaVision Imager sCMOS cameras equipped with Nikon 105 mm lenses (Figure 3.1). A pair of cameras was used each for the side and top views to extend the field-of-view (FOV) along the direction of droplet motion. Overlapping images acquired by each camera pair were stitched using a cosine weighted function. Table 3.3 summarises the imaging parameters, and the four FOVs are illustrated in Figure 3.5.
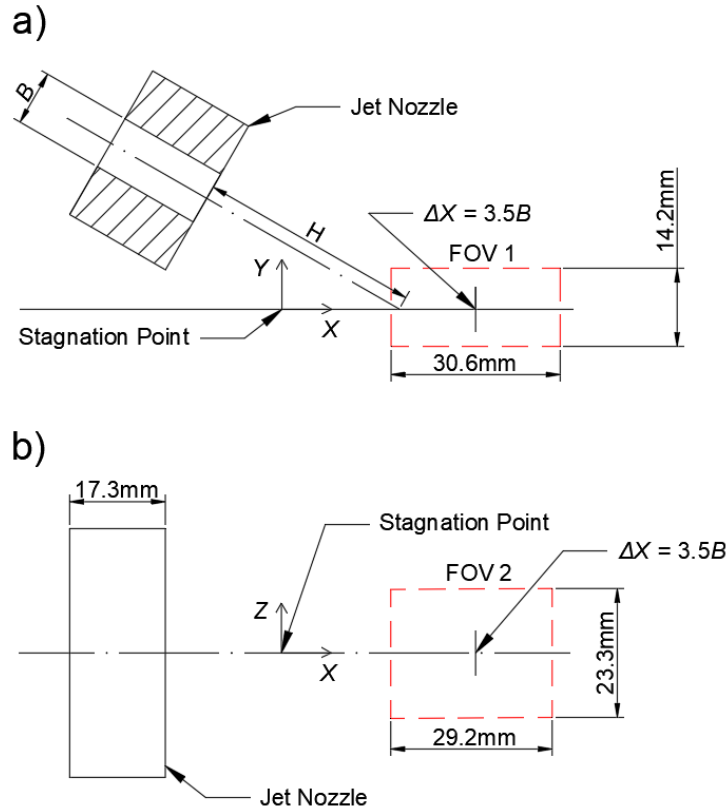
**Figure 3.4:** Experiment setup for $U_{\mathrm{crit}}$ experiments showing the employed a) side-view and b) top-view fields of view relative to the impinging jet nozzle. $\Delta X = 3.5B$ represents the initial droplet location.

**Table 3.2:** Test matrix for studying droplet breakup.

| Volume (µl) | Flow Acceleration (m/s$^2$) |
|:---:|:---:|
| 50 | 4.4 |
| 100 | 1.2, 2.2, 3.2, 4.4 |
| 200 | 4.4 |
| 300 | 4.4 |
| 400 | 4.4 |
| 500 | 4.4 |
| 600 | 1.2, 2.2, 3.2, 4.4 |

**Table 3.3:** Imaging parameters for studying droplet breakup.

| Parameter | Side-view | Top-view |
|---|---|---|
| Individual FOV (mm$^2$) | 90.6 x 14.2 | 90.6 x 25.58 |
| Combined FOV (mm$^2$) | 172.2 x 14.2 | 165.1 x 25.58 |
| Focal length (mm) | 105 | 105 |
| Resolution (px/mm) | 28.27 | 29.32 |
| Acquisition rate (Hz) | 120 | 120 |
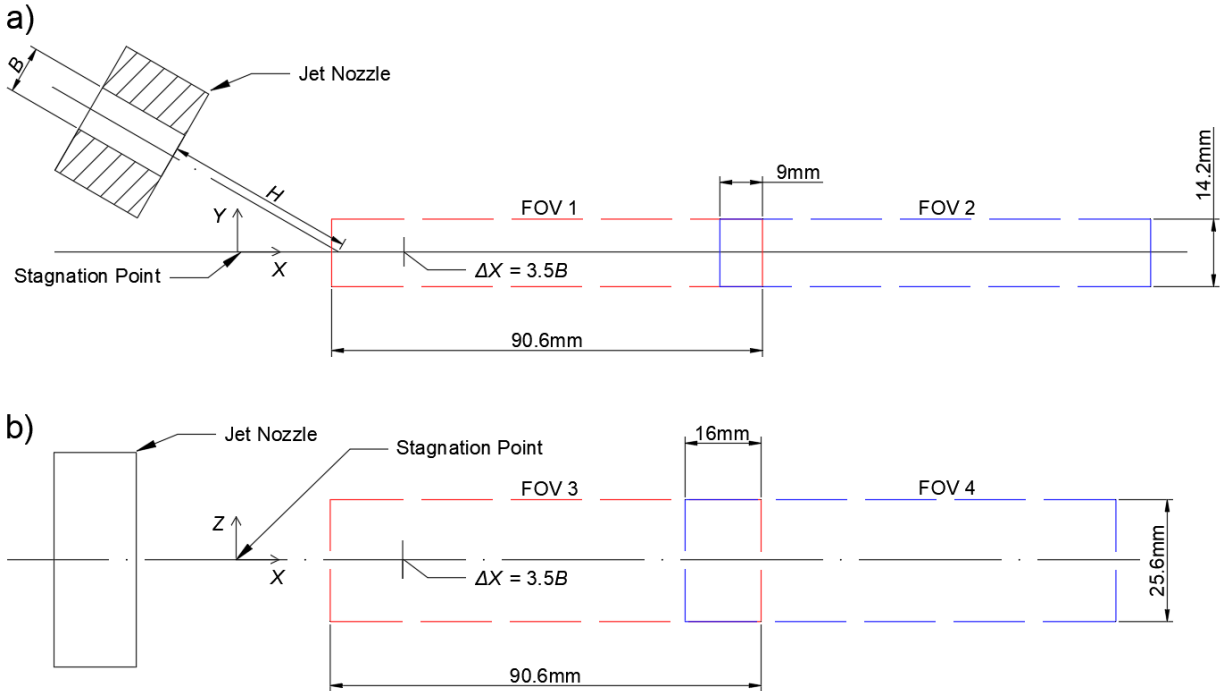


**Figure 3.5:** Experiment setup for breakup experiments showing the a) side-view and b) top-view FOV pairs relative to the impinging jet nozzle. $\Delta X = 3.5B$ represents the initial droplet location.

## 3.3 Image processing

Figure 3.6 illustrates a typical side-view (left) and top-view (right) droplet image of a sessile droplet. Figure 3.6 (a) and (b) identify the geometric parameters of interest that are estimated from the side-view and top-view images respectively. These include the upstream contact angle ($\theta_u$), downstream contact angle ($\theta_d$), droplet length ($l$), droplet height ($h$), and the droplet width ($w$). In order to extract these geometric parameters, a Canny edge detection using Otsu's threshold was first used to detect the droplet boundary [42]. Figure 3.6 (c) and (d) show the extracted droplet boundary overlaid on the sessile droplet snapshots from Figure 3.6 (a) and (b), respectively. The droplet boundary was
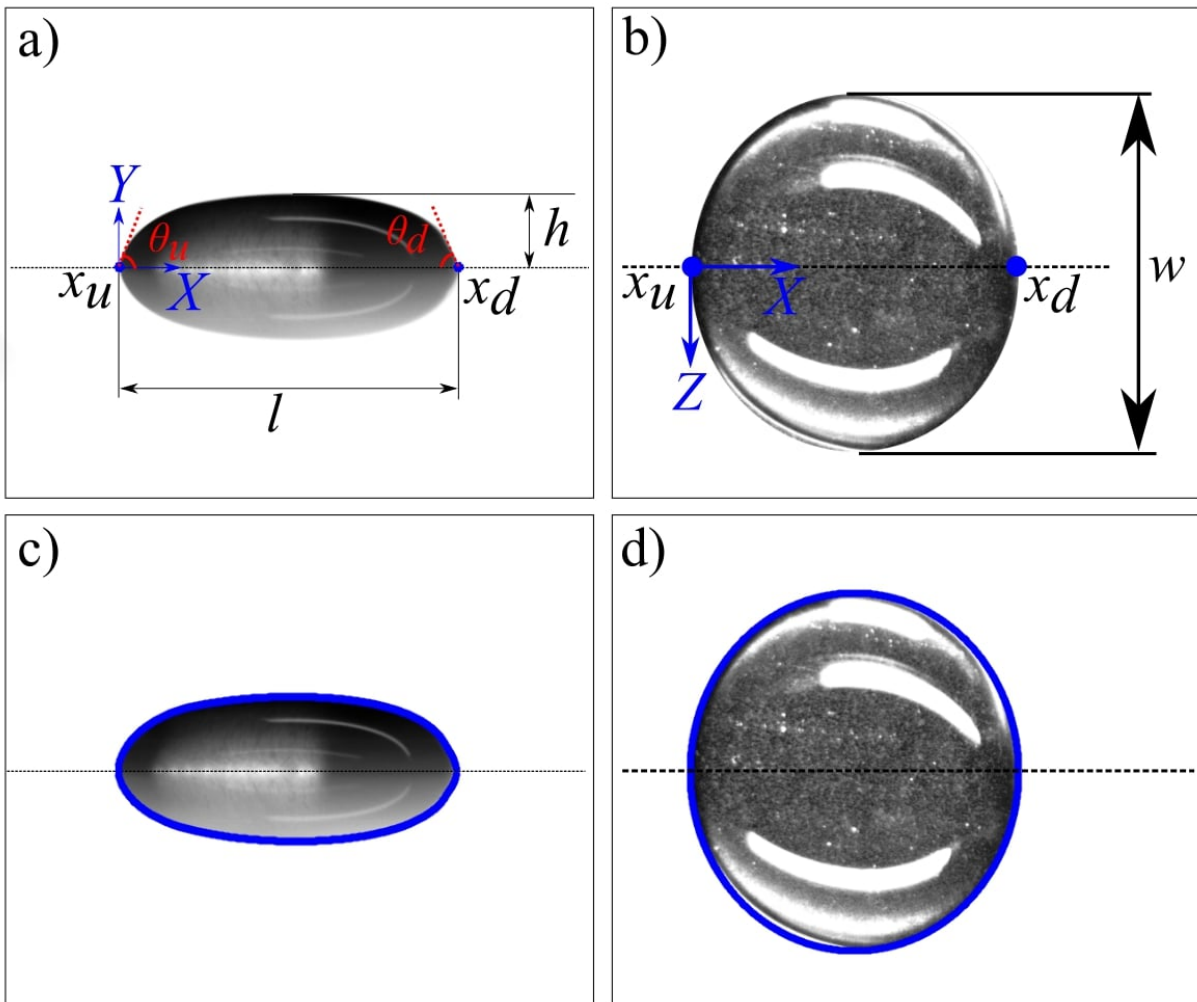


**Figure 3.6:** Side-view (a) and top-view (b) images of a sessile 600 µl droplet with geometric parameters annotated. Note that the side-view droplet image is reflected by the substrate. Overlaid droplet boundaries detected using canny edge detection are shown in (c) and (d). The droplet boundary was separated from the resulting binary canny edge map using a marching squares contour finding algorithm [12].

separated from the resulting binary canny edge map using a marching squares contour finding algorithm [12].

The contact point locations and contact angles were extracted from side-view images using the sub-pixel polynomial fitting (SPPF) method [12]. This approach involves first detecting the droplet boundary with pixel resolution using a Canny edge detection algorithm with Otsu's threshold [42]. The droplet boundary is then separated from the resulting binary Canny edge map using a marching squares contour finding algorithm as seen in Figure 3.6 (c) and (d) [12]. Afterwards, the droplet is divided into two segments (upstream and downstream segments) about its streamwise ($X$) centreline. Both contact points and contact angles are then found by applying the following steps to each of the two segments. For each $Y$-coordinate, along the droplet boundary, the corresponding $X$-coordinate of the droplet boundary is found with sub-pixel resolution. Specifically, a sigmoid is fit to the pixel intensity values along a horizontal (streamwise $X$) line crossing the droplet's boundary, and the saddle point of the sigmoid is identified as the coordinate of the droplet boundary. The location of the contact point is then found by extrapolating and intersecting the acquired droplet boundary points with the droplet's reflection. Finally, contact angles are calculated from the slope of a fitted second-order polynomial around the contact points. The polynomial is fit to the detected points along the droplet boundary which are near the contact point. The optimum number of points used in the polynomial fit is found by iteratively incrementing the number of points used in the fit. This is done until the measured contact angle changes by less than 0.1 degrees per unit change in the number of points used. For contact angles in the range of $10° \leq \theta_s \leq 160°$, as in the present study, the uncertainty associated with this approach is within 1 degree irrespective of the lightening conditions [12]. Using this method, average sessile contact angles across all cases were measured to be $81.8° \pm 2.4°$ (see Appendix B for uncertainty calculation). The droplet length ($l$) was measured as the streamwise ($X$) distance between the measured contact points. The droplet height ($h$) was measured with pixel accuracy to be the highest wall-normal ($Y$) distance of the droplet boundary from the average $Y$-position of both contact points. Lastly, the droplet width ($w$) was measured with pixel accuracy to be the maximum span of the droplet boundary along the $Z$-direction.

The measured average sessile length ($\bar{l}_0$) and average sessile height ($\bar{h}_0$) are plotted in Figure 3.7 for all the cases examined. It is seen that the sessile droplet length follows a power-law relationship with the droplet volume, with $\bar{l}_0 \sim V_0^{0.4}$, while the sessile droplet height exhibits a logarithmic relationship with volume, $\bar{h}_0 \sim 0.54\ln(V_0)$. These trends agree with previous studies [15][6], in which the droplet height is expected to plateau in the gravity-flattened droplet volume regime. This is further illustrated in Figure 3.8 in which the median contours for each droplet volume are shown. The characteristic change in the shape of droplets between the three volume regimes discussed in Section 2.3.1 is also seen. Top-view contours of the sessile droplets were also verified to follow a circular least-square fit with an average fit error below 1.4% of the droplet length. This points to homogeneous substrate characteristics and careful droplet placement.
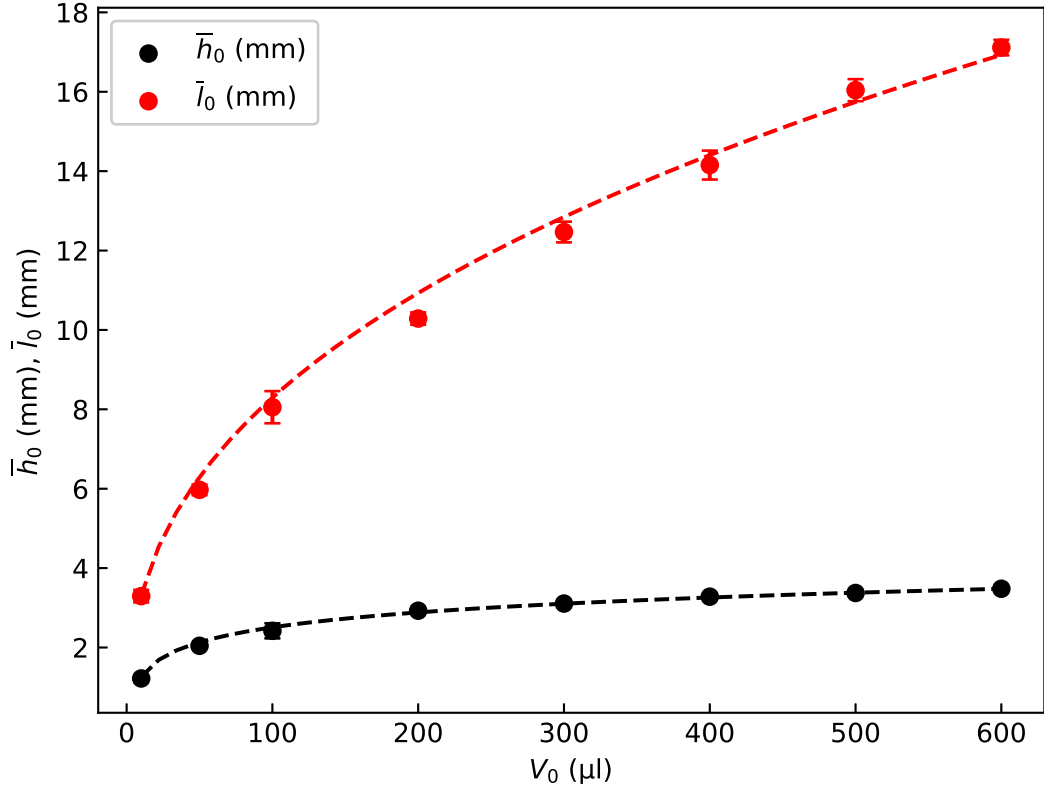
**Figure 3.7:** Sessile droplet dimensions. The red-dashed lines correspond to power-law ($\bar{l}_0 \sim V_0^{0.4}$) and logarithmic ($\bar{h}_0 \sim 0.54\ln(V_0)$) least-square fits applied to the corresponding plots. Error bars represent the corresponding uncertainty bounds (68% confidence).
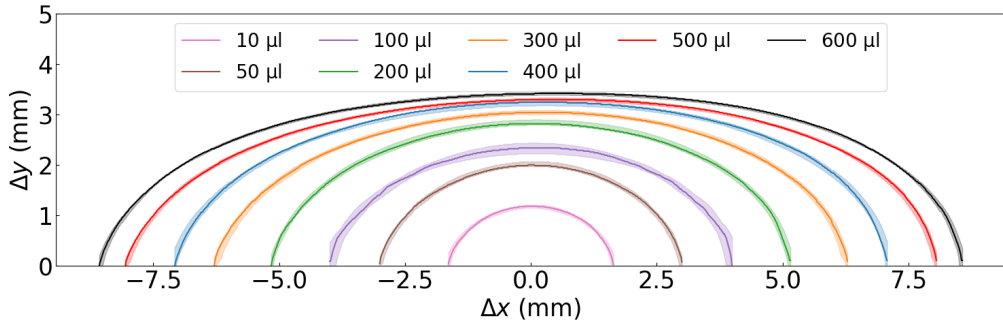


**Figure 3.8:** Median contours of droplets acquired in $U_{\mathrm{crit}}$ experiments (Section 3.2). Note that all profiles are centred horizontally at the origin. $\Delta x$ and $\Delta y$ represent the horizontal and vertical distances, respectively, from the common-centre. Error bars represent the inter-quartile range.

## 3.4 Volume estimation

In Section 4.4, the volume of child droplets was estimated by merging data from the top and side view measurements and performing a 3D droplet reconstruction. The side and top-view profiles of the droplet were extracted using the method detailed in Section 3.3. The droplet volume was then reconstructed with cross-sectional slices ($Y - Z$ planes) at each $X$-cordinate ($X_i$) within the droplet boundary. The cross-sectional slices were approximated as semi-ellipses as seen in Figure 3.9. The characteristic dimensions of each semi-ellipse were extracted from the droplet profiles. The semi-minor axis length corresponded to $h_i$,
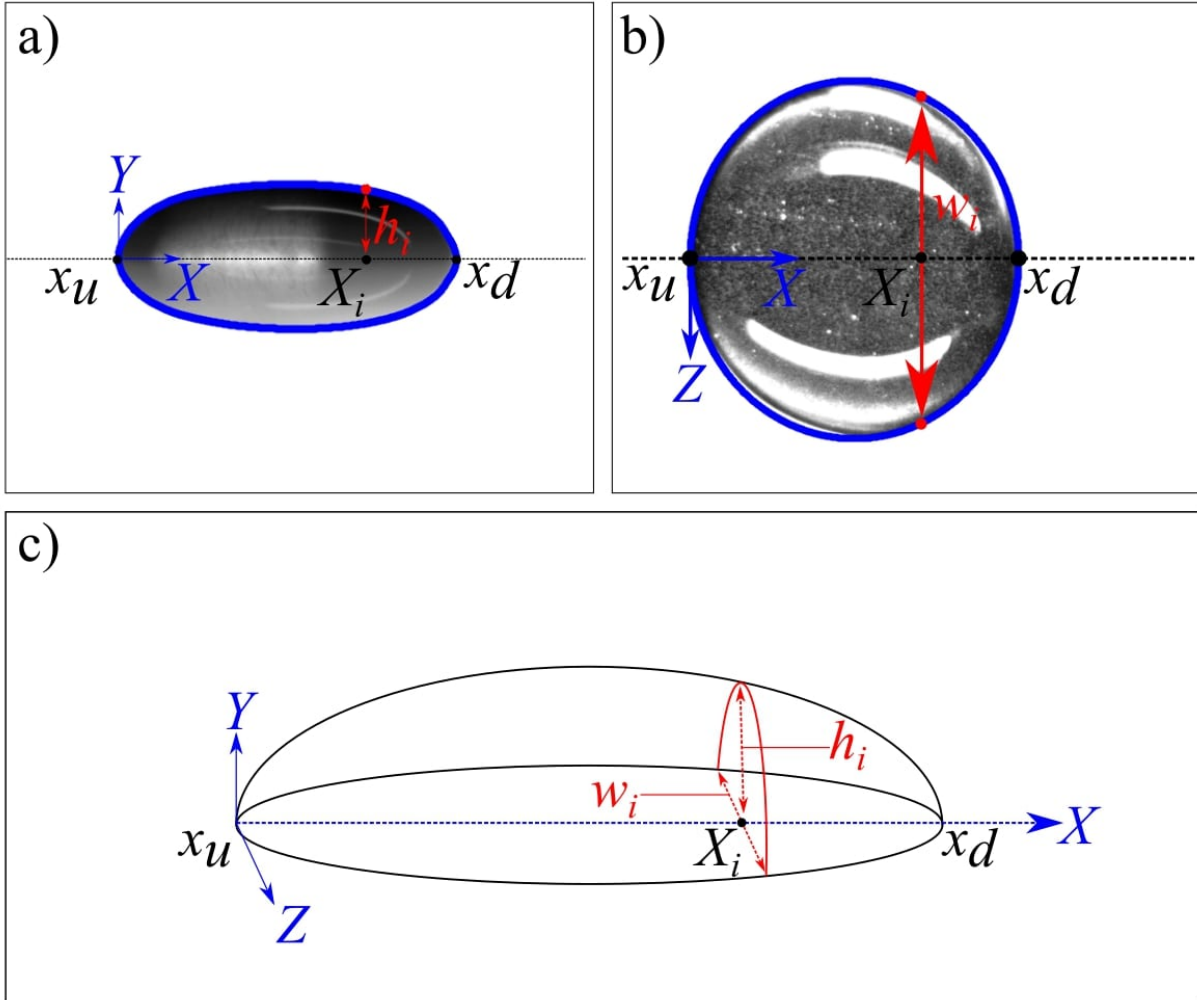


**Figure 3.9:** 3D droplet reconstruction process illustrated using side-view (a), and (b) top-view images of a sessile 600 µl droplet showing characteristic dimensions. Note that the side-view droplet image is reflected by the substrate. Overlaid droplet boundaries detected using canny edge detection are also shown [12]. (c) 3D schematic of the droplet showing semi-elliptical cross-sectional slice.

the $Y$-distance of the droplet boundary from the average $Y$-positions of both contact points. The major axis length corresponded to $w_i$, the $Z$-span of the droplet at the corresponding $X_i$. Figure 3.10 shows the resulting 3D reconstruction of the 600 µl droplet using this approach.
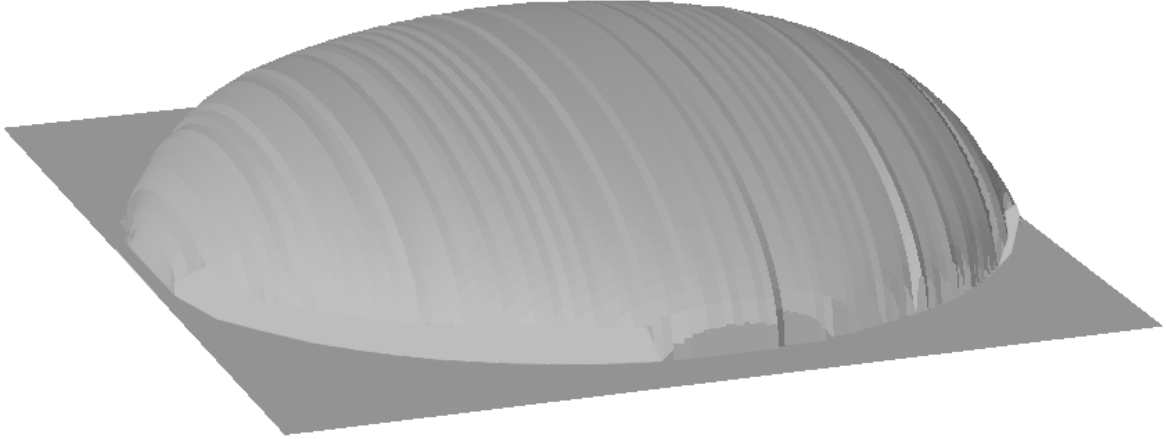


**Figure 3.10:** 3D reconstruction of a sessile 600 µl droplet.

Based on the 3D reconstruction, the droplet volume was computed as $V = \int_{x_u}^{x_d} 0.25\pi wh\,\mathrm{d}X$. This calculation was performed numerically using the trapezoidal rule as seen in Equation 3.1. The integration bounds were discretized with $\Delta X = 1$ px for $X \in [x_u, x_d]$. For the droplet volumes in the range 2 µl $\lesssim$ V $\lesssim$ 50 µl, this approach was estimated to result in an uncertainty of less than 10% (see Appendix B).

$$V = 0.125\pi\Delta X \sum_{i=1}^{N}(w_{i-1}h_{i-1}) + (w_i h_i) \tag{3.1}$$

# Chapter 4

# Results and Discussion

*This chapter discusses the depinning and breakup of surface-mounted droplets by an accelerating impinging jet flow. Section 4.1 illustrates the stages observed in the breakup process. Section 4.2 outlines the critical depinning conditions identified for the droplet volumes detailed in Section 3.2. Section 4.3 characterizes the necking and breakup of the droplets. Section 4.4 characterizes the child droplets which result from the droplets' breakup. Finally, Section 4.5 presents a summary and discussion of the findings of the chapter from a practical standpoint.*

## 4.1   Breakup process

An example of the breakup of a surface-mounted droplet is depicted in Figures 4.1 and 4.2 for droplet volumes 50 µl and 600 µl, respectively, at $\frac{dU_j}{dt} = 4.4$ m/s$^2$. As the flow speed increases, the droplet progressively deforms from its axisymettrical sessile shape (Figures 4.1 and 4.2 column 1, row 2). Eventually, the loading exceeds the adhesion force, and the droplet depins from its initial location (Figures 4.1 and 4.2 column 1, row 3). After depinning, the droplet elongates while moving downstream (Figures 4.1 and 4.2 rows 4 - 5). Eventually, necking starts, i.e., the droplet attains an hourglass shape (Figures 4.1 and 4.2 column 2, rows 6 - 10). Specifically, the top view profile of the droplet resembles two lobe-shaped segments, which are connected by a filament. The connecting filament continues to thin, and this process culminates in two, or more, smaller child droplets splitting off from the main droplet (Figures 4.1 and 4.2 rows 11 - 12). The presented sequence of images illustrates that the whole breakup process comprises three distinctive but continuous stages: depinning, necking, and breakup, which will be analyzed in the following sections.
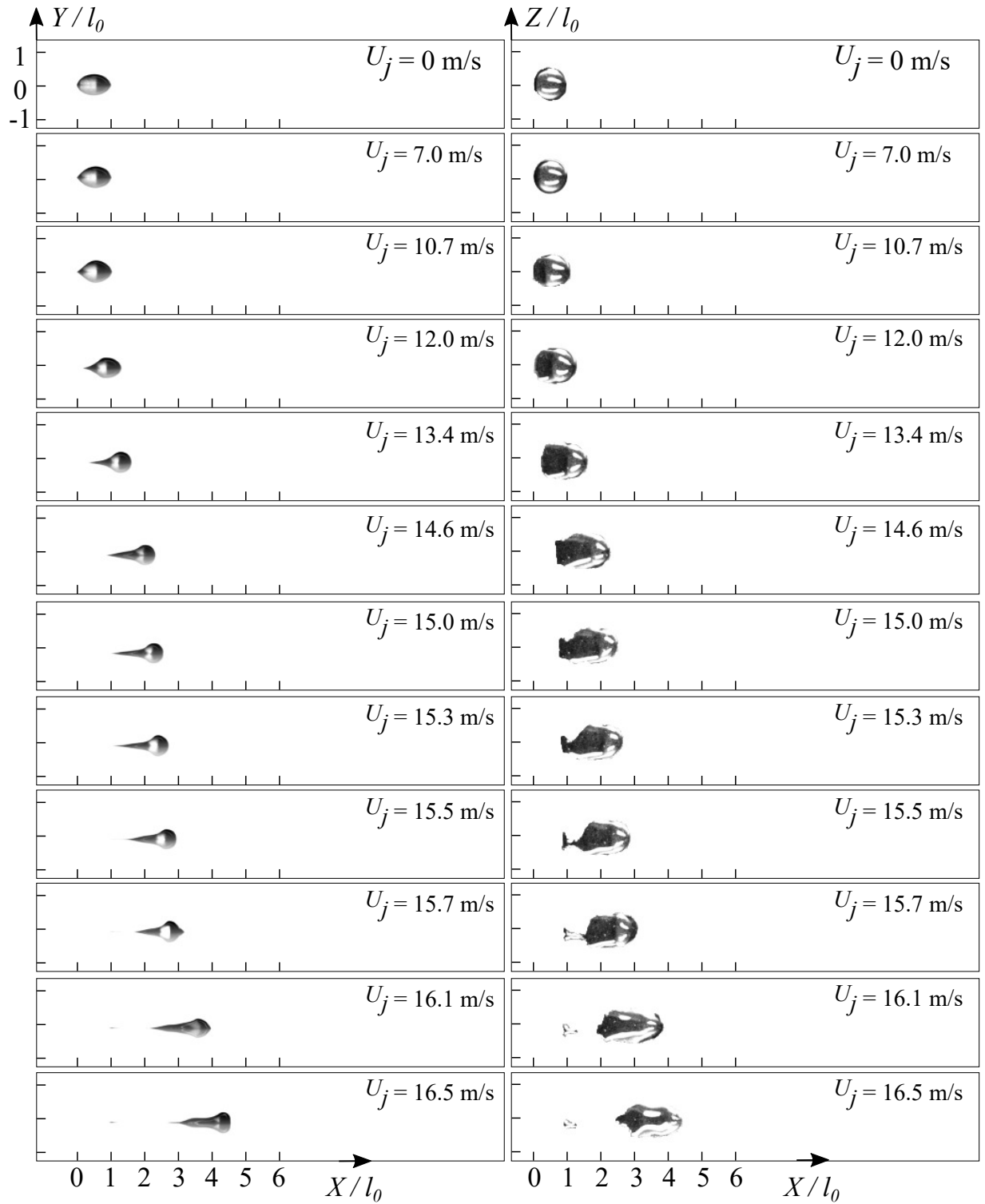
**Figure 4.1:** Typical side-view (left) and top-view (right) progression of breakup using a 50 µl droplet ($\frac{dU_j}{dt} = 4.4$ m/s$^2$).
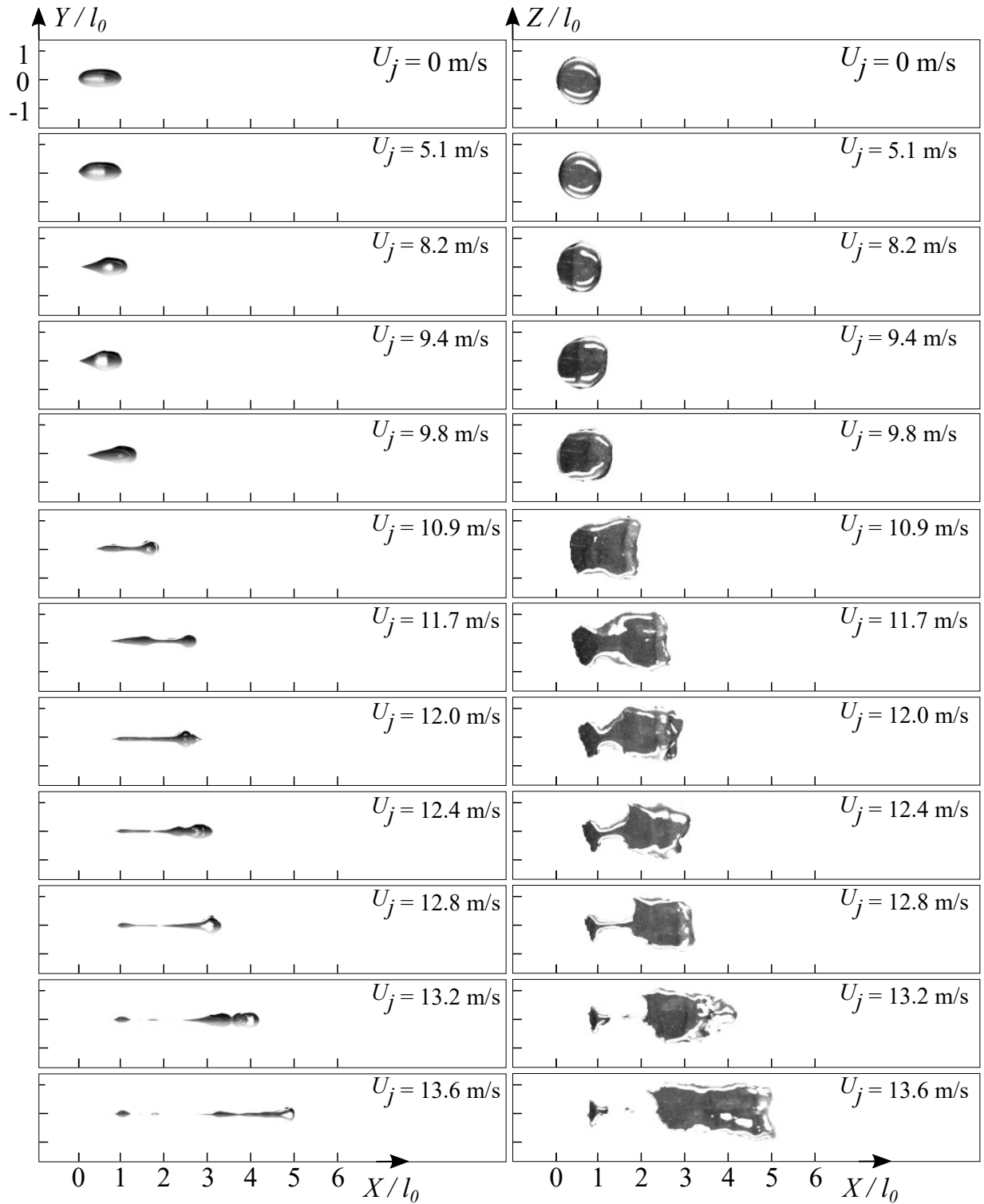
**Figure 4.2:** Typical side-view (left) and top-view (right) progression of breakup using a 600 µl droplet ($\frac{dU_j}{dt} = 4.4$ m/s$^2$).

## 4.2 Droplet depinning

Figure 4.3 shows typical upstream (receding) and downstream (advancing) contact point displacements in response to increasing jet velocity for $V_0 = 600$ µl and $\frac{dU_j}{dt} = 4.4$ m/s$^2$. As the flow velocity increases from zero, the contact points initially remain stationary. Increasing the flow velocity further ($U_j \gtrsim 4$ m/s) causes the downstream contact point to begin to move downstream while the upstream contact point remains stationary, which causes the droplet to elongate. When the flow velocity is increased further ($U_j \gtrsim 7$ m/s), the upstream contact point also begins to move downstream. Both contact points continue to move and accelerate with the flow as the droplet moves along the surface. The observed depinning process agrees with the results of other studies [5][70]. Similar to the approach taken in the previous investigations [70], the critical depinning velocity is defined here as that at which the upstream contact point begins to move continously. The critical depinning velocity ($U_{\text{crit}}$) was estimated from the side-view images to be the flow velocity at the time instant when the upstream contact point's displacement exceeded a set pixel displacement
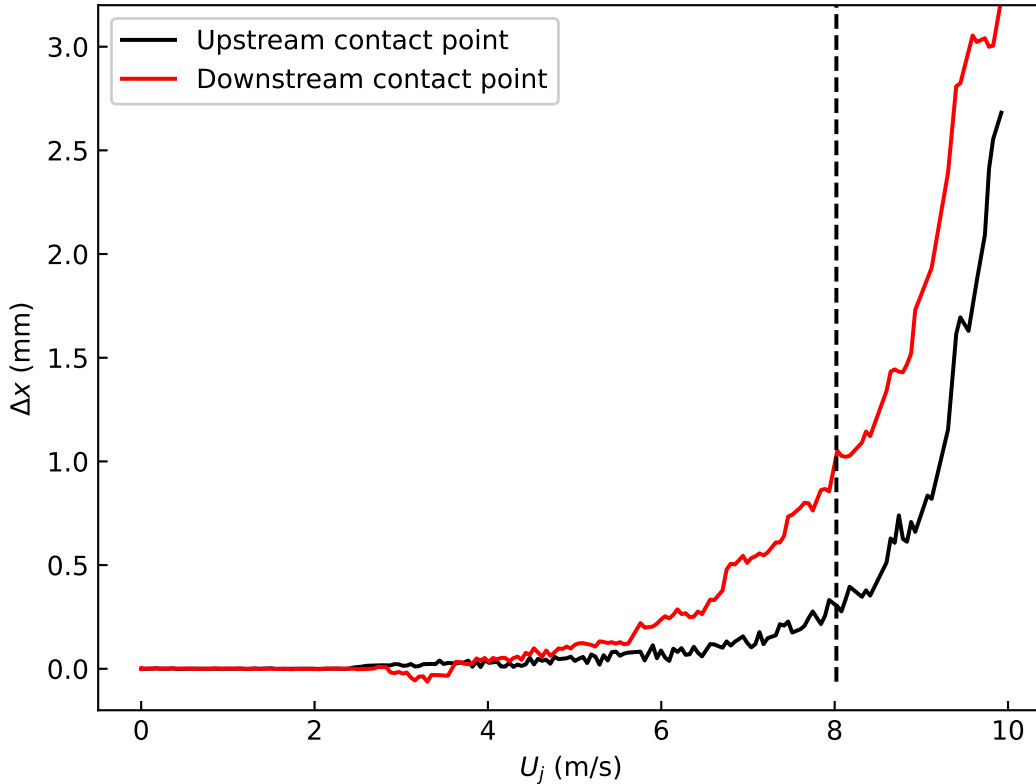


**Figure 4.3:** Contact point displacements using a 600 µl droplet ($\frac{dU_j}{dt} = 4.4$ m/s$^2$). The dashed line shows $U_{j,\text{crit}}$ estimated for this specific droplet test.

threshold. The pixel displacement threshold was selected such that, within the ensemble of test runs, the selection limits both the bias error arising from a more conservative choice of the displacement threshold and variations across the ensemble arising from too small of a threshold value. This approach is based on that proposed by Zhang [70] and is discussed in detail in Appendix A. The selected displacement thresholds in this study were in the range $23 \text{ px} \lesssim \Delta x_u \lesssim 25 \text{ px}$ (see Table A.1). The estimated $U_{j,\text{crit}}$ for the specific droplet test in Figure 4.3 is illustrated by the dashed line.

In this study, the critical depinning velocity associated with a sessile volume ($\overline{U}_{\text{crit}}$) is the ensemble of $U_{\text{crit}}$ estimates for each test in the volume configuration. The average critical depinning velocities are presented in Figure 4.4 for the investigated droplet volumes detailed in Section 3.2. Average depinning velocity ($\overline{U}_{h,\text{crit}}$) measurements by Zhang [70] which were taken in the same impinging jet facility at the same impinging angle and flow acceleration
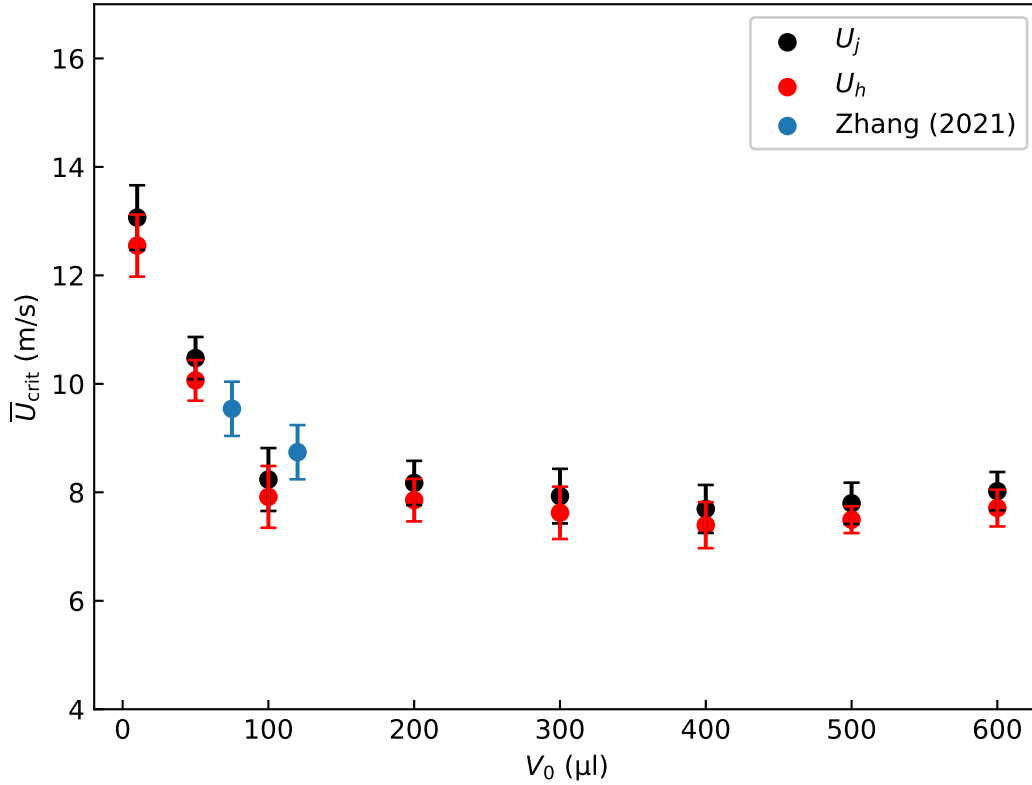


**Figure 4.4:** Critical depinning flow velocity measured at jet exit and droplet height for the range of droplet volumes tested ($\frac{dU_j}{dt} = 4.4 \text{ m/s}^2$). The blue markers represent $\overline{U}_{h,\text{crit}}$ measurements taken by Zhang [70] in the same impinging jet facility at the same impinging angle and flow acceleration as in the present study. Error bars represent the corresponding uncertainty bounds (68% confidence).

as this study are also included for comparison. For the range of tested droplet volumes, the critical depinning velocity measured at the jet exit ($U_{j,\text{crit}}$) is seen to be comparable to the critical depinning velocity measured at the droplet's height ($U_{h,\text{crit}}$), though it is higher, as expected. For sessile droplets within 10 µl $\lesssim V_0 \lesssim$ 100 µl, $\overline{U}_{\text{crit}}$ is seen to decrease with increasing droplet volume. However, for larger droplet volumes ($V_0 \gtrsim$ 100 µl), $\overline{U}_{\text{crit}}$ is seen to remain nearly constant ($\overline{U}_{h,\text{crit}} \approx$ 8 m/s). Similar to the findings of White et al. [63], most of these droplet volumes fall in the gravity flattened regime where the sessile droplet height does not vary appreciably with droplet volume ($\overline{h}_0 \approx$ 3 mm in the present study). Note, the measurements by Zhang were taken for droplets which were deposited further downstream at $X^* = 5B$. They are seen to have a slightly higher $\overline{U}_{h,\text{crit}}$ compared to droplets of similar volume in this study. This is due to the lower effective velocity across the droplet height resulting from the streamwise decay of flow momentum in impinging jet flows [70]. Furthermore, the displacement threshold used in this study was slightly higher than that used by Zhang (see Appendix A). Consequently, the $\overline{U}_{h,\text{crit}}$ measurements
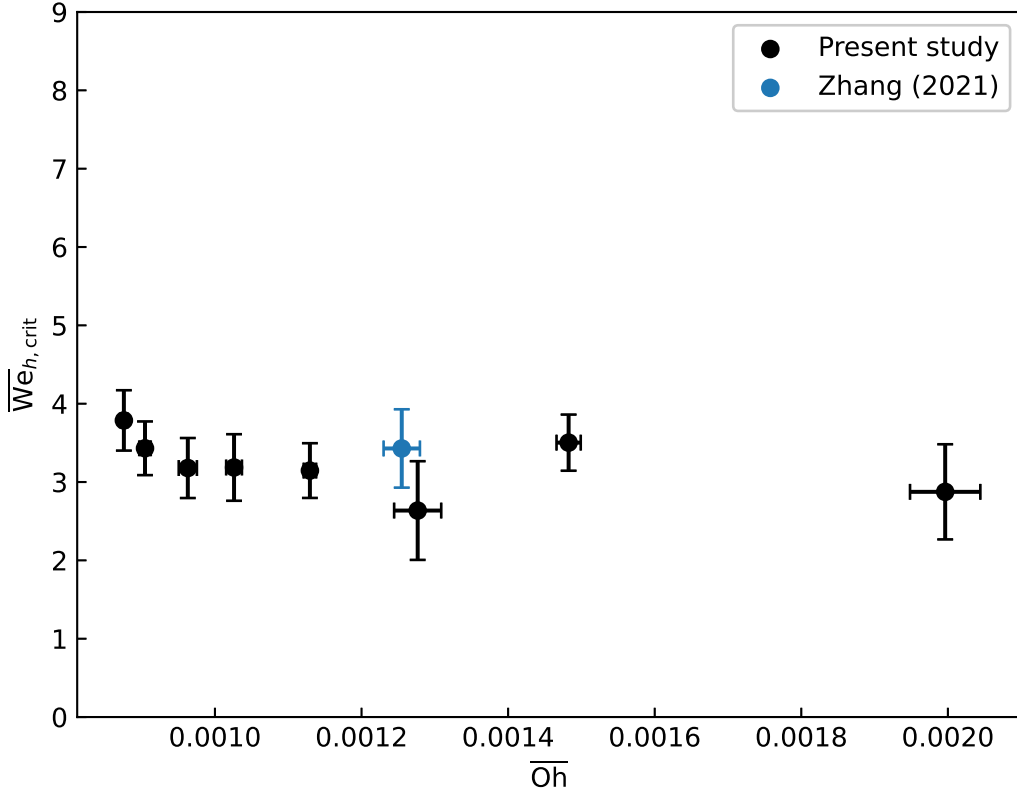


**Figure 4.5:** Critical Weber number for droplet depinning over the range of Oh tested ($\frac{dU_j}{dt} = 4.4$ m/s$^2$). The blue markers represent measurements taken by Zhang [70] in the same impinging jet facility, at the same impinging angle, and flow acceleration as this study. Error bars represent the corresponding uncertainty bounds (68% confidence).

by Zhang might be even higher, however this difference is not expected to be significant. Beyond a distance of $5B$ from the impinging point, increasing differences between $U_j$ and $U_h$ are expected due to a progressive decay in the maximum wall jet velocity [70].

Figure 4.5 presents the average Weber number ($\overline{\mathrm{We}}_{h,\mathrm{crit}}$) for droplet depinning ($\mathrm{We}_{h,\mathrm{crit}} = \frac{\rho U_{h,\mathrm{crit}}^2 h_{\mathrm{crit}}}{\gamma}$, where $\rho$ is the density of air, $h_{\mathrm{crit}}$ is the measured height of the droplet averaged over 40 ms prior to depinning, and $\gamma$ is the surface tension of the water droplet). The $\mathrm{We}_{h,\mathrm{crit}}$ is plotted against the average Ohnesoge number ($\overline{\mathrm{Oh}}$) of the droplets ($\mathrm{Oh} = \frac{\mu_{\mathrm{drop}}}{\sqrt{\rho_{\mathrm{drop}}\gamma l_0}}$, where $\mu_{\mathrm{drop}}$ is the dynamic viscosity of the droplet and $\rho_{\mathrm{drop}}$ is the density of the droplet). It is seen that droplets in the present study depinned within the Weber number range of $3 \lesssim \overline{\mathrm{We}}_{h,\mathrm{crit}} \lesssim 4$ when exposed to impinging jet flow. Although $\overline{\mathrm{We}}_{h,\mathrm{crit}}$ showed a minor decreasing trend with increasing $\overline{\mathrm{Oh}}$, the variation is within the experimental uncertainty. The results by Zhang [70], which were taken at the same impinging angle as
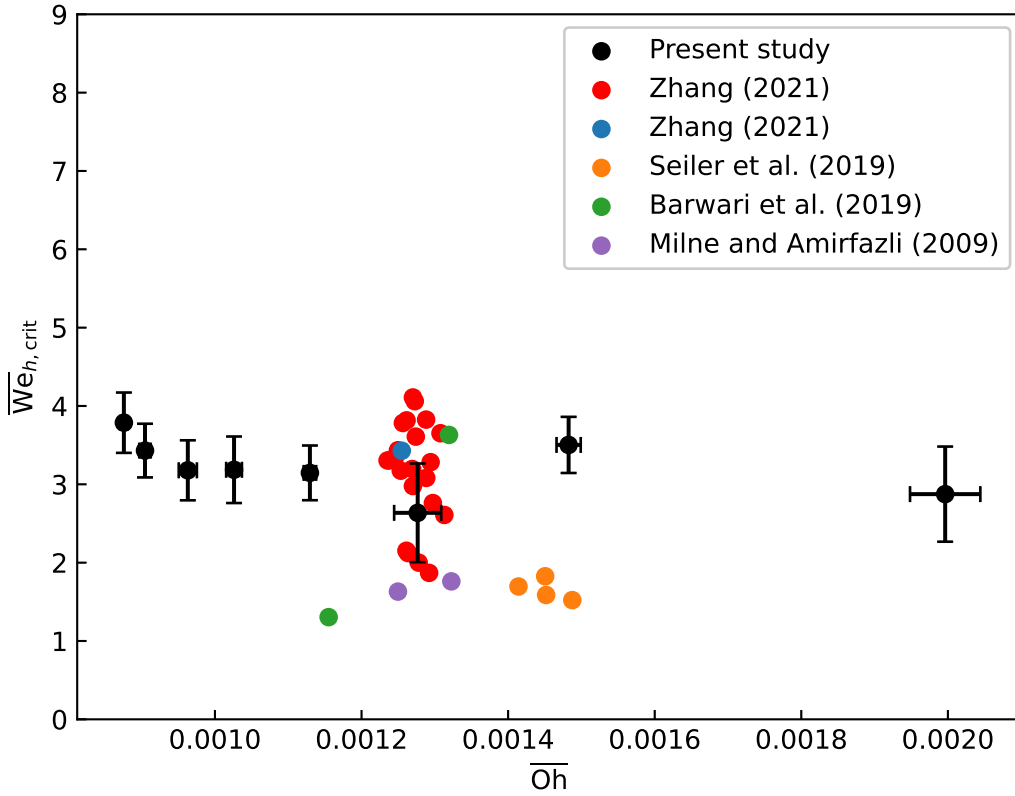


**Figure 4.6:** Critical Weber number for droplet depinning vs Oh. The light red and blue markers represent measurements taken by Zhang [70] in the same impinging jet facility at the same flow acceleration as this study. The blue markers were measured at the same impinging angle as this study. Error bars represent the corresponding uncertainty bounds (68% confidence).

this study, are comparable to those in the present study. However, these droplets depinned at slightly higher $\overline{\text{We}}_{h,\text{crit}}$ than droplets of similar $\overline{\text{Oh}}$ in this study. This is primarily due to their higher $U_{\text{crit}}$.

Figure 4.6 shows $\overline{\text{We}}_{h,\text{crit}}$ vs $\overline{\text{Oh}}$ with data from a wider range of studies [55][4][35] within the considered Oh range. Additional measurements by Zhang [70], which were taken at the same flow acceleration but varying impinging angles (light red markers), are also included for comparison. The measurements by Zhang [70] which were taken at other impinging angles, depinned in a slightly wider Weber number range ($2 \lesssim \overline{\text{We}}_{h,\text{crit}} \lesssim 5$) for very similar Ohnesoge number ($\overline{\text{Oh}} \approx 1.28 \times 10^{-3}$). This is most likely due to the effect of the impinging angle on the critical depinning velocity of the droplets. Zhang [70] found that within the range $30° \lesssim \theta_j \lesssim 60°$, the critical depinning velocity experienced a slight increase with increasing $\theta_j$ while droplets exposed to a normally impininging jet ($\theta_j = 90°$) experienced noteably lower critical depinning velocity. The results from other studies, on the other hand, depinned at a lower $\overline{\text{We}}_{h,\text{crit}}$ ($\text{We}_{h,\text{crit}} \approx 2$). This is attributed to the lower hydrophilicity ($0.15 \lesssim \text{CAH} \lesssim 0.63$) of the substrates used in the other studies, compared to the present study ($\text{CAH} \approx 0.7$). This results in a lower maximum adhesion force and a higher effective area for loading. Consequently, less hydrophilic substrates are known to result in a lower $U_{\text{crit}}$ [35].

## 4.3  Droplet necking and breakup

Figure 4.7 highlights the necking and breakup process seen for the droplets in the present study using the 50 µl (left) and 600 µl (right) droplets at $\frac{dU_j}{dt} = 4.4$ m/s$^2$. Figures 4.7 (a) and (b) show snapshots of the selected droplets' top-view images at various jet exit velocities through the necking process and breakup. The reported $U_j$ is normalized by the average depinning velocity ($\overline{U}_{j,\text{crit}}$) for the droplet volume. After depinning, the droplets continue elongating and their top-view outlines progressively deviate from their circular sessile shape to resemble a rounded rectangle, which has a relatively uniform width distribution (Figures 4.7 (a) and (b), row 1). As the elongation progresses, necking eventually begins as a precursor to breakup (Figure 4.7 (a) and (b), row 2). At this point, the top-view profile of the droplet begins to attain an hourglass shape. Specifically, a localized reduction of the droplet's span is seen in the previously uniform width distribution in Figures 4.7 (a) and (b), row 1. The necking continues to progress with the localized reduction in width becoming more prominent (Figure 4.7 (a) and (b), rows 3 - 6). As the necking becomes more pronounced, the top profile of each droplet resembles two lobe-shaped segments at both streamwise ends, which are connected by a filament. The filament continues to thin, and this process culminates in the droplet breaking up (Figure 4.7 (a) and (b), row 7).

Based on the observed changes to the droplet's geometry during necking, the minimum width ($w_{\text{min}}$) of the droplet was selected as a geometric parameter for quantifying the onset of the process. This metric is commonly used to study the necking of pendant droplets [19][13]. In this study, the minimum droplet width is defined as the tenth-percentile of the droplet's width distribution. Figures 4.8 (a) - (d) present the variation of the minimum
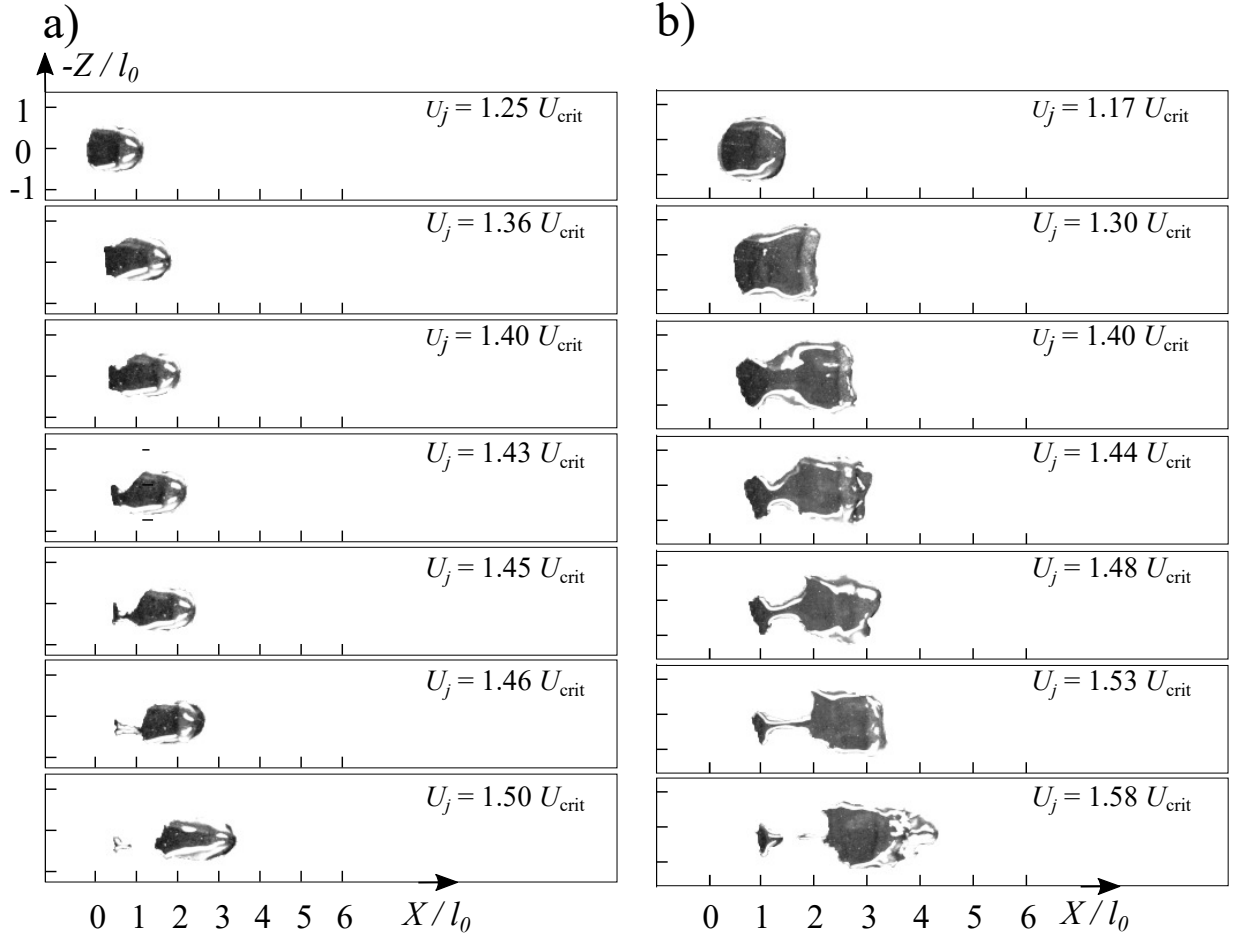
**Figure 4.7:** (a) and (b) Necking of a 50 µl (left) and 600 µl (right) droplet illustrated by snapshots.

droplet width (droplet extent in $Z$ direction) for the droplets in the present study using the 50 µl (left) and 600 µl (right) droplets at $\frac{dU_j}{dt} = 4.4$ m/s$^2$. The results are normalized by the length of the corresponding sessile droplets and $U_j$ is normalized by $\overline{U}_{j,\text{crit}}$. As the top-view profile of the droplet expands towards a rounded rectangular shape, a continuous increase in $w_{\min}$ is seen. Eventually, $w_{\min}$ exhibits a continuous decline during necking until breakup, similar to other studies [19][13]. Consequently, the onset of necking in this study is identified as the onset of the continuous decline in $w_{\min}$. For each test, the onset of necking was defined as the peak in $w_{\min}(\text{t})$ prior to breakup. The peak was found by progressively applying quadratic fits to a sliding data window on $w_{\min}(\text{t})$. The peak was then determined as the maxima of the maximum values recorded across all fits. The identified flow velocity for the onset of necking is shown with dashed vertical lines in Figure 4.8 (a) and (b). Figure 4.8 (c) and (d) shows the variation of the ensemble averaged $\overline{w}_{\min}$ for the same volumes. For each test case, $w_{\min}$ was normalized by the sessile length of the droplet before being averaged. The reported $U_j$ is normalized by $\overline{U}_{j,\text{crit}}$ of the corresponding droplet volume. A similar progression is seen in the ensemble averages, indicating the consistency
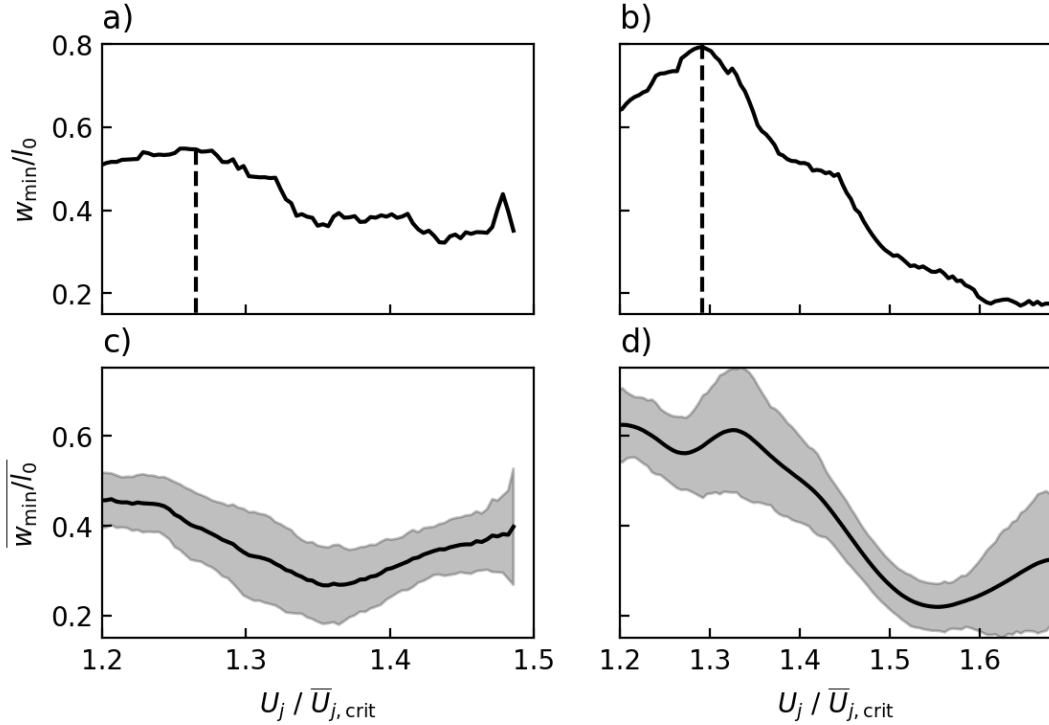
**Figure 4.8:** Necking of a 50 µl (left) and 600 µl (right) droplet illustrated by (a) and (b) minimum width vs flow velocity of an individual test, and (c) and (d) an ensemble average of all tests in the aforementioned configurations. Note that the dashed vertical lines in (a) and (b) indicate the onset of necking. Ensemble spreads in (c) and (d) indicate one standard deviation.

of the process across the 30 runs conducted in each configuration. However, due to the variability between runs, a clear peak is not discernible from the ensembles.

Figure 4.9 shows the variation of the ensemble averaged $\overline{w}_{\min}$ for the cases examined at $\frac{dU_j}{dt} = 4.4$ m/s². Prior to averaging, the $w_{\min}$ of each test run was normalized by the corresponding $l_0$. The reported $U_j$ is normalized by the corresponding $\overline{U}_{j,\text{crit}}$ of the droplet volume. The results show a similar progression of $\overline{w}_{\min}$ through the necking process as was seen in Figure 4.8 (a) and (b) irrespective of the droplet volume. This shows the consistency of the process across the droplet volumes tested. The ensemble averaged $\overline{w}_{\min}$ increases continously before plateauing. Eventually, necking begins and a continous decline is seen until breakup. However, similar to Figure 4.8 (c) and (d), the peak which indicates the onset of necking is smeared due to the variability across runs. This is particularly the case for the 600 µl droplets.

For each trial, the flow velocity at the onset of necking ($U_{\text{neck}}$) was estimated as the flow velocity that resulted in the peak in $w_{\min}$ versus $U_j$ (see Figure 4.8 (a) and (b)) for each configuration. Figure 4.10 (a) shows the average flow velocity for the onset of necking ($\overline{U}_{\text{neck}}$) for each tested sessile volume and flow acceleration. A similar trend to that of
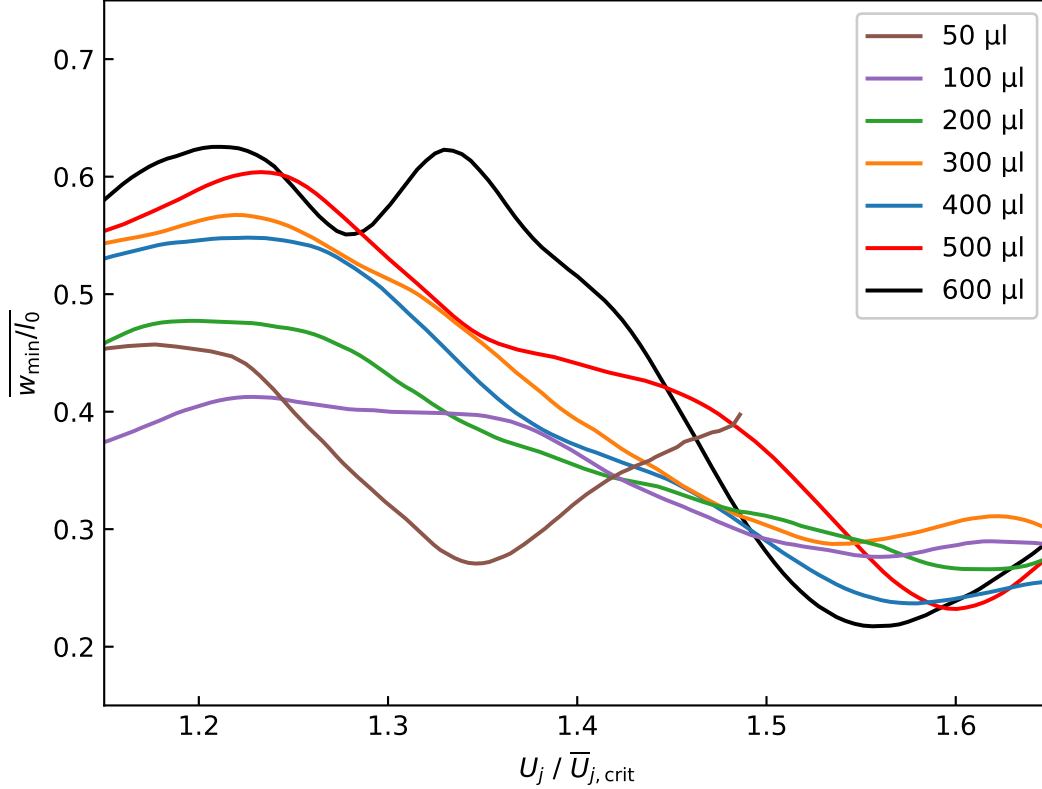
**Figure 4.9:** Necking of droplet width for the range of volumes tested ($\frac{dU_j}{dt} = 4.4$ m/s$^2$). Note that each curve represents an ensemble average of all tests for a given configuration. To improve clarity, the ensemble spreads are not shown (see Figure C.3).

Figure 4.4 is seen where $\overline{U}_{\text{neck}}$ appears to decrease with volume in the range $V_0 \lesssim 100$ µl but remains relatively constant for $V_0 \gtrsim 100$ µl. For the flow accelerations investigated, it is also seen that $\overline{U}_{\text{neck}}$ shows minimal variation with the flow acceleration. Figure 4.10 (b) shows the corresponding average Weber number for the onset of necking ($\overline{\text{We}}_{h,\text{neck}}$) for each tested configurations ($\text{We}_{h,\text{neck}} = \frac{\rho U_{h,\text{neck}}^2 h_{neck}}{\gamma}$, where $h_{\text{neck}}$ is the maximum height of the droplet at the onset of necking). It is seen that for the highest flow acceleration ($\frac{dU_j}{dt} = 4.4$ m/s$^2$), $\overline{\text{We}}_{h,\text{neck}}$ is relatively constant irrespective of the droplet volume ($\overline{\text{We}}_{h,\text{neck}} \approx 5.5$). Similarly, the $\overline{\text{We}}_{h,\text{neck}}$ for $V_0 = 600$ µl shows very little variation ($5.3 \lesssim \overline{\text{We}}_{h,\text{neck}} \lesssim 6.3$) over the investigated flow accelerations. For the 100 µl droplets, on the other hand, $\overline{\text{We}}_{h,\text{neck}}$ is seen to decrease gradually within the range $3.8 \lesssim \overline{\text{We}}_{h,\text{neck}} \lesssim 5.3$ with decreasing flow accelerations. However, these changes in $\overline{\text{We}}_{h,\text{neck}}$ are within the experimental uncertainty bounds.

Figure 4.11 highlights the final stages of breakup using side-view (left) and top-view (right) snapshots of the 600 µl droplet at $\frac{dU_j}{dt} = 4.4$ m/s$^2$. In the final stages of necking

**Figure 4.10:** a) Jet exit velocity, local velocity and b) Weber number for onset of droplet necking for the range of droplet volumes and flow accelerations tested. Note that different flow accelerations are shown with a slight volume offset for clarity for 100 µl and 600 µl droplets. Filled markers in a) represent $U_h$ while empty markers represent $U_j$. Error bars represent the corresponding uncertainty bounds (68% confidence).

(Figure 4.11 column 2, row 1), the filament connecting the two lobe-shaped segments of the droplet becomes very thin. Shortly after, the filament snaps (Figure 4.11 row 2) and the larger main droplet continues to move downstream while two, or more, resulting smaller child droplets remain stationary (Figure 4.11 row 3). In the present study, droplet breakup detection relied on estimates from both side and top FOVs. For each FOV, it was estimated to occur when more than one distinct droplet contour was detected within that specific FOV for the first time as seen in the second row of Figure 4.11. For a given run, $U_{br}$ is estimated to be the average of the flow velocities at which breakup is detected in the side and top FOVs.

The average flow velocity at which breakup occurs ($\overline{U}_{br}$) is plotted in Figure 4.12 (a) for all sessile volumes and flow accelerations considered in Table 3.2. Similar to the onset of necking, smaller droplets ($V_0 \lesssim 200$ µl) are seen to breakup at progressively higher flow velocities, whereas the breakup of larger droplets ($V_0 \gtrsim 200$ µl) occurs at a nearly constant
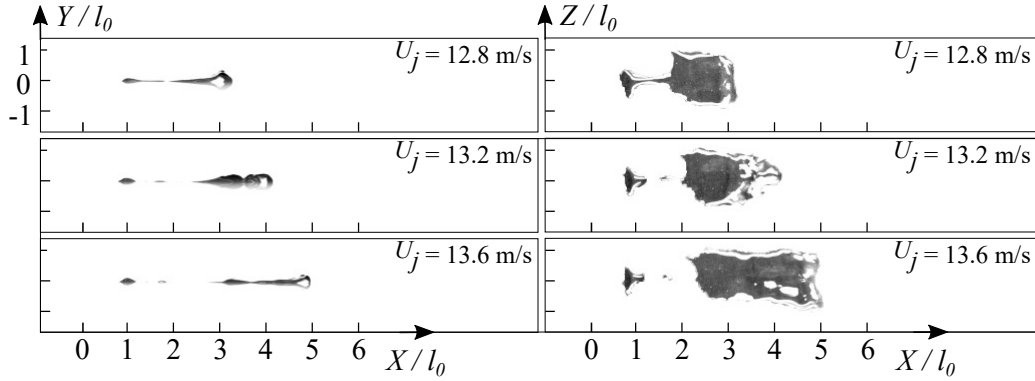
**Figure 4.11:** Progression of final stages of breakup of a 600 µl droplet ($\frac{dU_j}{dt} = 4.4$ m/s$^2$).

flow velocity. It is also seen that droplets exposed to a lower flow acceleration breakup at lower flow velocities. Figure 4.12 (b) shows the corresponding average Weber number at which breakup occurs ($\overline{\mathrm{We}}_{h,\mathrm{br}}$) for each tested configuration. The Weber number for breakup is defined as $\mathrm{We}_{h,\mathrm{br}} = \frac{\rho U_{h,\mathrm{br}}^2 h_{br}}{\gamma}$, where $h_{\mathrm{br}}$ is the maximum height of the droplet immediately prior to the detected breakup. For the highest flow accelerations tested ($\frac{dU_j}{dt} = 4.4$ m/s$^2$) the mean values across all trials fall between $6.5 \lesssim \overline{\mathrm{We}}_{h,\mathrm{br}} \lesssim 7.5$ and remain invariant with the droplet volume. Decreasing flow acceleration decreases $\overline{\mathrm{We}}_{h,\mathrm{br}}$ for a given sessile volume. However, this decrease in $\overline{\mathrm{We}}_{h,\mathrm{br}}$ across all tested flow accelerations is within the experimental uncertainty. Altogether, $\overline{\mathrm{We}}_{h,\mathrm{br}}$ aopears to be relatively invariant with sessile volume and flow acceleration for the range of parameters tested in the present study.

Figure 4.13 presents $\overline{\mathrm{We}}_{h,\mathrm{br}}$ versus $\overline{\mathrm{Oh}}$ for all tests conducted in the present study and other studies that reported breakup of surface-mounted droplets [18][4] over an extended range of $8.8 \times 10^{-4} \leq \overline{\mathrm{Oh}} \leq 6.9 \times 10^{-2}$. It is seen that for $\overline{\mathrm{Oh}} \lesssim 5.3 \times 10^{-2}$, $\overline{\mathrm{We}}_{h,\mathrm{br}}$ is nearly invariant with $\overline{\mathrm{Oh}}$ ($\overline{\mathrm{We}}_{h,\mathrm{br}} \approx 7$). Beyond this range, $\overline{\mathrm{We}}_{h,\mathrm{br}}$ is seen to increase with increasing $\overline{\mathrm{Oh}}$. This is because the viscous forces inside the droplet hinder its deformation [68]. The red dashed line represents a power law fit ($\overline{\mathrm{We}}_{h,\mathrm{br}} \sim \overline{\mathrm{Oh}}^{4.9}$) applied to the data pertaining to the breakup of surface-mounted droplets. The selection of a power-law fit is motivated by an emperical correlation of Brodkey [7]. This correlation showed that the transitional Weber numbers for the onsets of each breakup mode of free-falling droplets follow a power-law relationship with $\overline{\mathrm{Oh}}$. The black dashed line represents the transitional Weber number for the onset of bag breakup in free-falling droplets based on Brodkey's correlation [7]. The dotted line represents the Weber number from the study by Hsiang et al. [27] above which oscillatory deformation is expected for free falling droplets in a shock tube. Beyond a certain threshold, Huang et al. observed droplets deforming so that the ratio of their cross stream dimension to initial diameter was 1.1, corresponding to a deformation of 10%. The oscillatory deformation regime occured at slightly higher We than this threshold for $\overline{\mathrm{Oh}} < 0.4$. In this We regime, droplets oscillated with progressively decaying ratios of maximum to initial diameters before the bag breakup regime was reached. Overall, it is seen that surface-mounted droplets break up in the vibrational breakup and oscillatory deformation Weber number regime of free-falling droplets. Furthermore, the

41

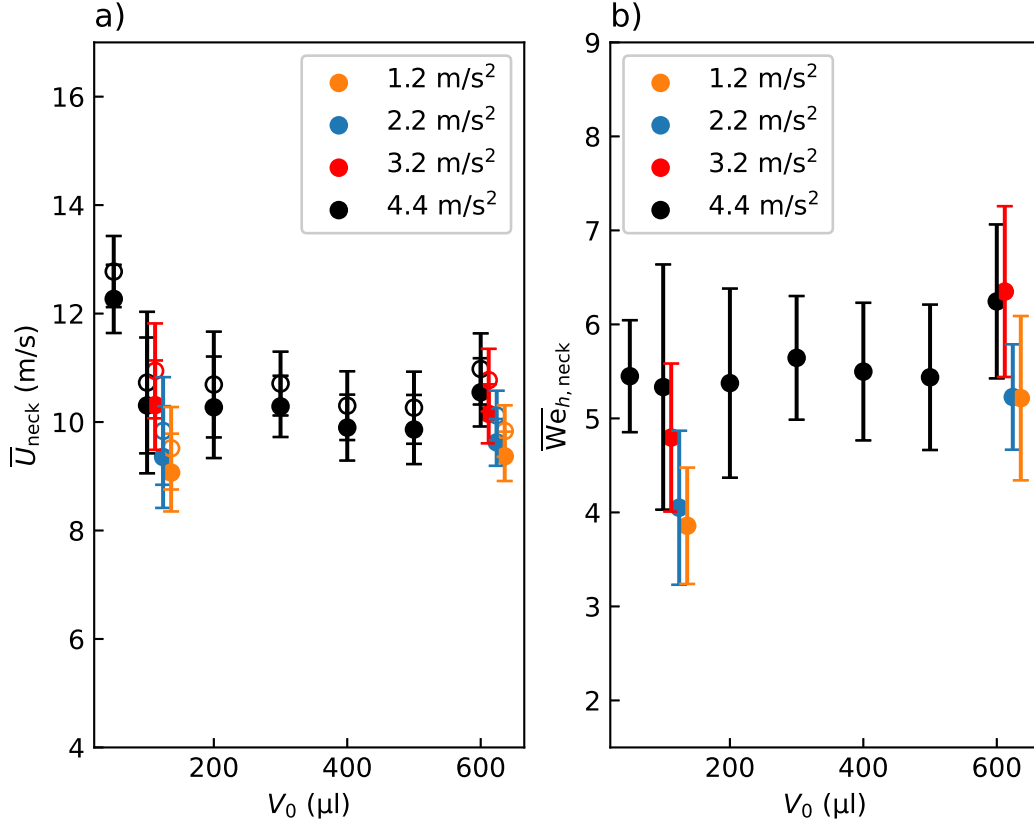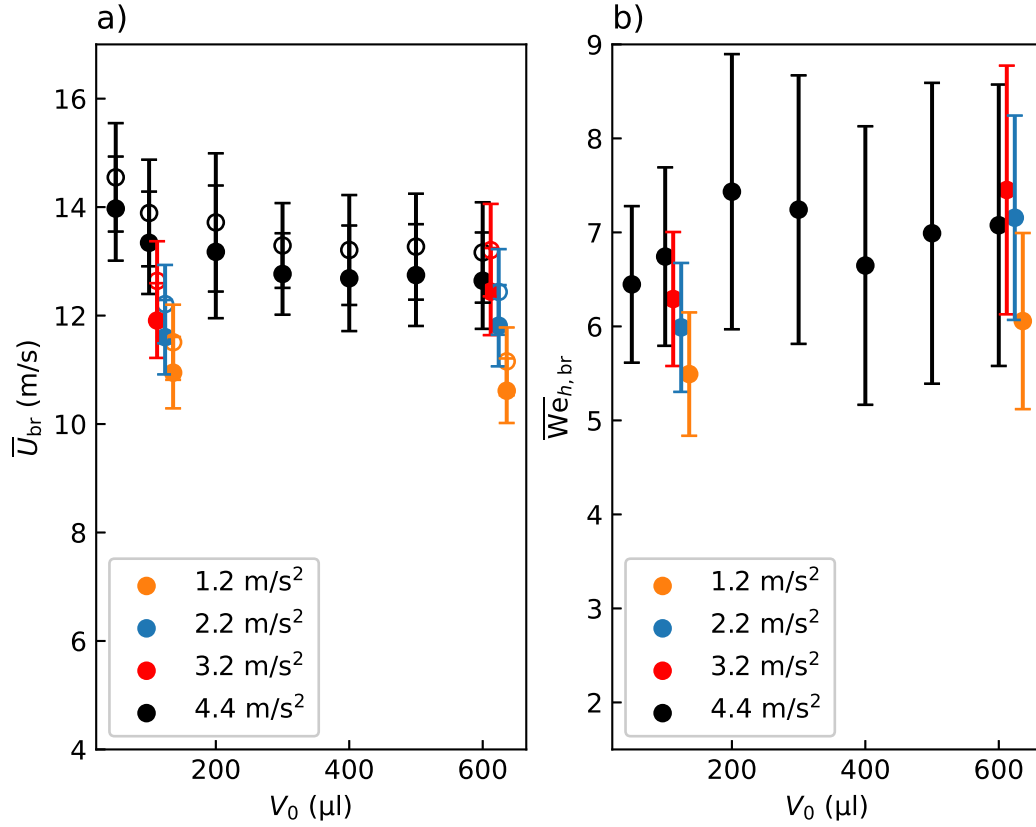**Figure 4.12:** a) Jet exit velocity, local velocity and b) Weber number for droplet breakup for the range of droplet volumes and flow accelerations tested. Different flow accelerations are shown with a slight volume offset for clarity for 100 µl and 600 µl droplets. Filled markers in a) represent $U_h$ while empty markers represent $U_j$. Error bars represent the corresponding uncertainty bounds (68% confidence).

breakup process detailed in Section 4.1 shows a lot of similarities with the vibrational breakup mode. In the vibrational breakup mode, the droplet experiences oscillations which amplify, resulting in the appearance of a narrow "neck" before the droplet ultimately breaks up into two or three parts [64].
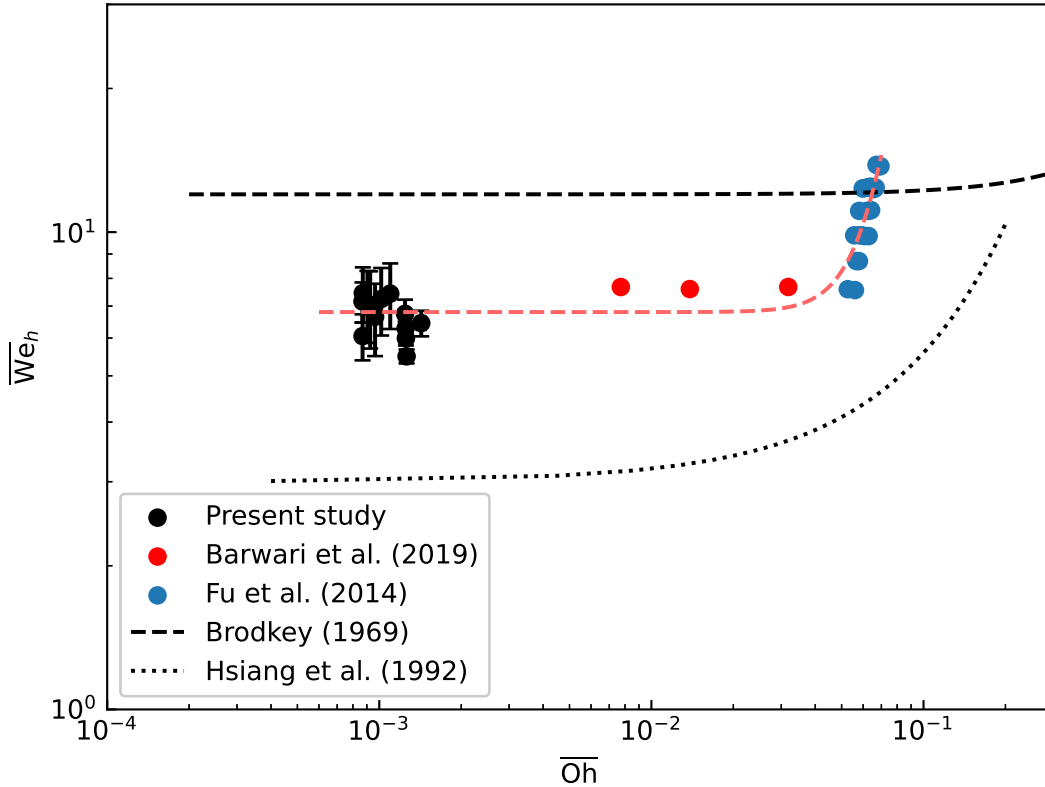
**Figure 4.13:** Critical Weber number for breakup of surface-mounted droplets. The dashed black line represents the critical Weber number for bag breakup in free-falling droplets [7]. The dotted black line represents the critical Weber number beyond which oscillatory deformation is expected [27]. The dashed red line represents a power-law fit applied to data pertaining to the breakup of surface-mounted droplets. Error bars represent the corresponding uncertainty bounds (68% confidence).

## 4.4 Child droplets

As seen in Figure 4.11, after the filament connecting the child and main droplet snaps, and breakup occurs, the child droplets contract to new metastable states due to the action of surface tension. The metastable state was estimated to have been reached when the percentage change of the child droplet's length fell below 2% between successive frames. At this point, child droplet geometric parameters were sampled for 40 milliseconds (five consecutive frames) to characterize the child droplet. In all cases tested, the length of the largest child droplet was its longest dimension. This is most likely due to the geometry of the droplet during the necking process. Additionally, for each configuration, the distribution of the child droplet lengths of the considered runs was not normally distributed. As such,

Figure 4.14 shows the median length of the largest child droplet that resulted from the breakup of the droplets tested in Table 3.2. The median is normalized by the sessile length of the originating droplet. For the range of volumes tested, larger sessile droplets break up into droplets with larger relative lengths ($\tilde{l}_{\mathrm{child}/l_0}$) irrespective of the flow acceleration. This increasing tend is seen to plateau for the largest volumes ($500\,\text{µl} \lesssim V_0 \lesssim 600\,\text{µl}$). For the same sessile volume, lower flow accelerations result in child droplets with smaller relative lengths.

Figure 4.15 shows the measured child droplet lengths (Figure 4.14) versus the lengths of the corresponding main droplet prior to breakup (see Figure C.2 (c)). The length of the main droplet is averaged over 40 ms prior to breakup. Both lengths are normalized by the sessile length of the main droplet. It is seen that the length of the child droplet follows a linear relationship ($\tilde{l}_{\mathrm{child}} \sim 0.25\bar{l}_{\mathrm{br}}$) with the length of the main droplet immediately prior to breakup. Specifically, the child droplet's length is about 25% of the length of the
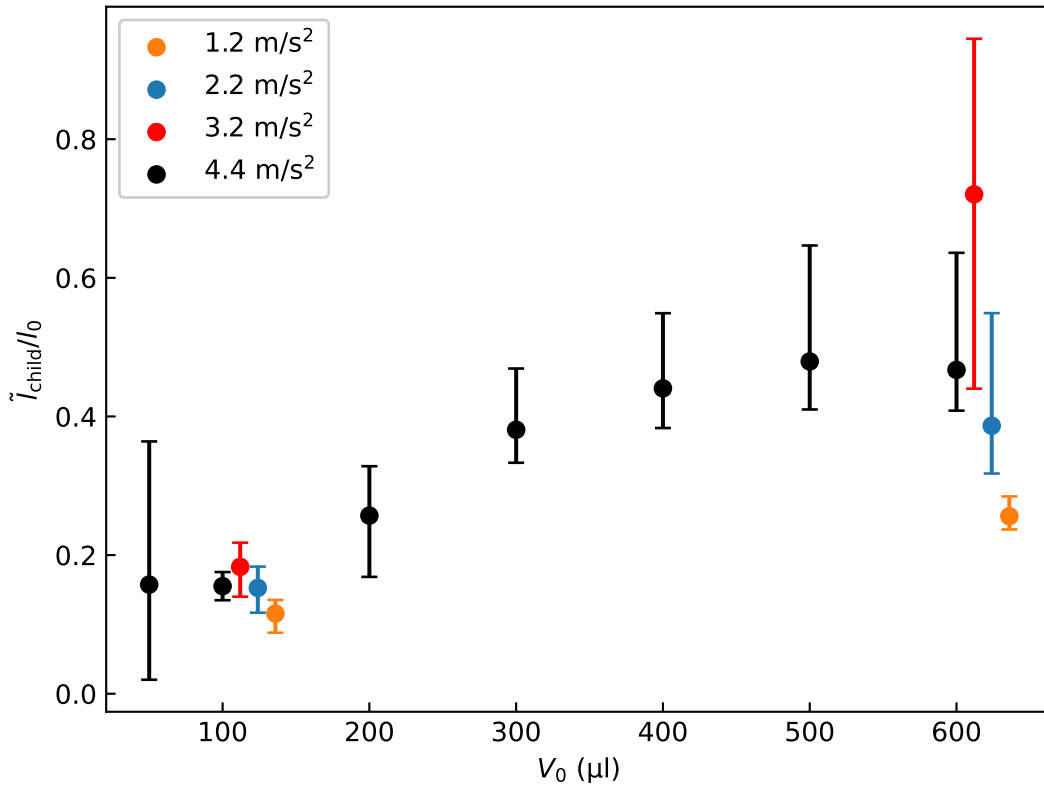


**Figure 4.14:** Length of child droplet shortly after breakup for the range of droplet volumes and flow accelerations tested. Note that different flow accelerations are shown with a slight volume offset for clarity for 100 µl and 600 µl droplets. Error bars represent the corresponding uncertainty bounds (68% confidence).

44

main droplet at breakup for the investigated cases. This implies that the necking position immediately prior to breakup is most likely invariant with the parameters tested. The necking position refers to the stream-wise position of the minimum width during necking, normalized by the length of the droplet at breakup.

Using the method detailed in Section 3.4, the volume of the largest child droplet formed after breakup was estimated using a 3D reconstruction rendered based on side and top-view droplet projections extracted from the corresponding images. It was determined that the child droplet volume distributions of the runs considered in each configuration were not normally distributed. Consequently, the median of the child droplet volumes are plotted in Figure 4.16 for each configuration. The results are normalized by the sessile volume of the originating droplet. The child droplets of the 50 µl and 100 µl droplets were too small to be reliably detected by the top-view cameras and, as such, child droplet volume measurements for these cases are not included in Figure 4.16. The results presented in Figure 4.16 show that larger originating droplets shed larger percentages of their volumes
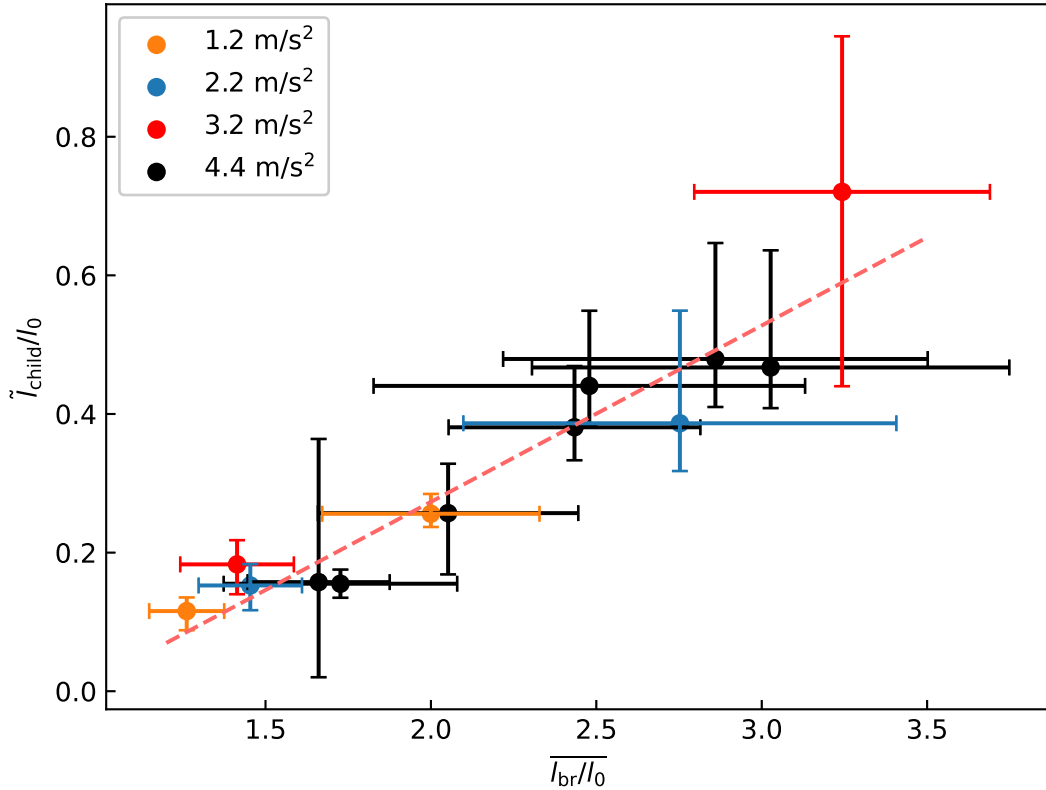


**Figure 4.15:** Length of child droplet versus length of main droplet immediately prior to breakup. Note that both lengths are normalized by the length of the sessile droplet. Error bars represent the corresponding uncertainty bounds (68% confidence).

during the breakup process. The volume of the child droplet also significantly reduced for lower flow accelerations, implying that a larger fraction of the sessile droplet was removed for the 600 µl originating droplet. Considering the fact that the length of the child droplet is its longest dimension, this trend shows a correlation with the trend in Figure 4.15. Larger sessile volumes and higher flow accelerations cause droplets to experience greater relative elongation prior to breakup (Figure C.2 (c)). This is most likely related to the increased loading from the larger frontal area of larger sessile volumes and the higher $U_{br}$ of droplets exposed to higher flow accelerations (Figure 4.12 (a)). Therefore, it is implied that smaller sessile droplets and droplets exposed to lower flow accelerations broke up into smaller volume fractions due to the lower elongation they experienced, as this results in smaller relative child lengths. It is also seen that the child droplets of the 500 µl originating droplets show a slight deviation from the aforementioned increasing trend. This is correlated to the smaller average measured height of the child droplets of the 500 µl droplets compared to that of the 400 µl originating droplets (see Figure C.4). Except for this deviation, the
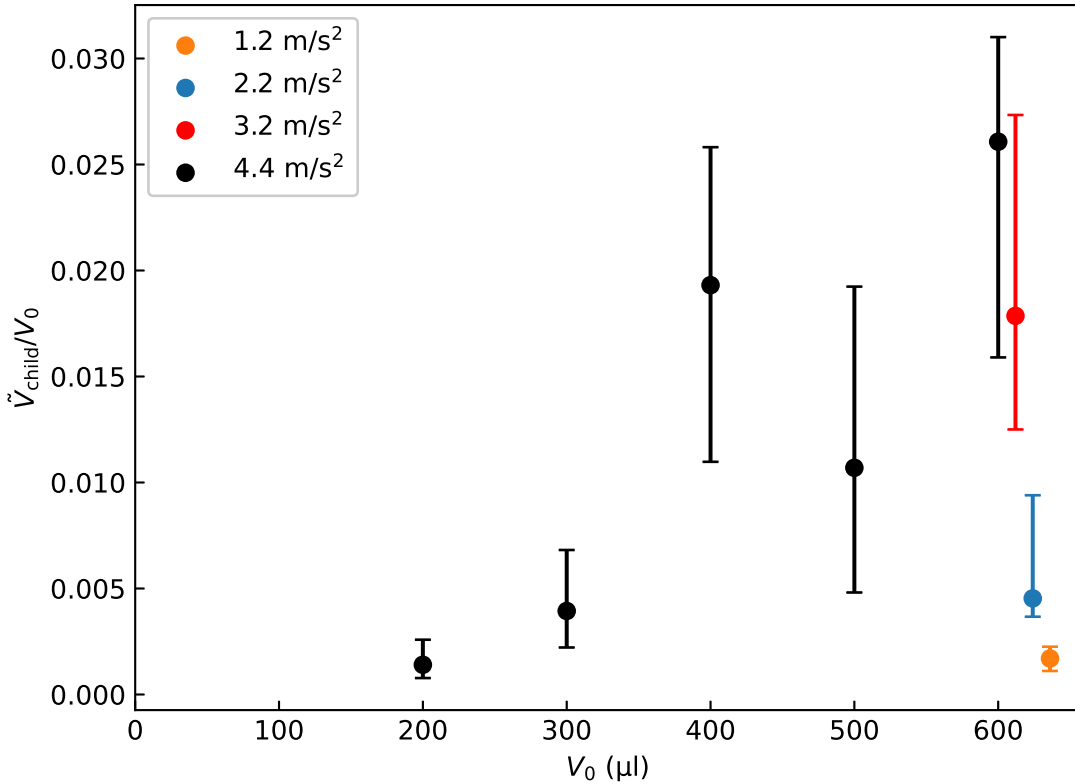


**Figure 4.16:** Median volume of child droplet normalized by the originating droplet volume and flow accelerations for initial volumes ranging from 200 to 600 µl. Child droplet volume estimation for originating volumes of 50 and 100 µl were unreliable and are thus not included. Error bars represent the inter-trial variation.

average child droplet height followed a very similar trend to that seen in Figure 4.14. The decreasing trend of the 500 µl originating droplets' child droplets' average height was seen to be within uncertainty.

The critical depinning velocity of the child droplets in Figure 4.16 were also estimated from their volumes using an exponential least-square fit ($\overline{U}_{j,\text{crit}} \propto e^{-0.0215V_0}$) applied to the measured $\overline{U}_{j,\text{crit}}$ in Figure 4.4. The estimated critical depinning velocity of the child droplets is normalized by $\overline{U}_{j,\text{br}}$ of the corresponding originating droplet and plotted in Figure 4.17. It is seen that due to their relatively small size, most child droplets, except those resulting from the largest droplet (600 µl) considered, have a critical depinning velocity that is higher than the flow velocity at which they are formed. As such, they are expected to remain pinned to the substrate after breakup unless a higher flow velocity is applied. This is also seen to be the case for the 600 µl droplet at lower flow accelerations ($1.2 \lesssim \frac{dU_j}{dt} \lesssim 3.2 \text{ m/s}^2$) which result in smaller child droplets.
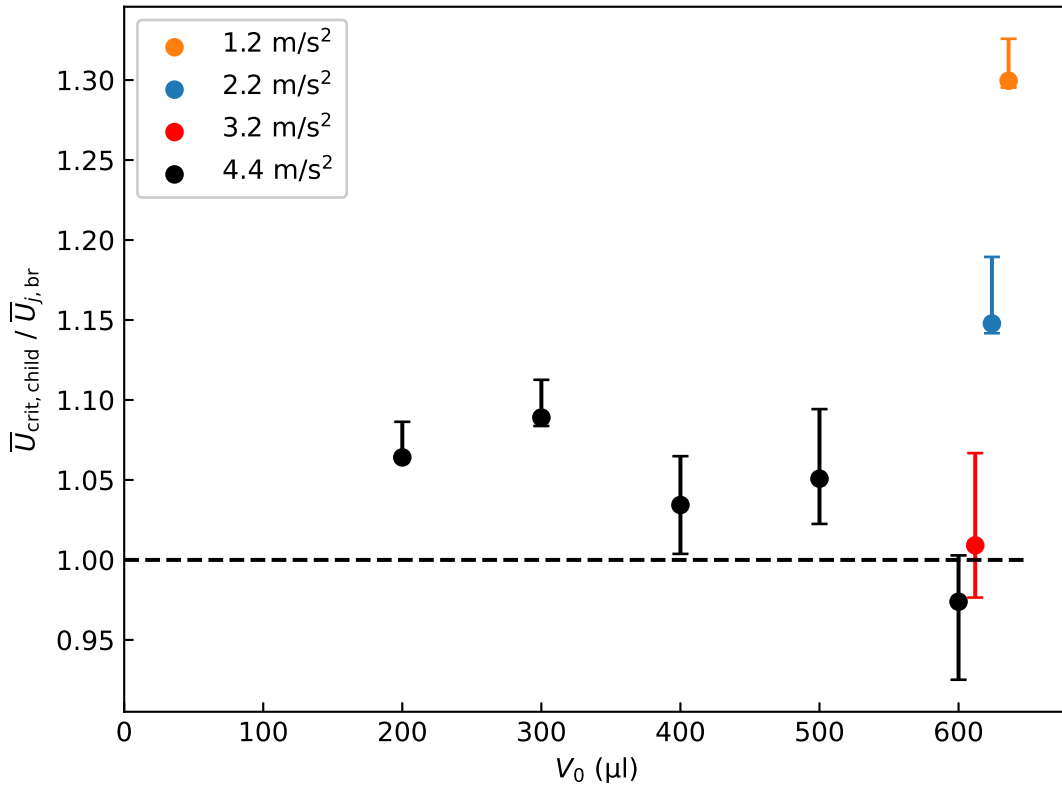


**Figure 4.17:** Approximate critical depinning velocity of child droplets for initial volumes ranging from 200 to 600 µl. Note that child droplet volume estimation for originating volumes of 50 and 100 µl were unreliable and are thus not included. Error bars represent the corresponding uncertainty bounds (68% confidence).

## 4.5 Practical implications of findings

The critical flow velocities presented in this chapter are summarized in Figure 4.18 for $\frac{dU_j}{dt} = 4.4$ m/s². They were each seen to follow exponential relationships ($\overline{U}_{j,\text{crit}} \propto e^{-0.02x}$, $\overline{U}_{j,\text{neck}} \propto e^{-0.05x}$, and $\overline{U}_{j,\text{br}} \propto e^{-0.01x}$) with the sessile volume, as indicated by the dashed lines. Droplets near the gravity flattened regime ($V_0 \gtrsim 100$ µl) were seen to depin at a relatively constant flow velocity ($U_j \approx 8$ m/s) while the smaller droplets ($10 \lesssim V_0 \lesssim 100$ µl) depinned at progressively higher flow velocities as volume decreased ($8 \lesssim V_0 \lesssim 13$ m/s). At slightly higher flow velocities ($U_j \approx 13$ m/s for the 50 µl droplet and $U_j \approx 10.7$ m/s for $V_0 \gtrsim 100$ µl droplets), the onset of necking was seen which serves as an indicator of the start of the breakup process. The breakup process ended with the separation of the child droplet occuring at $U_j \approx 14.5$ m/s for the 50 µl droplet and $U_j \approx 13.4$ m/s for droplets in the range $V_0 \gtrsim 100$ µl. The resulting child droplets for the 600 µl droplets at $\frac{dU_j}{dt} = 4.4$ m/s² were observed to move immediately after breakup due to their critical depinning velocity being of similar magnitude to the flow velocity at which breakup occurs. The child droplets
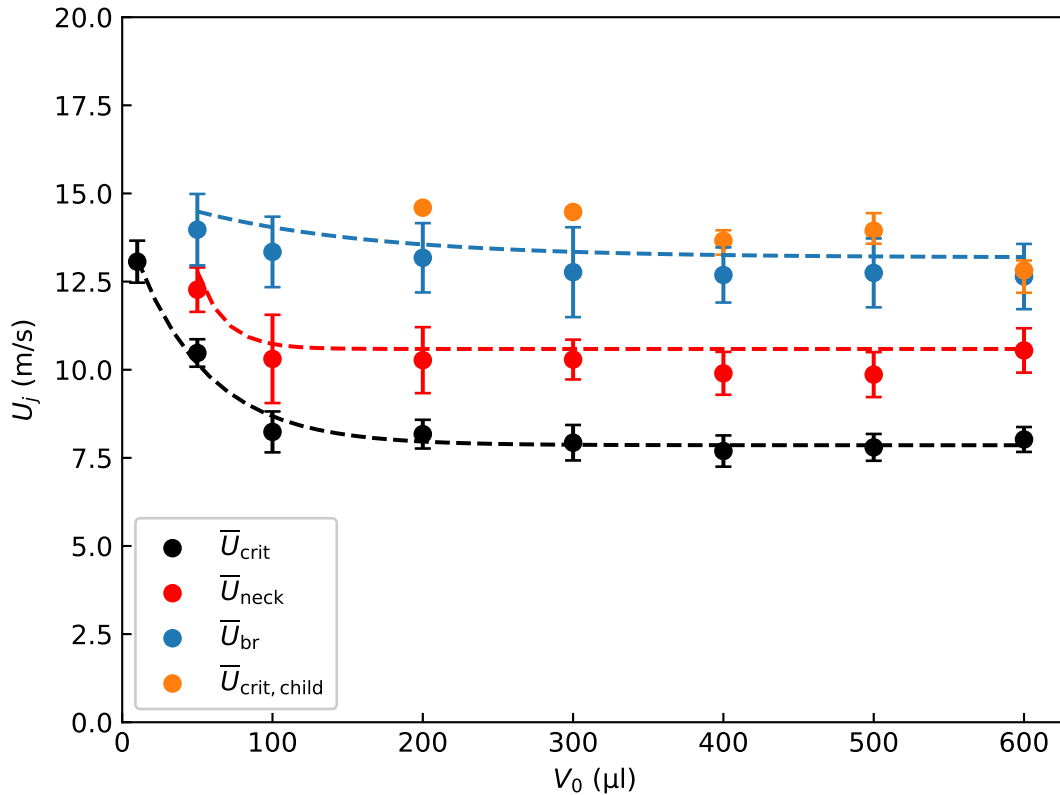


**Figure 4.18:** Summary of critical flow velocities in the present study. Note that the dashed lines represent exponential least-square fits applied to the corresponding plots.

of the smaller originating volumes ($100 \lesssim V_0 \lesssim 500$ µl), however, were predicted to depin at higher flow velocities than the flow velocity at which the originating droplets broke up.

In order to facilitate the discussion of the findings of the present study from a more practical perspective, six distributions of droplet volumes of ranges [1, 100], [1, 200], [1, 300], [1, 400], [1, 500], and [1, 600] µl were simulated. The aim is to use each volume distribution to illustrate potential removal behaviour for different target velocities in a drying application based on the findings of the present study. Each distribution was assumed to be Gaussian
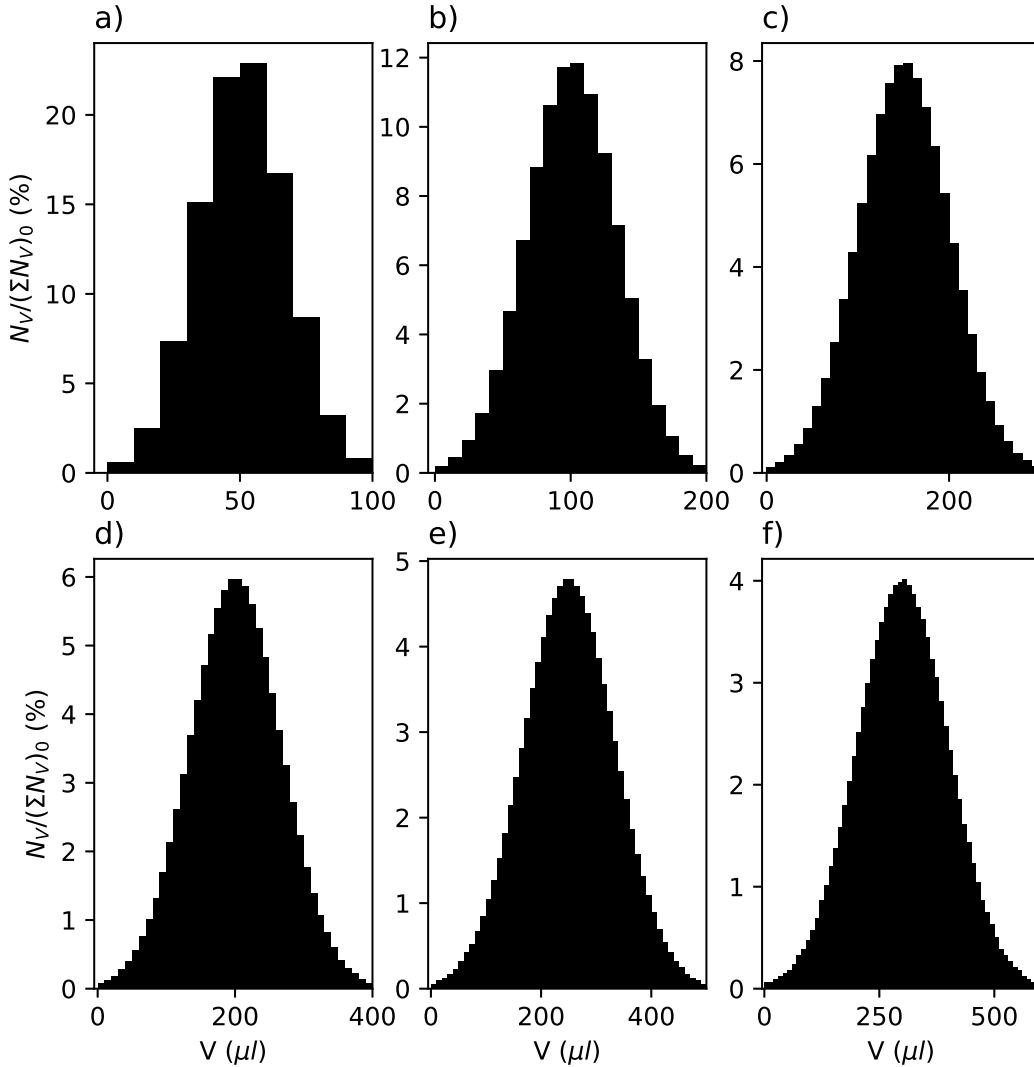


**Figure 4.19:** Initial Gaussian relative frequency distribution of droplet volumes of ranges a) [1, 100], b) [1, 200], c) [1, 300], d) [1, 400], e) [1, 500], and f) [1, 600] µl

and to have an initial cumulative volume of one litre. The histograms in Figure 4.19 show the corresponding initial distributions for each volume range, where the ordinate axis represents the frequency of each volume interval as a percentage of the initial total number of droplets in the distribution.

Figures 4.20 and 4.21 show the predicted evolution of the initial volume distributions seen in Figure 4.19 for the [1, 100] and [1, 600] µl volume ranges, respectively, for various target velocities. The predictions are based on the findings of the present study for $\frac{dU_j}{dt}$ = 4.4 m/s$^2$, and extrapolations with the least-square fits in Figure 4.18. It is assumed that the individual droplets are placed on the anodized aluminium substrate used in the present study and spaced sufficiently far apart that they do not interact with each other through their removal process. Each individual subplot in Figures 4.20 and 4.21 represents the outcome of a different target velocity, and it is assumed that the flow ramps up from zero to the corresponding target velocity with $\frac{dU_j}{dt}$ = 4.4 m/s$^2$. As such, the predictions for each target velocity are independent of prior predictions for lower target velocities. The
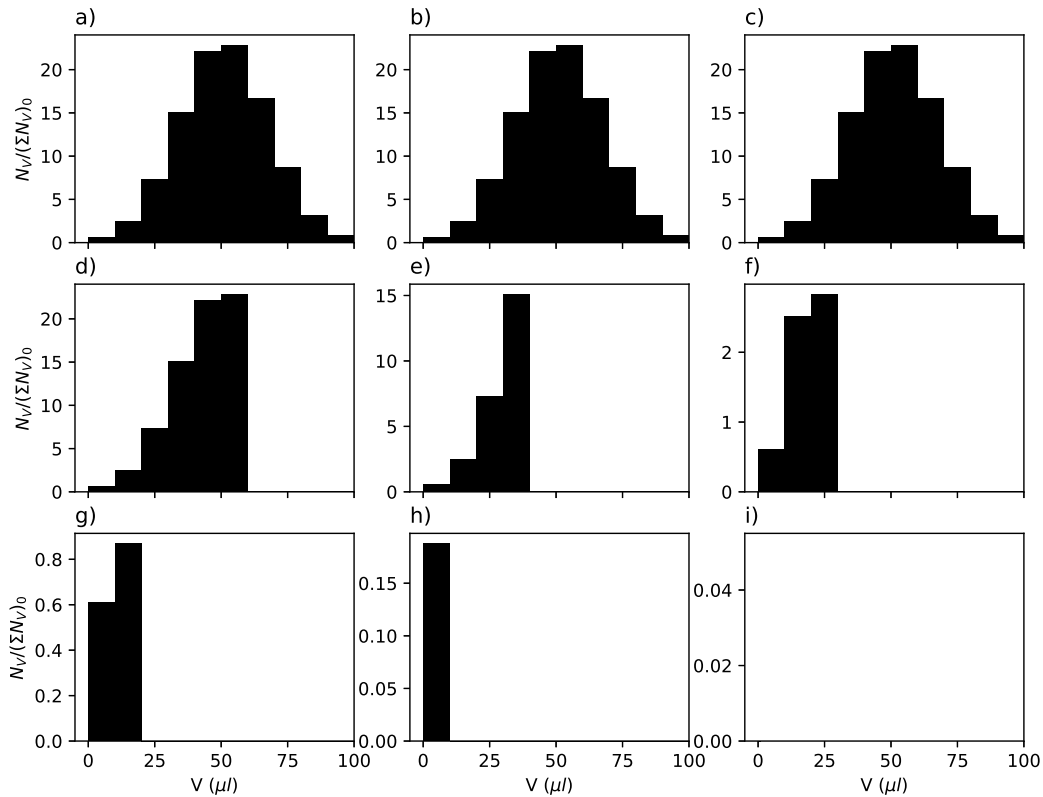


**Figure 4.20:** Predicted frequency distribution after exposing droplets ranging in $1 \leq V \leq$ 100 µl to various target velocities. The considered target velocities are $U_{j,\text{targ}}$ = a) 0, b) 8, c) 9, d) 10, e) 11, f) 12, g) 13, h) 14, and i) 15 m/s.
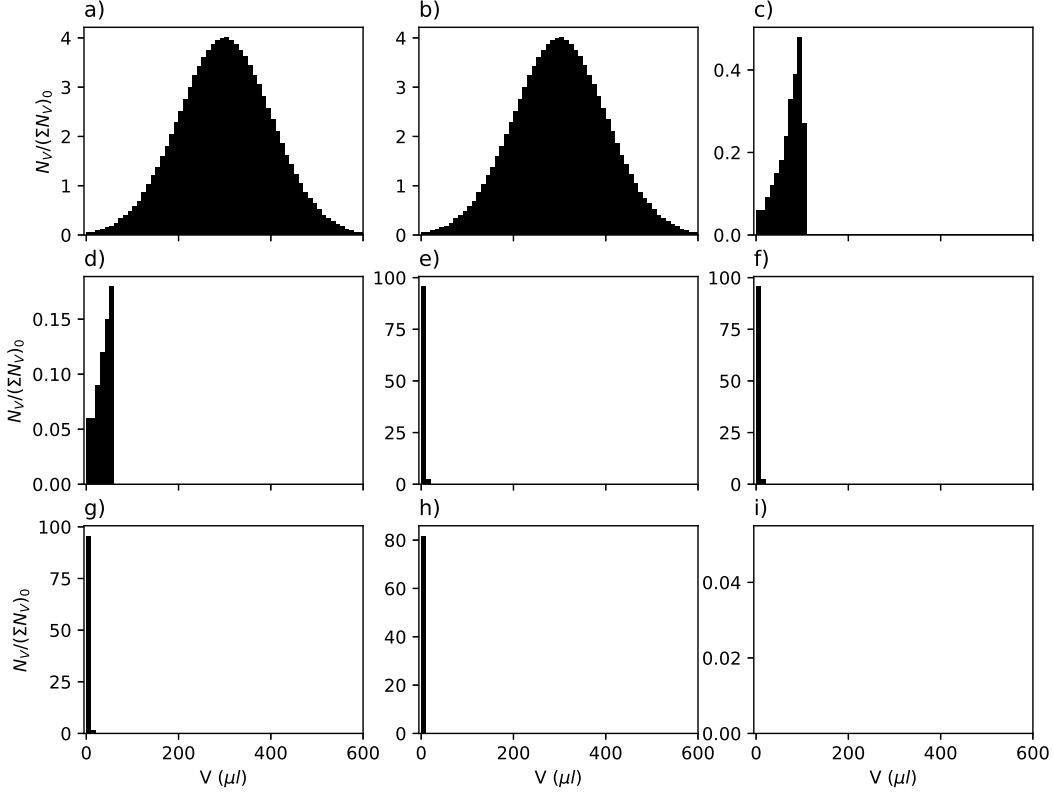
**Figure 4.21:** Predicted frequency distribution after exposing droplets ranging in $1 \leq V \leq$ 600 µl to various target velocities. The considered target velocities are $U_{j,\text{targ}} =$ a) 0, b) 8, c) 9, d) 10, e) 11, f) 12, g) 13, h) 14, and i) 15 m/s.

results are aimed at providing insight into how various volume distributions are affected by a designer's choice of target velocity. The subplots in Figures 4.20 and 4.21 correspond to target velocities, $U_{j,\text{targ}}$, ranging from 0 to 15 m/s. The ordinate axis in both figures represents the frequency of a given volume interval normalized by the initial total number of droplets in the distribution.

It is seen in Figure 4.20 that for droplet volumes in the range $1 \leq V \leq 100$ µl, the distribution remains unchanged for $U_{j,\text{targ}} < 11$m/s. For a higher target velocity, the larger droplets would be depinned and removed. Droplets in this volume range are expected to not breakup, or to breakup into sub-microliter volumes, which can be neglected due to their small wetted area and high likelihood of being evaporated. As such, removal of droplets in this volume range is primarily governed by their critical depinning velocity. Consequently, for progressively higher target velocities, only the smallest droplets are expected to remain. Based on the least-square fit in Figure 4.18, for a target velocity $U_{j,\text{targ}} \approx 15$ m/s, all microliter sized droplets are expected to be removed ($\overline{U}_{j,\text{crit}} \approx 14.5$ m/s for $V_0 = 1$ µl). The predicted evolution of the volume distribution for droplet volumes in

the range $1 \leq V \leq 600$ µl (Figure 4.21) is slightly different due to the breakup of the larger droplets. The distribution is seen to begin to change at a lower $U_{j,\mathrm{targ}} \approx 9$ m/s. At this target velocity, the larger droplets ($V_0 > 100$ µl) are expected to depin but potentially not breakup since the flow velocity at the onset of necking has not been reached. With a target velocity of 11 m/s, the larger droplets are expected to break up into smaller microliter droplets, which results in the distribution being skewed to the left. For progressively higher target velocities, the critical depinning velocity of the larger child droplets would be reached and only the smallest initial volumes and child droplets remain. Ultimately, once again, at a target velocity $U_{j,\mathrm{targ}} \approx 15$ m/s, all microliter sized droplets and child droplets are expected to be removed.

Figure 4.22 shows the corresponding remnant volume fraction, defined as the cumulative volume remaining after the target velocity is reached as a percentage of the initial cumulative volume for the aforementioned configurations. The removal ratio is not expected to change for target velocities below $8 \lesssim U_{j,\mathrm{targ}} \lesssim 11$ m/s at which point the larger droplets in the distributions are depinned. Higher target velocities are expected to result in a greater
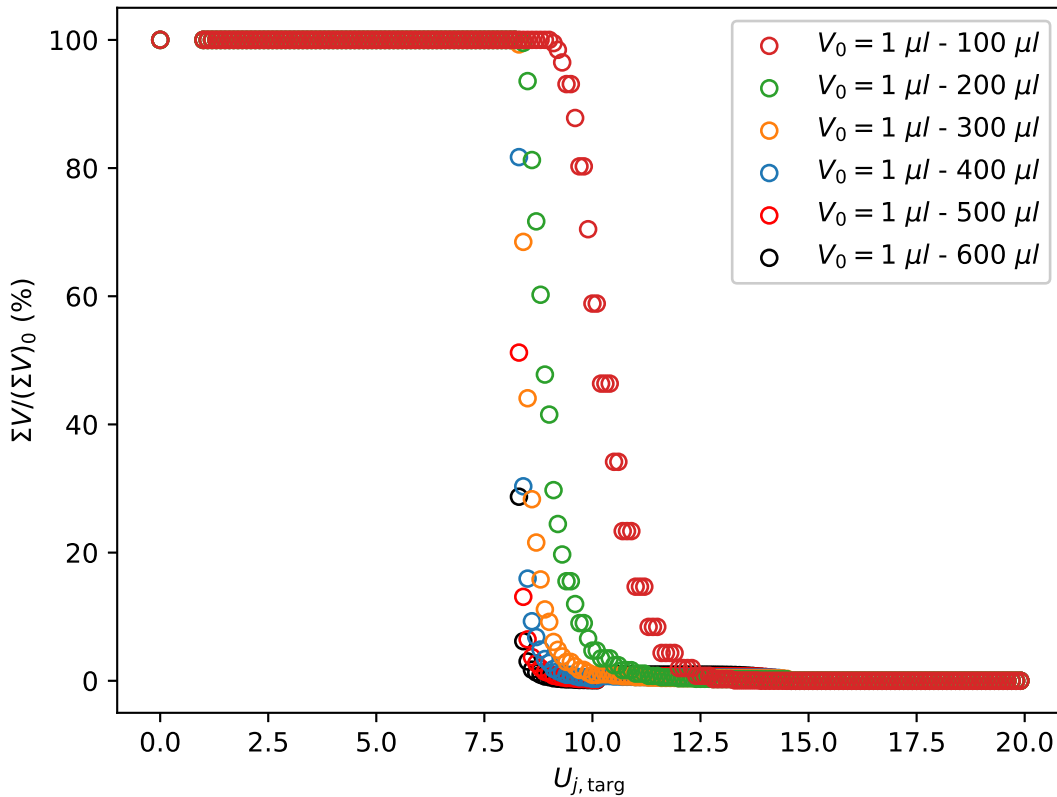


**Figure 4.22:** Predicted volume fraction remaining after exposing droplets of various volume ranges to various target velocities.

volume fraction being removed since smaller droplet volumes will depin. Ultimately, the remnant volume fraction approaches zero at $U_{j,\mathrm{targ}} \approx 15$ m/s since all the microliter sized droplets are removed. It is seen that for the same target velocity, initial distributions with higher volume bounds have a greater percentage of their initial volume removed. This is because majority of the larger droplets ($V_0 \gtrsim 100$ µl) are removed at roughly the same low flow velocity, and they account for a large percentage of the initial volume fraction. Additionally, although breakup may occur for a given droplet, the resulting child droplet that remains makes up a smaller fraction of the droplet than what is removed. Consequently, there is a net reduction in the remnant volume fraction. Figure 4.23 shows the predicted volume of the largest droplet remaining for a given target velocity. It is seen that this is primarily governed by the critical depinning velocity of the droplets.
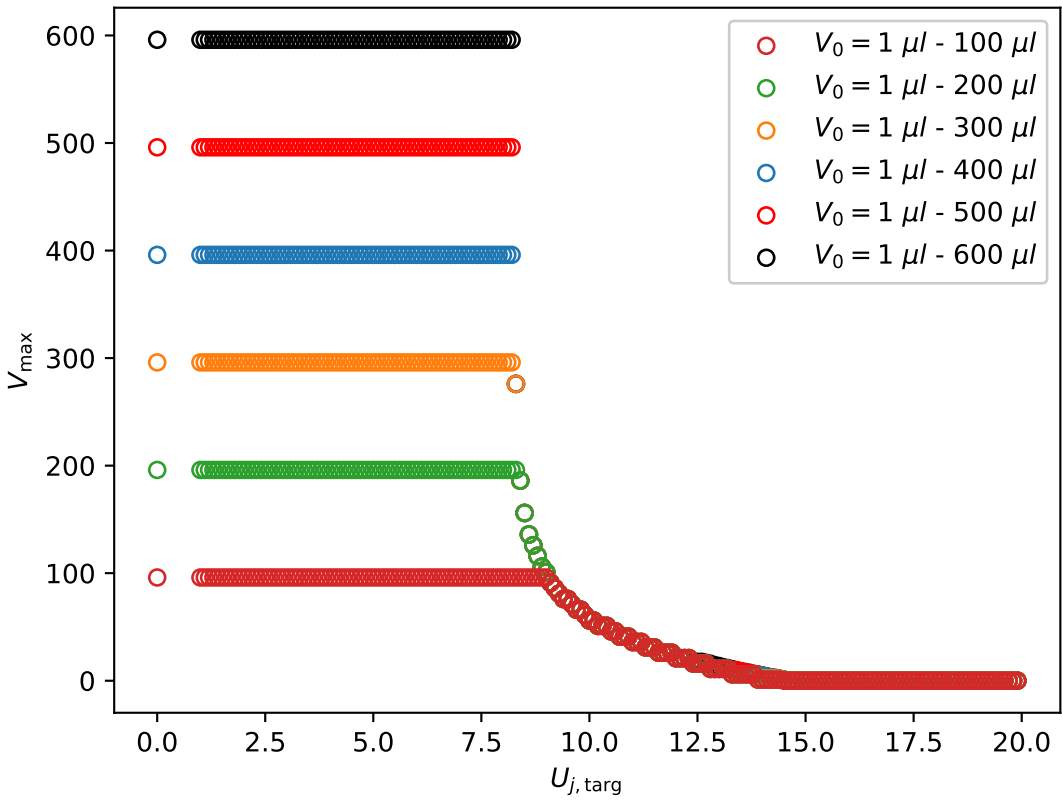


**Figure 4.23:** Predicted volume of largest droplet remaining after exposing droplets of various volume ranges to various target velocities.

# Chapter 5

# Conclusions and Future Work

This thesis studied the response of an isolated surface-mounted droplet to an accelerating impinging jet flow, focusing primarily on droplet breakup. The specific objectives of this study were to: (i) characterize the flow conditions that lead to breakup; (ii) understand the characteristics of the droplet immediately prior to breakup that serve as an indicator of the impending breakup; and (iii) characterize the geometry of the child droplet that results from the breakup of the original droplet.

Impinging jet flows were generated using a custom jet facility in the Fluid Mechanics Research Laboratory at the University of Waterloo [70]. An anodized aluminium substrate served as the impinging target. Distilled water droplets were tested on the substrate with a maximum jet exit target velocity $U_j = 20$ m/s at various flow accelerations ($\frac{dU_j}{dt} = 1.2$, 2.2, 3.2, and 4.4 m/s$^2$). The background flow fields were characterized using hotwire anemometer measurements at various locations for the considered flow accelerations (Section 2.1). Two sets of experiments were conducted to characterize the depinning and breakup of the droplets in this study. For all experiments, top and side view images of the droplet were captured simultaneously. In these experiments, droplet volumes of 10, 50, 100, 200, 300, 400, 500, and 600 µl were studied at a flow acceleration $\frac{dU_j}{dt} = 4.4$ m/s$^2$. Similar tests were performed to capture the droplet breakup behaviour. In these tests, droplet volumes of 50, 100, 200, 300, 400, 500, and 600 µl were studied at varying flow accelerations (Table 3.2).

## 5.1 Conclusions

The results show that the breakup process of surface-mounted droplets in an accelerating impinging jet flow comprises three distinctive but continuous stages: depinning, necking, and breakup, which have been analyzed in Chapter 4. In the present study, droplets in the range $V_0 \lesssim 100$ µl depin at progressively lower critical velocities (8 m/s $\lesssim \overline{U}_{h,\text{crit}} \lesssim 13$ m/s) for larger sessile volumes. This is attributed to smaller droplets having a higher shear flow submergence and lower frontal area. These characteristics result in smaller droplets experiencing a lower effective flow velocity and loading. Beyond this volume range ($V_0 \gtrsim 100$ µl), $\overline{U}_{\text{crit}}$ remains constant ($\overline{U}_{h,\text{crit}} \approx 8$ m/s) for the tested sessile volumes. The droplet volumes for which $\overline{U}_{\text{crit}}$ is constant fall in the gravity flattened regime, where the sessile droplet height also plateaus ($\overline{h}_0 \approx 3$ mm). The droplets in the present study depin within the Weber number range of $3 \lesssim \overline{\text{We}}_{h,\text{crit}} \lesssim 4$ when exposed to impinging jet flow.

Shortly after depinning, necking occurs as a precursor to droplet breakup. For the investigated droplets, this onset of necking occurs at flow velocities in the range $1.25 \lesssim U_h/\overline{U}_{h,\text{crit}} \lesssim 1.4$. For droplets in the range $V_0 \lesssim 100$ µl, $\overline{U}_{\text{neck}}$ decreases with increasing sessile volume. For larger droplets ($V_0 \gtrsim 100$ µl), however, $\overline{U}_{\text{neck}}$ remains constant ($\overline{U}_{\text{neck}} \approx 10.3$ m/s). Within the range of investigated flow accelerations, $\overline{U}_{\text{neck}}$ is invariant with flow acceleration. Furthermore, $\overline{\text{We}}_{h,\text{neck}}$ is nearly constant ($\overline{\text{We}}_{h,\text{neck}} \approx 5.5$) for the highest flow acceleration considered.

Ultimately, the necking process culminates in two, or more, smaller child droplets breaking off from the main droplet. The breakup occurs at around $1.4\overline{U}_{h,\text{crit}}$ for the 50 µl droplets and $1.6 \lesssim U_h/\overline{U}_{h,\text{crit}} \lesssim 1.7$ for $V_0 \gtrsim 100$ µl. Similar to $U_{\text{neck}}$, larger droplets in the range $V_0 \lesssim 200$ µl breakup at progressively lower flow velocities while droplets in the range $V_0 \gtrsim 200$ µl breakup up at very similar flow velocities ($\overline{U}_{h,\text{br}} \approx 12.8$ m/s). Droplets exposed to a lower flow acceleration breakup at slightly lower flow velocities. The Weber number at which breakup occurs for the highest flow acceleration tested ($\frac{dU_j}{dt} = 4.4$ m/s$^2$) falls between $6.5 \lesssim \overline{\text{We}}_{h,\text{br}} \lesssim 7.5$ for all considered sessile volumes. Droplets for which breakup was investigated fell into the Ohnesoge number range $8.8 \times 10^{-4} \leq \overline{\text{Oh}} \leq 1.4 \times 10^{-3}$. When complemented by data obtained from other studies [18][4], it was seen that $\overline{\text{We}}_{h,\text{br}}$ follows a power law relationship with Oh ($\overline{\text{We}}_{h,\text{br}} \sim \overline{\text{Oh}}^{4.9}$). Additionally, for $\overline{\text{Oh}} \lesssim 5.3 \times 10^{-2}$, $\overline{\text{We}}_{h,\text{br}}$ is relatively invariant with Oh ($\overline{\text{We}}_{h,\text{br}} \approx 7.0$). Beyond this range, $\overline{\text{We}}_{h,\text{br}}$ increases with Oh. This is consistent with findings in studies of the breakup of free-falling droplets which show that the viscous forces inside the droplet hinder its deformation. It was also seen that surface-mounted droplets breakup in the vibrational breakup Weber number regime seen in free-falling droplets [46].

The volume of the largest child droplet resulting from the breakup was estimated using a 3D reconstruction based on side and top-view droplet projections. Larger originating droplets shed larger percentages of their volumes during the breakup process. The volume of the child droplet also significantly reduces for lower flow accelerations. These trends were linked to the correlation (Figure 4.15) which shows that the length of the child droplet is linearly related ($\tilde{l}_{\text{child}} \sim 0.25\overline{l}_{\text{br}}$) to the length of the original droplet immediately prior to

breakup. Specifically, this implies that smaller sessile droplets and droplets exposed to lower flow accelerations likely breakup into smaller volume fractions due to the lower elongation they experience. The smaller sessile volumes experience a lower relative elongation prior to breakup, likely due to their smaller frontal area. Similarly, droplets exposed to a lower flow acceleration experience a lower elongation likely due to their lower $U_{\mathrm{br}}$. Additionally, due to the small sizes of these child droplets, most child droplets do not depin after breaking off.

## 5.2   Future work

From the results of the present work, additional questions remain to be addressed through further analysis and investigations. The following recommendations are made for future work.

1. Investigate the relationship between droplet oscillations and breakup. As discussed in Section 4.3, the breakup of surface-mounted droplets occurs in the vibrational breakup Weber number regime of free-falling droplets. In free-falling droplets, this breakup mode occurs due to the progressive increase in the droplet's oscillation amplitude, which eventually results in droplet breakup. Droplet videos captured in the present study showed strong bulk oscillations during the breakup process. Studying these oscillations could potentially explain the influence of instantaneous events on the breakup process of surface-mounted droplets.

2. Investigate the effects of substrate wettability on the breakup process. In the present study, a single combination of liquid (water), gas (air), and solid (anodized aluminium) was considered. However, as discussed in Section 2.3.4, the substrate wettability plays a significant roles in the breakup process. The present study attempted to account for this by comparing measurements from studies with surface-mounted droplets with higher Oh. However, future experiments can be performed to validate whether droplets in impinging jets on substrates of varied wettabilities will follow the same trend seen in Chapter 4.

3. Investigate the effects of surfactant concentration on the breakup process. In many non-touch cleaning applications, the droplets being removed have been mixed with industrial surfactants, such as detergents. These are known to affect the droplet's properties, especially the surface tension. As discussed in Section 2.3.4, the droplet's surface tension is a primary source of resistance in the breakup process. Future experiments can be performed to illustrate how the presence of these surfactants would affect the breakup process of surface-mounted droplets.

4. Investigate the breakup behaviour of droplets in an array. The present study focused primarily on the breakup behaviour of a single isolated droplet. Furthermore, the practical implications discussed in Section 4.5 assumed that the droplets in the considered distributions were sufficiently far apart that they did not interact with each other. However, in many practical applications, this is not the case. The change

in the flow development over the droplets due to the proximity to other droplets might affect the breakup behaviour of the droplets. Consequently, future experiments could be performed to shed light on the extent to which the breakup behaviour in these applications deviate from the predictions made in Section 4.5. This can be performed using multiple droplets of different distributions which are randomly spaced on a substrate.

# References

[1] ADIGA, K., WILLAUER, H. D., ANANTH, R., & WILLIAMS, F. W. 2009 Implications of droplet breakup and formation of ultra fine mist in blast mitigation. *Fire Safety Journal* **44** (3), 363–369. ↩

[2] ANTONINI, C., INNOCENTI, M., HORN, T., MARENGO, M., & AMIRFAZLI, A. 2011 Understanding the effect of superhydrophobic coatings on energy reduction in anti-icing systems. *Cold regions science and technology* **67** (1-2), 58–67. ↩

[3] ARKLES, B. 2011 Hydrophobicity, hydrophilicity and silane surface modification. *Gelest Inc, Morrisville* ↩

[4] BARWARI, B., BURGMANN, S., BECHTOLD, A., ROHDE, M., & JANOSKE, U. 2019 Experimental study of the onset of downstream motion of adhering droplets in turbulent shear flows. *Experimental Thermal and Fluid Science* **109**, 109843. ↩

[5] BEREJNOV, V. & THORNE, R. E. 2007 Effect of transient pinning on stability of drops sitting on an inclined plane. *Physical Review E* **75** (6), 066308. ↩

[6] BORMASHENKO, E., MUSIN, A., POGREB, R., LUZ, E., & ZINIGRAD, M. 2010 Thickness of gravity-flattened water layers ("puddles") deposited on the polymer substrates and the hysteresis of the contact angle. *Colloids and Surfaces A: Physicochemical and Engineering Aspects* **372** (1-3), 135–138. ↩

[7] BRODKEY, R. 1967 The phenomena of fluid motions, addison-wesley. *Reading* **621**. ↩

[8] CAO, Y., TAN, W., & WU, Z. 2018 Aircraft icing: an ongoing threat to aviation safety. *Aerospace science and technology* **75**, 353–385. ↩

[9] CAO, Y., WU, Z., SU, Y., & XU, Z. 2015 Aircraft flight characteristics in icing conditions. *Progress in Aerospace Sciences* **74**, 62–80. ↩

[10] CAO, Y. & TAMURA, T. 2020 Large-eddy simulation study of reynolds number effects on the flow around a wall-mounted hemisphere in a boundary layer. *Physics of Fluids* **32** (2), 025109. ↩

[11] CASPER, J. M. 1976 Physical chemistry of surfaces , arthur w. adamson. ↩

[12] CHINI, S. F. & AMIRFAZLI, A. 2011 A method for measuring contact angle of asymmetric and symmetric drops. *Colloids and Surfaces A: Physicochemical and Engineering Aspects* **388** (1-3), 29–37. ↩

[13] DONG, H., CARR, W. W., & MORRIS, J. F. 2006 An experimental study of drop-on-demand drop formation. *Physics of fluids* **18** (7). ↩

[14] ESPOSITO, A., MONTELLO, A. D., GUEZENNEC, Y. G., & PIANESE, C. 2010 Experimental investigation of water droplet–air flow interaction in a non-reacting pem fuel cell channel. *Journal of Power Sources* **195** (9), 2691–2699. ↩

[15] EXTRAND, C. & MOON, S. I. 2010 When sessile drops are no longer small: transitions from spherical to fully flattened. *Langmuir* **26** (14), 11815–11822. ↩

[16] FAN, J., WILSON, M., & KAPUR, N. 2011 Displacement of liquid droplets on a surface by a shearing air flow. *Journal of colloid and interface science* **356** (1), 286–292. ↩

[17] FARHADI, S., FARZANEH, M., & KULINICH, S. 2011 Anti-icing performance of super-hydrophobic surfaces. *Applied Surface Science* **257** (14), 6264–6269. ↩

[18] FU, S. C., LEUNG, W. T., & CHAO, C. Y. 2014 Detachment of droplets in a fully developed turbulent channel flow. *Aerosol Science and Technology* **48** (9), 916–923. ↩

[19] FURBANK, R. J. & MORRIS, J. F. 2007 Pendant drop thread dynamics of particle-laden liquids. *International journal of multiphase flow* **33** (4), 448–468. ↩

[20] HADŽIABDIĆ, M. & HANJALIĆ, K. 2008 Vortical structures and heat transfer in a round impinging jet. *Journal of Fluid Mechanics* **596**, 221–260. ↩

[21] HANSON, A., DOMICH, E., & ADAMS, H. 1956 An experimental investigation of impact and shock wave breakup of liquid drops. *Univ. of Minnesota, Inst. of Tech. Dept. of Aero. Eng. Res. Report* **125**. ↩

[22] HANSON, A., DOMICH, E., & ADAMS, H. 1963 Shock tube investigation of the breakup of drops by air blasts. *The Physics of Fluids* **6** (8), 1070–1080. ↩

[23] HASSLER, G. 1970 Breakup of large water drops under the influence of aerodynamic forces in a steady stream of stream and stream at subsonic velocities. In *3rd International Conference on Rain Erosion and Related Phenomena, Hampshire, Angleterre.* ↩

[24] HINZE, J. 1949 Critical speeds and sizes of liquid globules. *Flow, Turbulence and Combustion* **1**, 273–288. ↩

[25] HINZE, J. O. 1955 Fundamentals of the hydrodynamic mechanism of splitting in dispersion processes. *AIChE journal* **1** (3), 289–295. ↩

[26] HOOSHANGINEJAD, A. & LEE, S. 2017 Droplet depinning in a wake. *Physical Review Fluids* **2** (3), 031601. ↩

[27] HSIANG, L.-P. & FAETH, G. M. 1992 Near-limit drop deformation and secondary breakup. *International journal of multiphase flow* **18** (5), 635–652. ↩

[28] ISRAELACHVILI, J. N. 2015 *Intermolecular and surface forces.* Academic press. ↩

[29] KRZECZKOWSKI, S. A. 1980 Measurement of liquid droplet disintegration mechanisms. *International Journal of Multiphase Flow* **6** (3), 227–239. ↩

[30] LEUNG, W. T., FU, S. C., & CHAO, C. Y. 2017 Detachment of droplets by air jet impingement. *Aerosol Science and Technology* **51** (4), 467–476. ↩

[31] LEUNG, W. T., FU, S. C., & CHAO, C. Y. 2017 Detachment of droplets by air jet impingement. *Aerosol Science and Technology* **51** (4), 467–476. ↩

[32]  LUO, X., YAN, H., HUANG, X., YANG, D., WANG, J., & HE, L. 2017 Breakup characteristics of aqueous droplet with surfactant in oil under direct current electric field. *Journal of colloid and interface science* **505**, 460–466. ↩

[33]  MAHER, F. J. 1965 Wind loads on basic dome shapes. *Journal of the Structural Division* **91** (3), 219–228. ↩

[34]  MANDAL, D. K., CRISCIONE, A., TROPEA, C., & AMIRFAZLI, A. 2015 Shedding of water drops from a surface under icing conditions. *Langmuir* **31** (34), 9340–9347. ↩

[35]  MILNE, A. & AMIRFAZLI, A. 2009 Drop shedding by shear flow for hydrophilic to superhydrophobic surfaces. *Langmuir* **25** (24), 14155–14164. ↩

[36]  MOFFAT, R. 1982 Contributions to the theory of single-sample uncertainty analysis ↩

[37]  MOFFAT, R. J. 1985 Using uncertainty analysis in the planning of an experiment ↩

[38]  MOFFAT, R. J. 1988 Describing the uncertainties in experimental results. *Experimental thermal and fluid science* **1** (1), 3–17. ↩

[39]  MOGHTADERNEJAD, S., JADIDI, M., ESMAIL, N., & DOLATABADI, A. 2016 Shear-driven droplet coalescence and rivulet formation. *Proceedings of the Institution of Mechanical Engineers, Part C: Journal of Mechanical Engineering Science* **230** (5), 793–803. ↩

[40]  NICHOLLS, J. A. & RANGER, A. 1969 Aerodynamic shattering of liquid drops. *Aiaa Journal* **7** (2), 285–290. ↩

[41]  OBENAUF, D. & SOJKA, P. 2021 Theoretical deformation modeling and drop size prediction in the multimode breakup regime. *Physics of Fluids* **33** (9), 092113. ↩

[42]  OTSU, N. 1979 A threshold selection method from gray-level histograms. *IEEE transactions on systems, man, and cybernetics* **9** (1), 62–66. ↩

[43]  PIAO, C., WINANDY, J. E., & SHUPE, T. F. 2010 From hydrophilicity to hydrophobicity: a critical review: part i. wettability and surface behavior. *Wood and Fiber Science* **42** (4), 490–510. ↩

[44]  PIERIS, S. 2017 *Experimental investigation of a normally impinging planar jet.* MA thesis, University of Waterloo. ↩

[45]  PIERIS, S., ZHANG, X., YARUSEVYCH, S., & PETERSON, S. D. 2019 Vortex dynamics in a normally impinging planar jet. *Experiments in Fluids* **60** (5), 1–18. ↩

[46]  PILCH, M. & ERDMAN, C. 1987 Use of breakup time data and velocity history data to predict the maximum size of stable fragments for acceleration-induced breakup of a liquid drop. *International journal of multiphase flow* **13** (6), 741–757. ↩

[47]  RAAD, M., REZAZADEH, S., JALILI, H., & ABBASINEZHAD FALLAH, D. 2021 A numerical study of droplet splitting in branched t-shaped microchannel using the two-phase level-set method. *Advances in Mechanical Engineering* **13** (11), 16878140211045487. ↩

[48] RAZZAGHI, A. & AMIRFAZLI, A. 2019 Shedding of a pair of sessile droplets. *International Journal of Multiphase Flow* **110**, 59–68. ↩

[49] RAZZAGHI, A. 2018 *Shedding of Multiple Sessile Droplets*. MA thesis, York University. ↩

[50] REINECKE, W. & MCKAY, W. 1969 EXPERIMENTS ON WATER DROP BREAKUP BEHIND MACH 3 TO 12 SHOCKS. *Tech. rep.*, Avco Corp., Wilmington, Mass. Avco Government Products Group. ↩

[51] REINECKE, W. & WALDMAN, G. 1970 A study of drop breakup behind strong shocks with applications to flight. *Avco Report AVSD-0110-70-77* ↩

[52] ROISMAN, I. V., CRISCIONE, A., TROPEA, C., MANDAL, D. K., & AMIRFAZLI, A. 2015 Dislodging a sessile drop by a high-reynolds-number shear flow at subfreezing temperatures. *Physical Review E* **92** (2), 023007. ↩

[53] SAVORY, E. & TOY, N. 1986 Hemisphere and hemisphere-cylinders in turbulent boundary layers. *Journal of Wind Engineering and Industrial Aerodynamics* **23**, 345–364. ↩

[54] SCHMUCKER, J. A. 2012 *Experimental investigation of wind-forced drop stability*. Texas A&M University. ↩

[55] SEILER, P. M., GLOERFELD, M., ROISMAN, I. V., & TROPEA, C. 2019 Aerodynamically driven motion of a wall-bounded drop on a smooth solid substrate. *Physical Review Fluids* **4** (2), 024001. ↩

[56] SHUKLA, A. K. & DEWAN, A. 2017 Flow and thermal characteristics of jet impingement: comprehensive review. *Int. J. Heat Technol* **35** (1), 153–166. ↩

[57] SILVA, F. S., MEDRONHO, R. A., & BARCA, L. F. 2019 Experimental study of water droplet break up in water in oil dispersions using an apparatus that produces localized pressure drops. *Oil & Gas Science and Technology–Revue d'IFP Energies nouvelles* **74**, 1. ↩

[58] STEFANITSIS, D., STROTOS, G., NIKOLOPOULOS, N., KAKARAS, E., & GAVAISES, M. 2019 Improved droplet breakup models for spray applications. *International Journal of Heat and Fluid Flow* **76**, 274–286. ↩

[59] SURYAPRAKASH, R. & TOMAR, G. 2019 Secondary breakup of drops. *Journal of the Indian Institute of Science* **99**, 77–91. ↩

[60] TAYLOR, T. 1992 Wind pressures on a hemispherical dome. *Journal of Wind Engineering and Industrial Aerodynamics* **40** (2), 199–213. ↩

[61] THEODORAKAKOS, A., OUS, T., GAVAISES, M., NOURI, J., NIKOLOPOULOS, N., & YANAGIHARA, H. 2006 Dynamics of water droplets detached from porous surfaces of relevance to pem fuel cells. *Journal of colloid and interface science* **300** (2), 673–687. ↩

[62] Wang, S., Chang, S., & Zheng, H. 2018 Study on dynamic characteristics of water drop on surface with different wettability under shear of airflow. In *Proceedings 18th International Symposium on Flow Visualization*. ETH Zurich. ←

[63] White, E. B. & Schmucker, J. A. 2021 Wind-and gravity-forced drop depinning. *Physical Review Fluids* **6** (2), 023601. ←

[64] Wierzba, A. 1990 Deformation and breakup of liquid drops in a gas stream at nearly critical weber numbers. *Experiments in fluids* **9** (1-2), 59–64. ←

[65] Wierzba, A. & Takayama, K. 1988 Experimental investigation of the aerodynamic breakup of liquid drops. *AIAA journal* **26** (11), 1329–1335. ←

[66] Wood, J. N., De Nayer, G., Schmidt, S., & Breuer, M. 2016 Experimental investigation and large-eddy simulation of the turbulent flow past a smooth and rigid hemisphere. *Flow, Turbulence and Combustion* **97** (1), 79–119. ←

[67] Wu, P.-K., Ruff, G., & Faeth, G. M. 1991 Primary breakup in liquid-gas mixing layers. *Atomization and sprays* **1** (4). ←

[68] Xu, Z., Wang, T., & Che, Z. 2020 Droplet deformation and breakup in shear flow of air. *Physics of Fluids* **32** (5), 052109. ←

[69] Zhang, X. & Basaran, O. A. 1995 An experimental study of dynamics of drop formation. *Physics of fluids* **7** (6), 1184–1203. ←

[70] Zhang, X. 2021 *Interaction of water droplets residing on a solid surface with wall-bounded shear flows*. PhD thesis, University of Waterloo. ←

[71] Zhang, X., Tuna, B. A., Yarusevych, S., & Peterson, S. D. 2021 Flow development over isolated droplet-inspired shapes. *International Journal of Heat and Fluid Flow* **88**, 108756. ←

# Appendices

# Appendix A

# Selection of Droplet Depinning Criteria

As mentioned in Section 4.2, the depinning of the upstream contact point was selected as the criterion for droplet depinning in the present study. Droplet depinning was identified when the upstream contact point's displacement exceeded a set pixel displacement threshold. The pixel displacement threshold was selected such that, within the ensemble of test runs, the selection limits both the bias error arising from a more conservative choice of the displacement threshold and variations across the ensemble arising from too small of a threshold value. To minimize the overall error, the pixel displacement threshold was progressively increased from 1 px to 100 px and the corresponding mean and standard deviations of depinning velocities across all tests in the configuration were calculated. The "mean differential" was also calculated as the forward difference in mean depinning velocities between consecutive displacement thresholds. This metric was used to reflect the bias in depinning velocity due to an increment of one pixel. Figure A.1 shows the typical mean differential (black markers) and standard deviation (red markers) over the tested threshold range. The optimal pixel displacement threshold is chosen where both parameters are small and relatively invariant with pixel increments. In the example shown in Figure A.1, this occurs in the range of 20 to 30 px; the threshold of 25 px (shown by the black dashed line) was chosen manually from this range. This process used in selecting the pixel displacement threshold is the same one used by Zhang [70].

The selected displacement thresholds used for each volume investigated in Section 3.2 are detailed in Table A.1. The selected displacement thresholds (23 px $\lesssim \Delta x_u \lesssim$ 25 px) in the present study are noticeably higher than in the study be Zhang [70], which were in the range 6 px $\lesssim \Delta x_u \lesssim$ 8 px. One reason for this is the higher pixel resolution of the droplet images in this study compared to Zhang. Consequently, a displacement of one
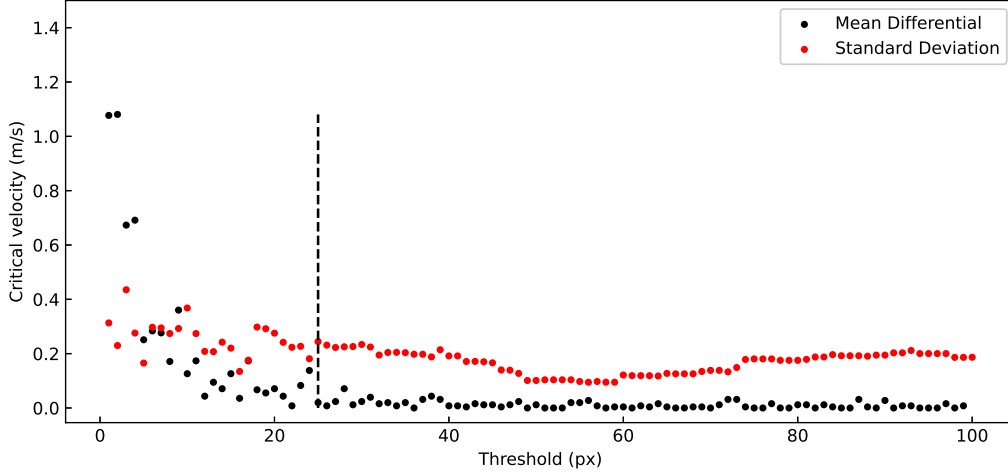
**Figure A.1:** Typical procedure of pixel threshold selection using 50 µl droplets at $\frac{dU_j}{dt} =$ 4.4 m/s. Black markers show the forward difference in mean critical depinning velocity determined by two consecutive pixel thresholds. Orange markers indicate standard deviation in critical depinning velocities identified by a given pixel threshold for a given configuration. The vertical black dashed line represents the selected pixel displacement threshold.

pixel in the present study translates to a smaller millimeter displacement than in the study by Zhang. Additionally, for the same impinging angle, the droplets in the present study were initially placed closer to the jet exit compared to the study by Zhang. The increased loading, and acceleration, would most likely cause the droplets to travel a greater distance at depinning. However, the induced error is expected to be small, as $U_{\mathrm{crit}}$ measurements in the present study showed good agreement with measurements by Zhang (see Fig. 4.4).

**Table A.1:** Selected pixel threshold for droplet depinning. Note that all pixel thresholds correspond to approximately 0.3 mm

| Volume (µl) | Depinning threshold (px) |
| --- | --- |
| 50 | 23 |
| 100 | 25 |
| 200 | 25 |
| 300 | 25 |
| 400 | 22 |
| 500 | 24 |
| 600 | 25 |

# Appendix B

# Experimental Uncertainty

The uncertainties reported throughout this thesis were calculated over a 68% confidence interval. For a specific quantity ($\beta$), the associated total uncertainty ($\epsilon_\beta$) due to n sources of error was estimated using Moffat's [38]-[36] root-square-sum method. This approach is summarized in Equation B.1. Although it is impossible to include all sources of error in this approach, great care has been taken to account for the major contributors to each uncertainty estimate.

$$\epsilon_\beta = \sqrt{\sum_{i=1}^{n} \epsilon_i^2} \tag{B.1}$$

For a derived quantity ($\beta$) related to measured quantities ($\alpha_i$) through a known relationship ($\beta = f(\alpha_1, \alpha_2, ... \alpha_n)$), its uncertainty ($\epsilon_\beta$) was estimated using a root-sum-square approach similar to Equation B.1. This approach is summarized in Equation B.2.

$$\epsilon_\beta = \sqrt{\sum_{i=1}^{n} (\frac{\delta f}{\delta \alpha_i} \epsilon_{\alpha_i})^2} \tag{B.2}$$

In scenarios where the relationship between the derived quantity ($\beta$) and the measured quantities ($\alpha_i$) are too complex, the uncertainty ($\epsilon_\beta$) was estimated using the method of sequential perturbation [37][36]. The approach is as follows:

1. Calculate the derived quantity using $\alpha_i$ without accounting for uncertainties, this is denoted as $\beta_0$.

2. For each i, calculate $\beta_{i+}$ and $\beta_{i-}$ using $\alpha_i + \epsilon_{\alpha_i}$ and $\alpha_i - \epsilon_{\alpha_i}$ respectively while other

measured quantities remain unchanged. The uncertainty contribution by $\alpha_i$ can then be estimated as the average of $|\beta_{i+} - \beta_0|$ and $|\beta_{i-} - \beta_0|$.

3. Finally, the total uncertainty ($\epsilon_\beta$) can be estimated using Equation B.1.

Uncertainty analysis for the measurements acquired in Chapter 3 and the results reported in Chapter 4 were conducted using the approaches summarised above. The resulting estimates of measurement uncertainties throughout this thesis are presented in Table B.1.

**Table B.1:** Uncertainty estimates for experiment measurements and derived quantities.

| Parameter | Uncertainty |
|:---:|:---:|
| $\theta_j$ | $\pm 0.07°$ |
| $U$ | $\pm 2.6\%$ |
| $\frac{dU_j}{dt}$ | $\pm 3.8\%$ |
| $V_0 \in [10, 100]$ µl | $\pm 0.33$ µl |
| $V_0 \in (100, 1000]$ µl | $\pm 2.1$ µl |
| $l, w, h$ | $\pm 0.01$ mm |
| $\overline{\theta}_s$ | $\pm 2.4°$ |
| $\overline{U}_{\text{crit}}$ | $\pm 5.2\ \%$ |
| $\overline{U}_{\text{neck}}$ | $\pm 7.0\ \%$ |
| $\overline{U}_{\text{br}}$ | $\pm 6.7\%$ |
| $\overline{\text{Oh}}$ | $\pm 1.3\%$ |
| $\overline{\text{We}}_{h,\text{crit}}$ | $\pm 13.9\%$ |
| $\overline{\text{We}}_{h,\text{neck}}$ | $\pm 15.4\%$ |
| $\overline{\text{We}}_{h,\text{br}}$ | $\pm 16.6\%$ |

In all the experiments conducted in Chapter 4, the impinging angle ($\theta_j$) was fixed at 30° using a digital protractor. The protractor was used to take measurements on both the nozzle exit and the impinging surface in order to set the relative angle between the two surfaces. The resulting uncertainty of the impinging angle ($\epsilon_{\theta_j}$) was calculated based on the protractor's angular resolution using Equation B.1.

As discussed in Section 3.1, the flow velocity corresponding to each droplet image was estimated using a linear least-square fit. The linear fit was applied to an ensemble average of five velocity ramp-up trials, in which the flow velocity was measured using a Dantec Streamline Pro constant-temperature anemometer. Consequently, the error of the least-square fit (RMSE) and the error of the velocity measurements were primary contributors to the total uncertainty ($\epsilon_U$). The error in a given velocity sample was due to calibration, and variations in experimental conditions such as temperature variations, ambient pressure variations, humidity, and probe positioning.

The sessile volume of the considered droplets in the present study were measured using

micropipettes. Two micropipettes of ranges [10, 100], and [100, 1000] µl were used. The uncertainty of the volume measurements ($\epsilon_{V_0}$) were estimated from the manufacturer's calibration of the corresponding micropipette. The contact angles of the droplets ($\theta_u$ and $\theta_d$) were also measured using a sub-pixel polynomial fitting (SPPF) method which has an expected error of 1° irrespective of lightening conditions [12]. The error due to the SPPF algorithm as well as random errors (STD) from droplet placement and surface heterogenity were used in estimating $\epsilon_{\theta_u}$ and $\epsilon_{\theta_d}$. Additionally, the dimensions of the droplet $(l, w, h)$ were measured using detected droplet boundaries. The uncertainty of the positions of the corresponding two boundary extents, which was estimated from image calibration, were the primary contributor to the total uncertainty ($\epsilon_l, \epsilon_w, \epsilon_h$) of each droplet dimension.

In Section 4.2, the criterion for droplet depinning was the displacement of the upstream contact point beyond a selected pixel displacement threshold. The process used in selecting the pixel displacement threshold is detailed in Appendix A. The total uncertainty in $\overline{U}_{\mathrm{crit}}$ was estimated from $\epsilon_U$, random errors, and bias. The random errors and bias where estimated from the standard deviation and the mean differential corresponding to a selection of $\pm 5$ px respectively (see Appendix A).

The total uncertainty in $\overline{U}_{\mathrm{neck}}$ was estimated from $\epsilon_U$, random errors (STD), and the error of the fit (RMSE) used in detecting the onset of necking. The total uncertainty in $\overline{U}_{\mathrm{br}}$ was estimated from $\epsilon_U$, random errors (STD), and the uncertainty in the breakup detection algorithm. The uncertainty in the breakup detection algorithm was derived from the uncertainty in the predicted time of breakup. This was estimated as the error (RMSE) in estimates from the algorithm compared to manual measurements of the droplet breakup time.

The Ohnesorge number (Oh) and the Weber number (We) are two dimensionless numbers (defined in Chapter 4) that were used in the present study. The total uncertainty of each dimensionless number was calculated using Equation B.2. Uncertainty contributions from the measured quantities were estimated based on $\epsilon_l$ or $\epsilon_h$, and variations in ambient temperature and pressure across experiments. The random error contribution (STD) was also included in the estimates of the total uncertainty. Additionally, the total uncertainty of the Weber number also included error contributions from the critical flow velocity being normalized.

In Section 4.4, the volume of the child droplet ($V_{\mathrm{child}}$) resulting from breakup was estimated using the numerical method detailed in Section 3.4. In order to evaluate the error of the volume estimation algorithm, it was tested on sessile volumes ($V_0 \in [50, 600]$ µl) which were deposited with the aforementioned micropippettes. The RMSE was used to quantify the error of the algorithm relative to the micropipette measurements. The uncertainty in the child droplet's volume was primarily due to the ineffectiveness of the ellipse fit used for the cross-sectional slices of the droplet. This error was seen to reduce for smaller droplet volumes due to the droplets approaching a more spherical shape. The uncertainty of the algorithm was estimated to be less than 10% for 2 µl $\lesssim V_0 \lesssim$ 50 µl such as the child droplets in the present study. Sub-microliter droplets below this range were too small to be reliably detected by top-view cameras due to the lower contrast of the sub-microliter droplets with the substrate. In the distributions of $V_{\mathrm{child}}$, the uncertainty

contributions due to inter-trial variations (interquartile range) were significantly greater than the uncertainty contributions from the volume estimation algorithm. Consquently, only the inter-trial variation is shown with the error bars in Figure 4.16.

# Appendix C

# Supplementary Information

## C.1  Droplet height at critical flow velocities

Figure C.1 shows the height of the investigated droplets immediately prior to their depinning (Figure C.1 (a)), necking (Figure C.1 (b)), and breakup (Figure C.1 (c)). Measurements were averaged over 40 milliseconds prior to the detection of the aforementioned critical events.
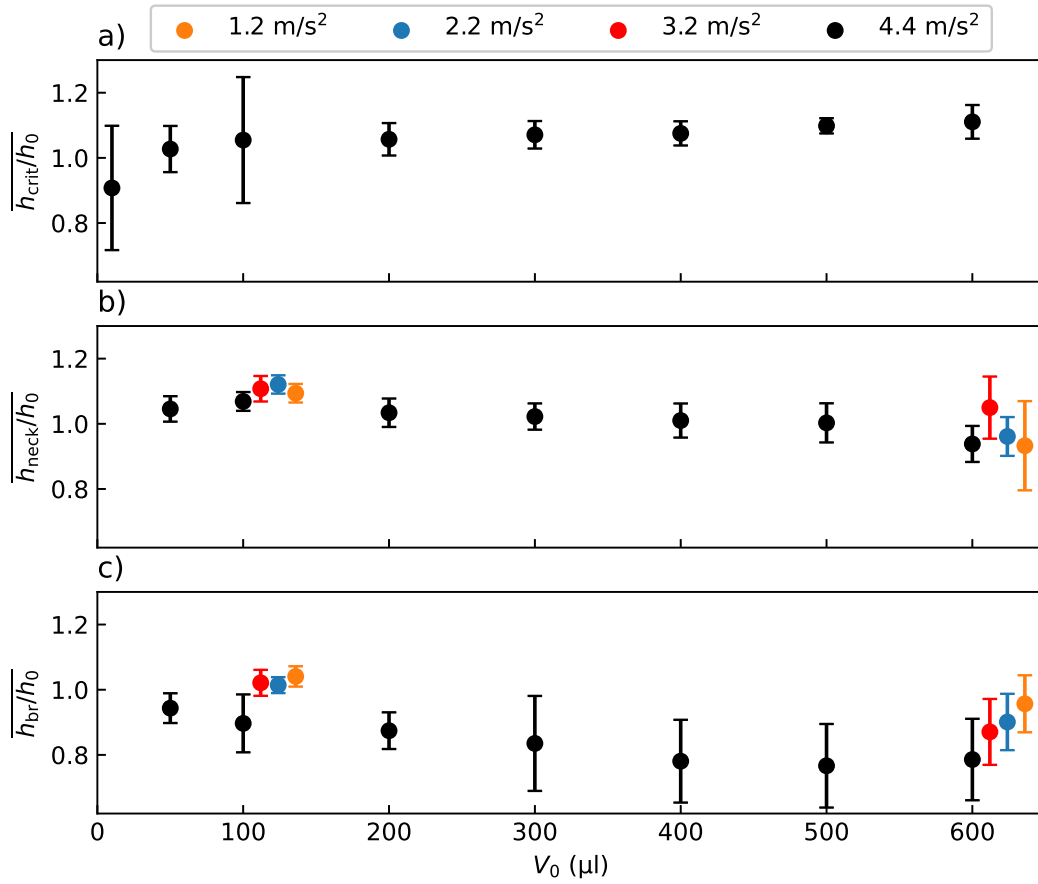
**Figure C.1:** Height of droplet at a) critical depinning velocity, b) flow velocity at the onset of necking, and c) flow velocity at which breakup occurs normalized by sessile height. Error bars represent the corresponding uncertainty bounds (68% confidence).

## C.2 Droplet length at critical flow velocities

Figure C.2 shows the length of the investigated droplets immediately prior to their depinning (Figure C.1 (a)), necking (Figure C.1 (b)), and breakup (Figure C.1 (c)). Measurements were averaged over 40 milliseconds prior to the detection of the aforementioned critical events.
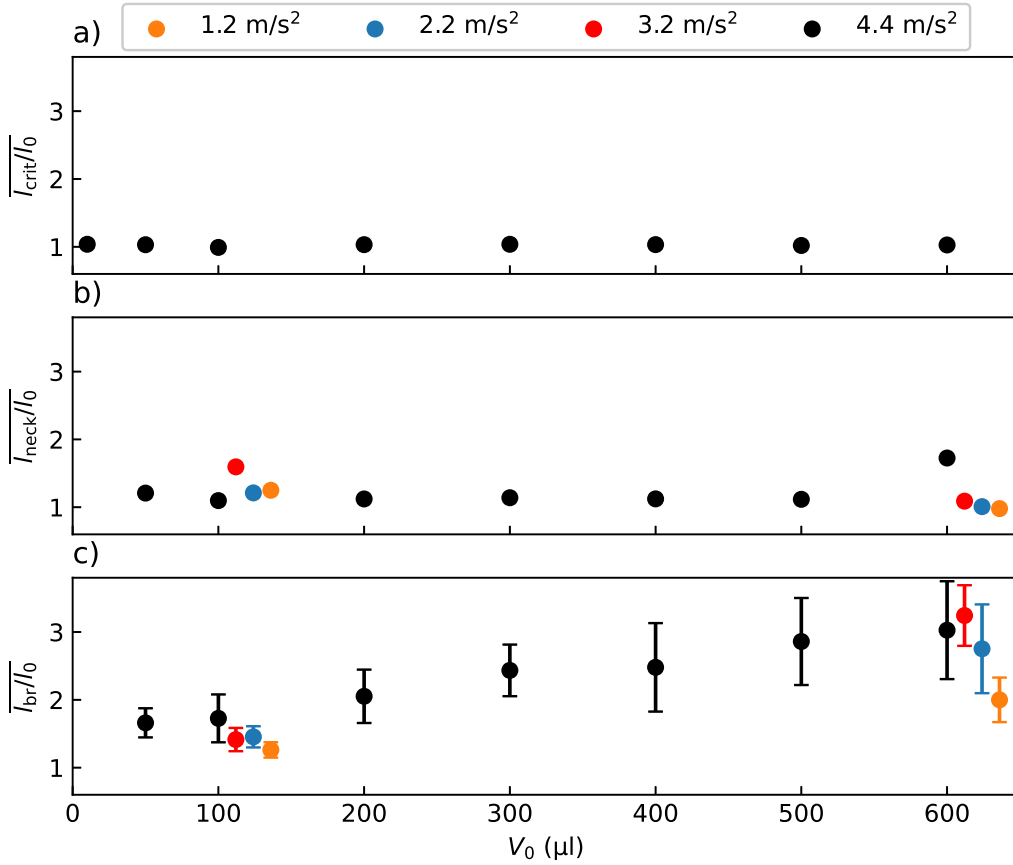
**Figure C.2:** Length of droplet at a) critical depinning velocity, b) flow velocity at the onset of necking, and c) flow velocity at which breakup occurs normalized by sessile length. Error bars represent the corresponding uncertainty bounds (68% confidence).

# C.3 Evolution of droplet minimum width during neck-ing

Figure C.3 shows the ensemble of $w_{\min}$ across all tests conducted for some of the investigated sessile volumes in Table 3.2 in response to the jet exit velocity ramp up (Figure 3.2 (d)). The displayed jet exit velocities are normalized by the estimated $\overline{U}_{j,\mathrm{crit}}$ (Figure 4.4) corresponding to the droplet's sessile volume, while the displayed minimum widths are normalized by the sessile length of the droplets. Similar figures for the 50 µl and 600 µl droplets are shown in Figure 4.7 (e) and (f). respectively.
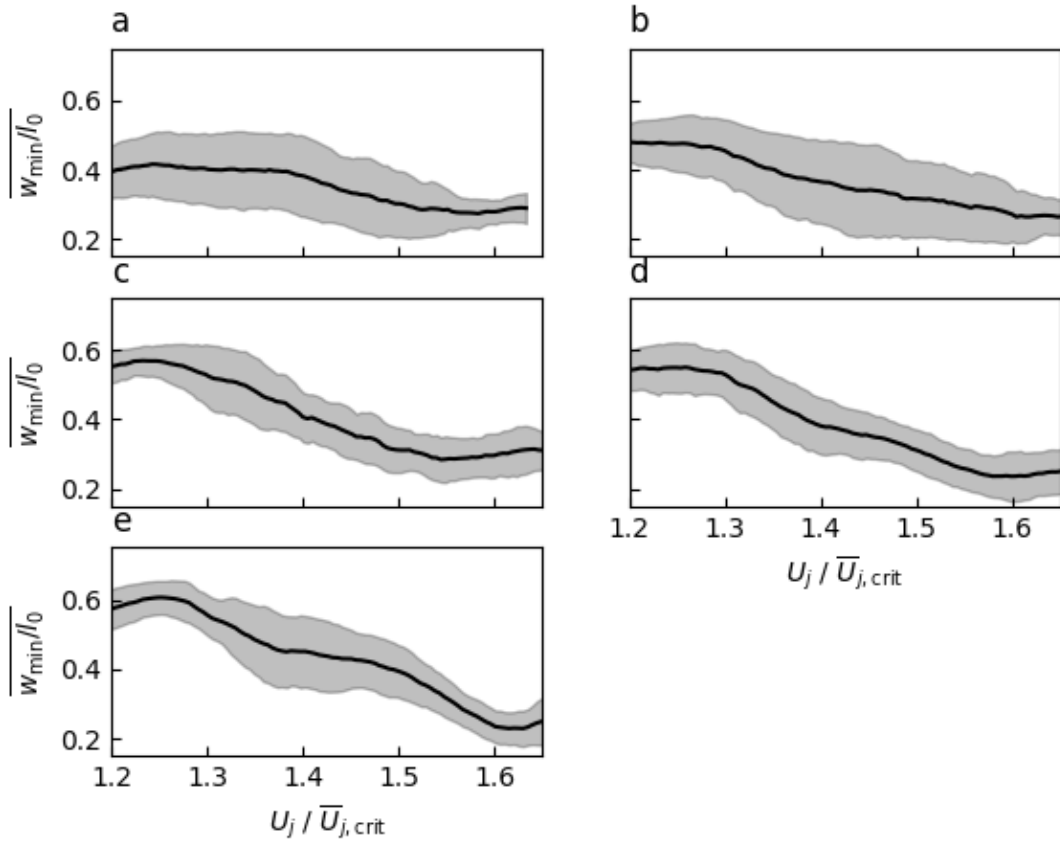


**Figure C.3:** Necking of investigated droplet volumes illustrated by ensemble averages of $w_{\min}$ vs $U_j$ ($\frac{dU_j}{dt}$ =4.4 m/s$^2$) of all tests conducted in each configuration. Each subplot corresponds to the following sessile volumes: a) 100, b) 200, c) 300, d) 400, and e) 500 µl. Note that the ensemble spreads indicate one standard deviation.

## C.4  Height of child droplet

Figure C.4 shows the height of the largest child droplet resulting from the breakup of the droplets studied in Table 3.2. Measurements were averaged over 40 milliseconds after the child droplets reached a new metastable state after breakup.
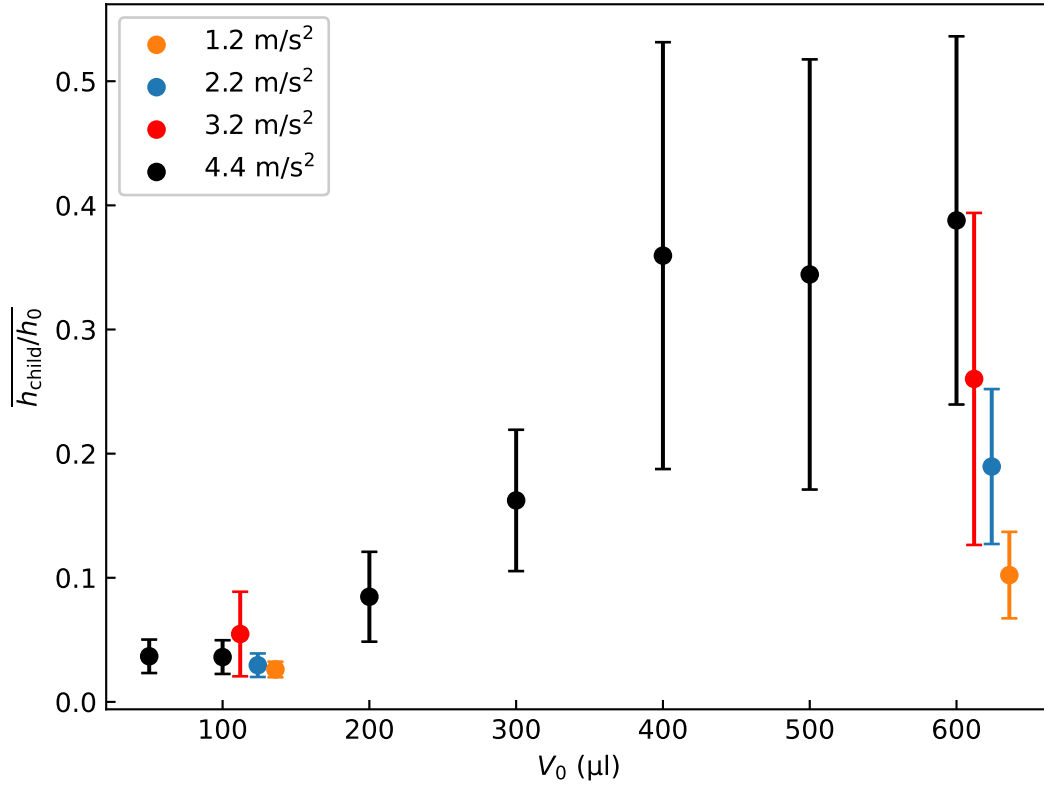


**Figure C.4:** Height of child droplet shortly after breakup for the range of droplet volumes and flow accelerations tested. Note that different flow accelerations are shown with a slight volume offset for clarity for 100 µl and 600 µl droplets. Error bars represent the corresponding uncertainty bounds (68% confidence).